Modification of Tip-Vortices using Chevron Wing Tips

Anushka Goyal

Department of Mechanical Engineering
McGill University
Montreal, Canada

August, 2019

A thesis submitted to McGill University in partial fulfillment of the requirements of the Masters in Mechanical Engineering

Abstract

This study focuses on the effect of chevrons located on the tip of a flat plate on the overall aerodynamic performance and the near field structure of the tip vortex. The aerodynamic performance of chevrons with varying depths, cut directly into the tips of a flat plate with a semi aspect ratio of 3 were investigated using a time resolved six axis force/torque sensor at a Reynolds number of 67,000. Results show that that highest lift-to-drag ratio, $\frac{L}{D}$ was obtained for an angle of attack of 5°. For shallower chevrons, this $\frac{L}{D}$ ratio was increased by up to 7.7% compared to a flat plate. It is known that the formation of a tip vortex depends on the geometry of the wing tip [1], [2]. The tip-vortex was measured using constant temperature anemometry and a four-wire hot-wire probe. The chevron plates formed tip vortices that have lower peak tangential velocities and larger core radii as compared to a flat plate. To ensure that this effect was due to the presence of chevrons and not due to wandering, which is an inherent meandering of the tip vortex, Devenport *et. al* [3]'s correction was applied to the test plates with a laminar core. The tip vortices formed on wing tips with deeper chevrons exhibited a turbulent core, as opposed to those formed on a flat plate. It was also found that deeper chevron plates had an impact on the wandering of the tip vortex- plates with deeper chevrons exhibited a narrow range of frequencies over which the cross power spectral density coefficient showed a spike, as opposed to the flat plate, which showed spikes in the cross power spectral density coefficient at a wide range of frequencies.

Résumé

Cette étude porte sur l'effet de chevrons situés sur la pointe d'une plaque plate sur les performances aérodynamiques globales et sur la structure en champ proche du tourbillon marginal. Les performances aérodynamiques de chevrons de différentes profondeurs, découpés directement dans les pointes d'une plaque plate avec un demi-allongement d'aile de 3, ont été étudiées à l'aide d'un capteur de force et de moment à six axes à résolution temporelle, à un nombre de Reynolds de 67,000. Les résultats montrent que le rapport de finesse le plus élevé a été obtenu pour un angle d'attaque de 5°. Pour les chevrons moins profonds, ce rapport $\frac{L}{D}$ a été augmenté de 7.7% au maximum par rapport à une plaque plate. Il est démontré que la formation d'un tourbillon marginal dépend de la géométrie de l'extrémité de l'aile [1], [2]. Le tourbillon marginal a été mesuré par anémométrie à température constante et par une sonde à fil chaud à quatre fils. Les plaques avec chevrons ont formé des tourbillons marginaux ayant des vitesses tangentielles maximales plus basses et des rayons de noyau plus grands par rapport à une plaque plate. Pour s'assurer que cet effet était dû à la présence de chevrons et non à un biais, ce qui est un probléme inhérent au tourbillon marginal, la correction de Devenport *et al.* [3] a été appliquée aux plaques d'essai avec noyau laminaire. Les tourbillons marginaux formés sur les extrémités des ailes avec des chevrons plus profonds présentaient un noyau turbulent, par opposition à ceux formés sur une plaque plate. Il a également été constaté que les plaques à chevrons plus profonds avaient un impact sur le biais des plaques avec des tourbillons marginaux. Les chevrons plus profonds présentaient une plage de fréquences étroite dans laquelle le coefficient de densité spectrale de puissance croisée montrait un pic, par opposition à la plaque plate qui montre des pics du coefficient de densité spectrale de puissance croisée dans une large plage de fréquences.

Acknowledgments

I'd like to express my gratitude to my thesis supervisor, Prof. Nedić, for being generous with his infinite pool of knowledge, for being patient with my endless questions and for his insight every time we hit a roadblock. I am grateful for his encouragement and support during the course of this thesis. The road to learning is slow, difficult, and at times, frustrating, and I couldn't have asked for a better supervisor to walk me through it.

I'd also like to thank the members of my research group for their valuable inputs, their willingness to lend a helping hand and their friendship. It would not have been possible to submit this thesis without them. I would especially like to thank Dylan Caverly, without whose help the test facility would not have been set up in time. The test plates would not have been ready without the help of Raphaël Limbourg, who taught us how to use the laser cutter and drilled countless holes for the setup. The experimental setup would also not have been possible without members of the Machine Shop in the Department of Mechanical Engineering- Lydia, Mathieu, Harry, Andy, Sam and Meisam as well as the chief workshop technician at the Peter Guo-hua Fu School of Architecture, David Speller, and I thank them for their time, advice and punctuality.

Finally, I'd like to thank my family and friends for their unconditional love and support, in particular, my parents, for giving me the independence to be my own person and for constantly motivating me to do better.

Contents

List of Figures

List of Tables

Chapter 1

Introduction

1.1 Background and Motivation

Fluid flow is an integral aspect of engineering problems, such as finding the forces on an aircraft, the mass flow rate through a pipe, prediction of weather patterns, *etc*. Of particular importance in this thesis is the flow of air over wings. As air flows over a body, aerodynamic forces are exerted on the body due to the pressure distribution and skin friction acting on the body. Lift is the component of the aerodynamic force that acts normal to the relative velocity whilst drag acts parallel to the relative velocity.

An aircraft wing produces lift owing to its shape, which creates a pressure difference between its upper surface, or the suction side, and lower surface, or the pressure side. As a by-product of this pressure difference, the high pressure air over the bottom surface of the wing tends to curl around its tip and leak onto the upper surface, thereby, creating a circulatory motion of air around the wing tips, commonly called the tip-vortex. Therefore, wing tip vortices are by-products of lift, and entrain the incoming flow to induce a local velocity in the downward direction called downwash. In the presence of downwash, the effective relative airflow tilts, causing the lift vector to tilt and contribute to the drag, as is shown in Fig 1.1. This component of drag, called the lift induced drag, along with the profile drag, which is the drag due to the shape of the object, makes the total drag.

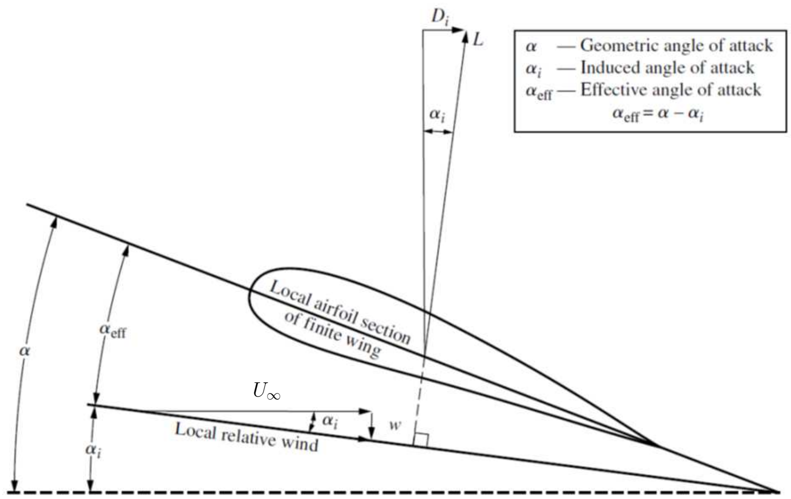

Fig. 1.1: Effect of Downwash over an Airfoil Section of a Finite Wing [4], where U_∞ is the local relative velocity, w is the downwash velocity, α is the geometric angle of attack, α_i is the induced angle of attack and α_{eff} is the effective angle of attack

During steady, level flight, the lift force balances the weight of the aircraft, while the drag is balanced by the thrust produced by the engine. Aerodynamic efficiency is defined as the ratio of lift to drag. A higher drag leads to a higher thrust required for the same amount of lift. An obvious consequence of larger drag forces is higher fuel consumption, in order to generate the required thrust for steady flight, leading to higher CO_2 emissions and noise. For instance, in 2017, the International Air Transport Association (IATA) reported an expenditure of 149 billion USD on 90 billion gallons of fuel by system-wide global commercial airlines, leading to 859 million tonnes of CO_2 emissions [5]. It is, therefore, desirable to have a lower drag for a given amount of lift *i.e.*, a high aerodynamic efficiency.

Since the total drag force is the sum of the profile drag and the induced drag, either of them could be lowered for a higher aerodynamic efficiency. Both of these components of drag are dependent on the velocity of the aircraft; when the velocity is low *i.e.*, during take-off and landing, the lift induced drag dominates over the profile drag whereas at higher velocities, the profile drag is the dominating component. This is shown schematically in Fig 1.2. At the maximum aerodynamic efficiency, *i.e*, at the point of minimum total drag in Fig 1.2, both components of drag contribute equally to the total drag. One can, therefore, see why lowering the lift induced drag becomes important. The lift induced drag is dependent on the strength of the tip vortices,

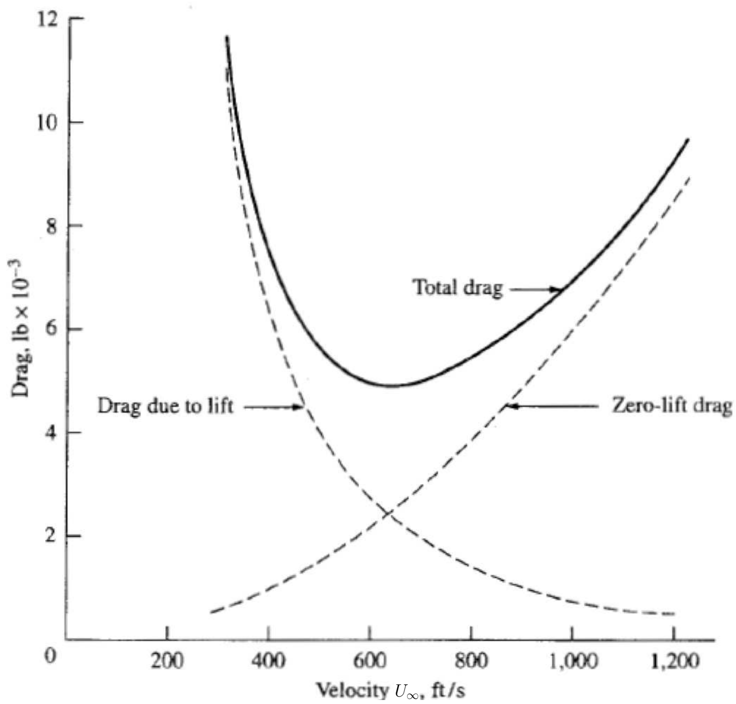

Fig. 1.2: Drag vs Velocity for the Gulfstream IV at an altitude of 30,000 ft [6]. The drag due to lift decreases with an increases in velocity, while the profile drag decreases with an increase in velocity

which will be examined in detail in Section 1.2. Another important consequence of tip vortices is that they are coherent structures and persist downstream for quite some distance while continuously growing in size. This coherence of tip-vortices determines the minimum spacing between two aircraft during take-off and landing. Faster dissipation of these vortices would reduce the minimum spacing between two aircraft and increase airport capacities.

From the above discussion, it is clear that tip vortices are a by-product of lift and modifying their structure would have a direct effect on their coherence as well as the induced drag in an aircraft. In order to understand how this can be achieved, it is necessary to first understand how tip vortices are formed and how they affect the overall aerodynamic performance.

1.2 Flow over a Finite Wing

The main function of a lifting surface is to turn the oncoming flow, so as to create a pressure gradient that can act on the solid surface and hence create a lifting force. On an aircraft, an airfoil is able to achieve this owing to its shape and the fact that the flow stays attached to the surface of the lifting body, which can be seen in Fig 1.3. This curvature in the flow field results in the velocity along a streamline to increase as we move away from the virtual center of rotation. According to Bernoulli's equation, the velocity along a streamline can be related to the pressure, where a faster flow speed results in lower pressure. Hence, on either side of the lifting body, a pressure difference is created, thereby creating the lift force, as shown in Fig 1.4. On an aircraft, the wing is the lift generating surface and is composed of many two-dimensional cross-sections of an airfoil along its span. Despite that, the aerodynamic characteristics of an airfoil are very different from that of the wing because wings are finite, three dimensional structures while airfoils are two dimensional.

As mentioned earlier, lift is generated by a pressure imbalance between the top and bottom surfaces of a wing. A consequence of this pressure imbalance is that the high pressure air over the bottom surface of the wing curls around the wing tips and tends towards the low pressure air over the top surface of the wing, as shown in Fig. 1.5. This results in a circulatory flow around the wing tips, or tip vortices, that trail downstream of the wing, as shown in Fig 1.6. The circulatory motion of air tends to push the oncoming flow downwards to create a local component of velocity in the downward direction, called the downwash (w).

Fig. 1.3: Flow visualization of the steady flow around an airfoil [7], depicting how the streamlines curve around the solid body

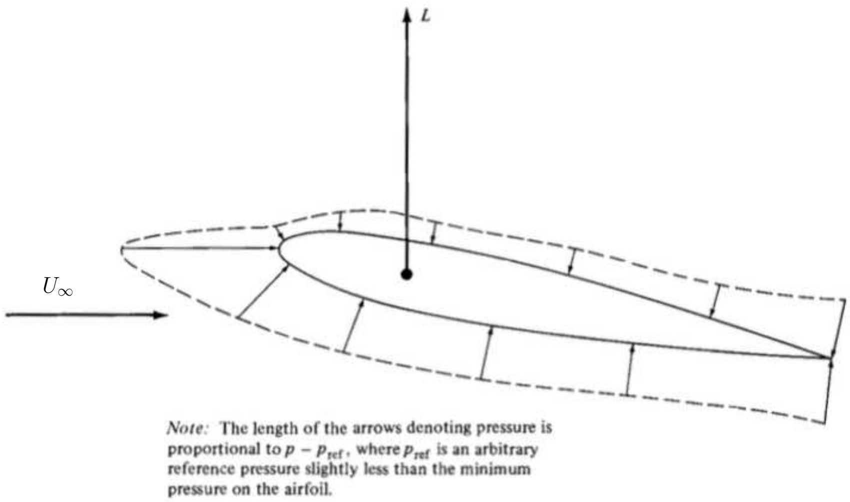

Fig. 1.4: Schematic showing the typical pressure distribution around the surface of the airfoil, as well as the resulting force vector [8]

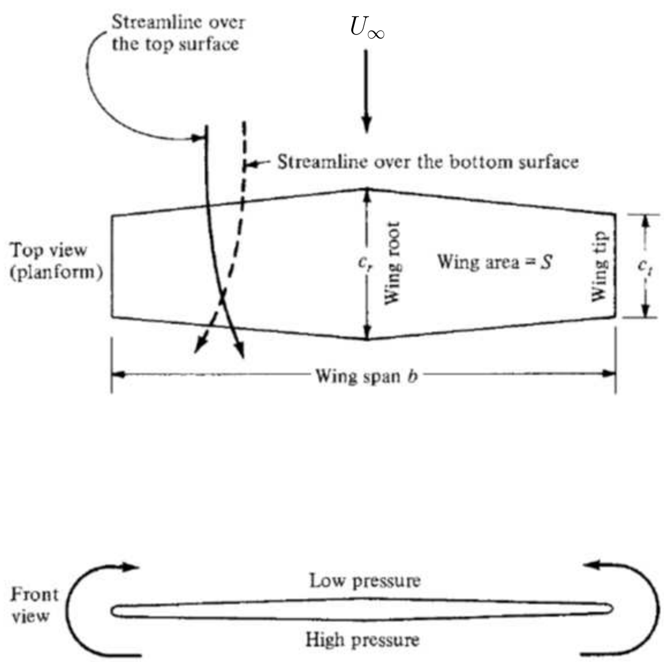

Fig. 1.5: Flow over a Finite Wing [4], where U_∞ is the incoming wind velocity, b is the wing span and S is the wing surface area; the streamlines over the suction surface curl around the root, while those on the pressure surface curl around the tip.

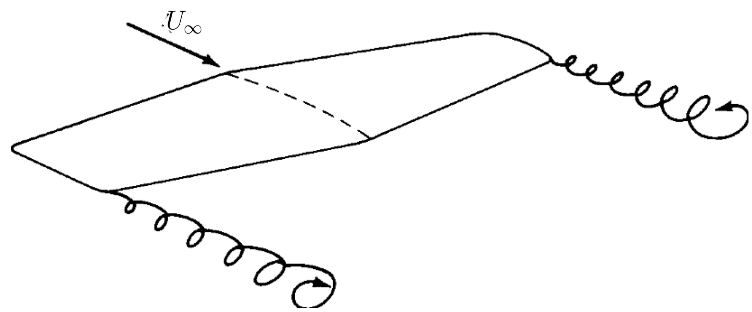

Fig. 1.6: Tip-vortices trailing downstream of a wing [4]

Downwash has two major consequences: (i) The geometric angle of attack α is the angle between the relative free stream velocity and the local airfoil section. Since the local relative velocity seen by the airfoil section would be a resultant of the free stream velocity U_∞ and downwash w, the local airfoil section sees the velocity at a smaller angle of attack- α_{eff} instead of the geometric angle of attack α (see Fig. 1.1). (ii) The lift force is a function of the angle of attack and acts perpendicular to the direction of the local velocity vector. Since the local velocity vector is titled by the induced angle α_i, the lift vector is similarly titled by the same angle which now creates a component that is acting parallel to the oncoming flow field and hence directly contributes to the drag force acting on the body. This component of drag is called the lift induced drag or D_i.

The aerodynamic forces acting on a finite wing can be quantified using Prandtl's lifting line theory, where the wing is modeled as a bound vortex filament of strength Γ. According to Helmholtz vortex theorem, a vortex filament cannot end in the fluid and we assume that the vortex filament continues as two free vortices trailing downstream, thereby forming a horseshoe vortex. The downwash due to the trailing vortices can be found using the Biot-Savart Law applied to several superimposed horseshoe vortices which model the tip vortices on a finite wing. Once the downwash (w) is computed, the induced angle (α_i) can be found. The total lift is found using the Kutta-Joukowski theorem *i.e.*, $L = \rho U_\infty \Gamma$. Once the total lift is found, the lift induced drag can be found using $D_i = L\alpha_i$. A rigorous mathematical treatment to quantify induced drag can be found in textbooks by J.D Anderson [4] and Cummings and Bertin [9]. The end result, however, gives the following expression for the coefficient of lift (C_L) and the coefficient of induced drag (C_{D_i}):

$$C_L = \frac{2}{U_\infty S} \int_{-b/2}^{b/2} \Gamma(y) dy \tag{1.1}$$

$$C_{D_i} = \frac{2}{U_\infty S} \int_{-b/2}^{b/2} \Gamma(y) \alpha_i(y) dy \tag{1.2}$$

where S is the surface area of the wing. These expressions indicate that the lift force is a function of the circulation (Γ) due to tip-vortices. Therefore, any attempt to reduce the circulation and, therefore, the strength of tip vortices would also reduce the total lift. It is also important to note that the induced drag is a function of the induced angle α_i, which directly depends on the downwash (w), which is dictated by the circulation Γ.

The lift induced drag (C_{D_i}) in addition to the profile drag (C_{D0}), which is a consequence of skin friction, gives the total drag. The drag coefficient C_D is given by:

$$C_D = C_{D_0} + k{C_L}^2 \tag{1.3}$$

where $k = \frac{1}{\pi \text{Æ} e}$ and e is the Oswald efficiency factor that tells us how close the lift distribution is to the elliptic lift distribution, which, according to Prandtl's lifting line theory, produces the lowest induced drag. Therefore, the maximum value that e can take is 1 (elliptical lift distribution), with the induced drag increasing as e tends to 0 [4]. Æ is the aspect ratio, defined as the ratio between the square of the distance between the tips of the wings or the span, b and the surface area of the wing, S.

1.2.1 Effects of Tip-Vortices

One can summarize the main consequences of tip-vortices as follows:

1. High thrust requirement- In order to overcome the drag force created by the aircraft as it flies, a thrust force needs to be generated by the engines; the larger the drag the more thrust force is required, leading to a higher fuel expenditure, CO_2 emissions and noise. According to Eq 1.2, the induced drag is dictated by the strength of the tip vortices and the downwash speed and Eq 1.3 shows that it contributes to the total drag.

2. Coherence of tip vortices- Tip vortices are coherent i.e., once they develop, they are stable and persist thousands of chords downstream of the wing [10]. This leads to the “following plane” problem: a following plane could get caught in the wake of a plane flying in front of it. As a result, the following plane would encounter a sudden change in the angle of attack and stall, or it would experience a large rolling moment that would not be controlled by the ailerons. As a result, there are regulations for a minimum spacing between aircrafts during take-off and landing, which limit airport capacity.

3. In an aircraft, the tail generates a pitching moment that maintains longitudinal static stability. The downwash angle due to tip vortices affects the flow field incident on the tail of the aircraft, as shown in Fig 1.7. An important criterion for longitudinal static stability is that the change in coefficient of pitching moment with respect to the angle of attack must be negative. This change in coefficient of pitching moment with respect to the angle of attack depends on the downwash angle α_i.

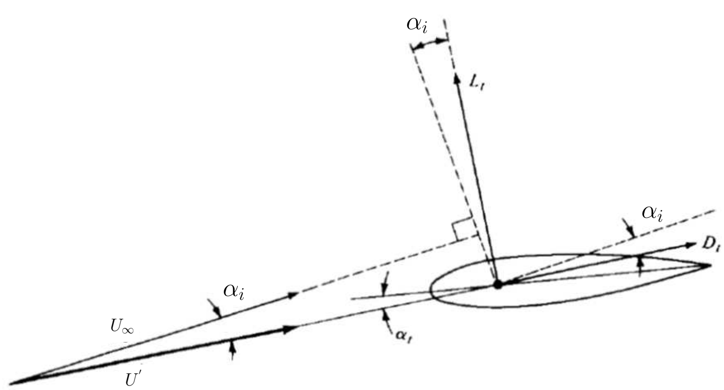

Fig. 1.7: Flow and forces in the vicinity of the tail. Here U_∞ is the free stream velocity and $U^{'}$ is the relative velocity seen by the tail after deflection due to downwash, α_t is the angle of attack at the tail [8]

To counter the adverse effects of tip vortices, most conventional aircraft use wing-tip devices.

1.2.2 Conventional Wing-Tip Devices

In commercial aircrafts, wing-tip devices are used to alter the formation of tip-vortices to reduce the induced drag and enhance lift. The earliest development of a wing-tip device was by

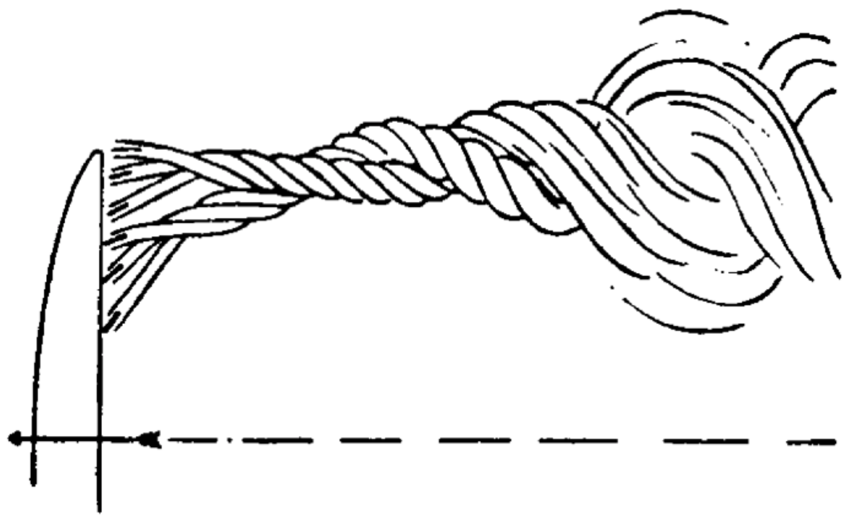

Fig. 1.8: Lanchester's drawing of a tip-vortex [11]

Lachester. Figure 1.8 shows Lanchester's sketch of a tip-vortex [11], who further proposed the use of end-plates to reduce the drag force at high lift conditions which would break the span-wise velocity component and reduce the three-dimensional effects. However, the endplates lead to a higher profile drag during cruise due to local flow separation and negated the reduction in induced drag. [12]

In the late 1970s, R.T. Whitcomb drew inspiration from bird wings and designed winglets that reduce the induced drag. He observed that the flow over the pressure surface of the wing is directed outward, towards the tip of the wing whilst the flow over the suction surface is directed inwards, towards the root of the wing. It was demonstrated that a cambered, angled, nearly vertical surface above or below the wing-tip can utilize this cross-flow tendency over the wing and thereby, reduce the strength of the tip vortex. These winglets, therefore, utilized a part of the energy of the tip vortices that would have otherwise been wasted [13]. The first winglet consequently came to be known as the Whitcomb winglet.

Several wing-tip devices have since been developed in an attempt to increase the efficiency of aircrafts, some of which are shown in Fig 1.9. These wing-tip devices work in different ways but their intended effect is to reduce the induced drag of the aircraft. For instance, tip fences extend both above and below the wing tip and utilize the span-wise component of velocity to reduce the strength of tip vortices [15]. Canted winglets are angled upwards which utilizes

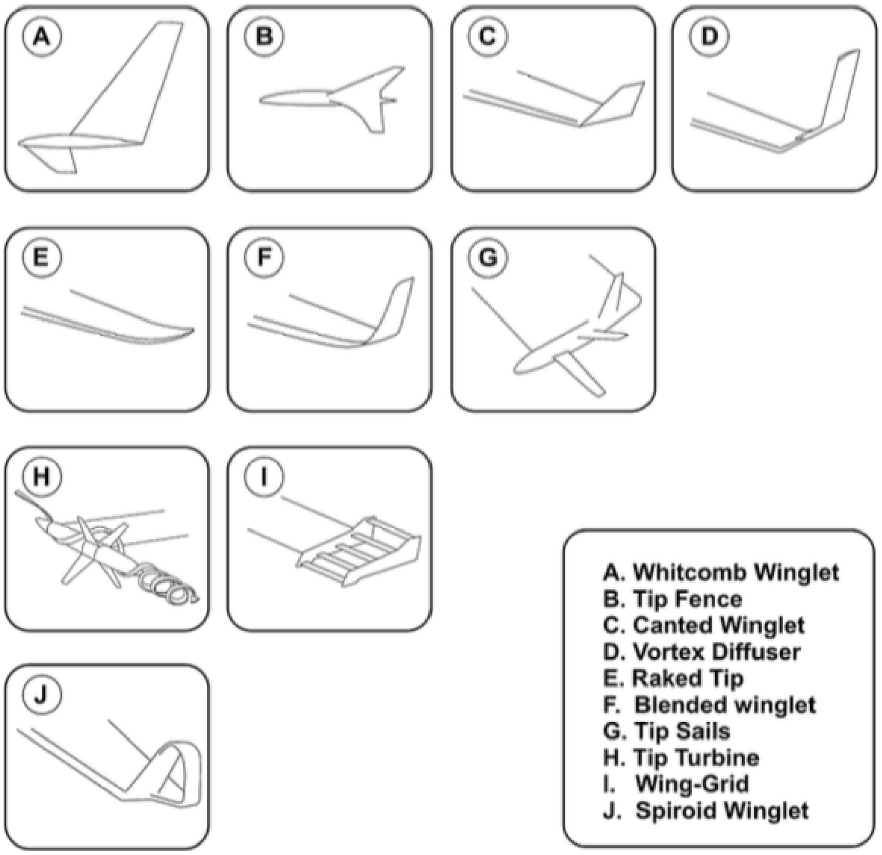

Fig. 1.9: Wing-tip devices currently in use or testing stage [14]

the span-wise component of velocity to generate an apparent thrust. Blended winglets act like canted winglets, except that they are attached to the wing with a smooth curve instead of a sharp angle to reduce interference drag at the junction of the wingtip and winglet [15]. Horizontal tip extensions have been shown to double the induced drag as compared to vertical tip extensions of the same size, but they also add twice as much weight to the wing structure [16]. Van Damn [17] showed that the induced drag for a planar wing with elliptical lift distribution can be reduced by sweeping the wing aft. A raked wing-tip (which is also bio-inspired) combines this effect with an increase in the aspect ratio, thereby reducing the induced drag. Lazos and Visser [18] studied the aerodynamic performance of a hyper-elliptic cambered span wing (shown in Fig 1.10), which was inspired from a seagull wing in gliding flight. It was found that these wings have an enhanced aerodynamic performance as compared to a conventional elliptic wing and the position of the tip-vortex had been shifted outboard.

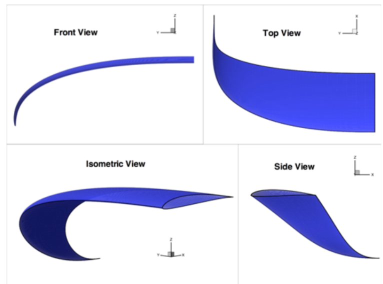

Fig. 1.10: Views of the Hyper Elliptic Cambered Span designed by [18]

While most wing-tip devices are bio-inspired, the final design consists of simple geometries. On the other hand, bird wings are more complex in nature, having slotted feathers at the wing-tips. Sheppard and Rival [19] investigated slotted delta wings and showed that they produced a higher lift due to an increase in circulation due to the presence of secondary and tertiary vortices, as compared to a conventional delta wing, as shown in Fig 1.11. It is, therefore, of interest to investigate how other complex geometries would affect the structure of the tip vortex and its development downstream of a wing. The latter becomes important as tip vortices persist several chord-lengths downstream of a wing and determine the minimum spacing between aircraft at airports during take-off and landing.

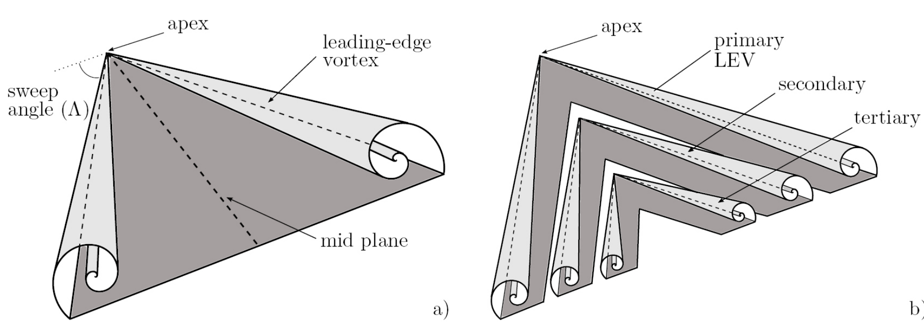

Fig. 1.11: Comparison of a delta wing in (a) to a slotted delta wing in (b) [19], showing the formation of a primary, secondary and tertiary leading edge vortex around the tips of a slotted delta wing, in contrast to the single leading edge vortex on a delta wing.

1.3 Working Hypothesis

The impact of complex geometries on wake characteristics, noise and aerodynamic performance have steadily increased over recent years. In 1997, Tombaziz and Bearman [20] found that the addition of sinusoidal trailing edges to a half-ellipse bluff body reduces the strength of the vortex street as well as the base drag, which would imply a lower profile drag. Similarly, multi scale (fractal-like) geometries, such as those shown in Fig 1.12 were found to reduce the energy of vortex shedding as compared to their non-fractal counterparts in three-dimensional bluff bodies [21]. This study also showed that even though the geometry of these bluff bodies is significantly altered, the wake arranges itself in such a way that it is similar to that of a disk.

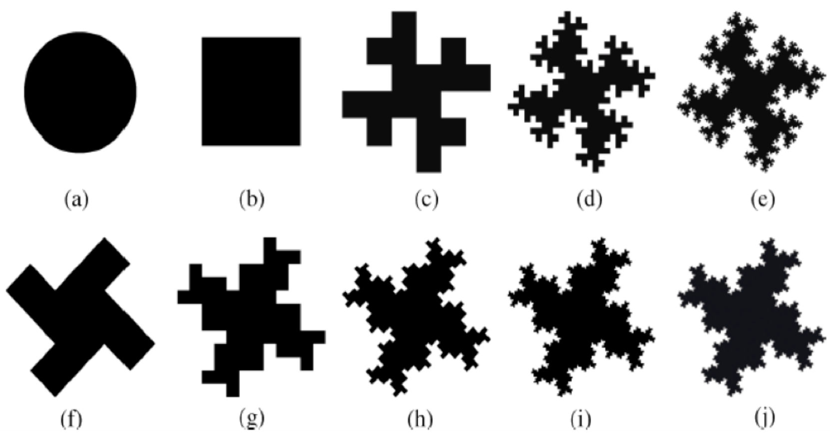

Fig. 1.12: Complex geometries for flat plates used in [21]

So far, it has been established that tip vortices have a significant impact on the performance of an aircraft *i.e.*, they lead to induced drag and they persist downstream of an aircraft for several chord lengths which leads to greater separation between aircraft during take-off and landing. To counteract these effects, commercial aircraft use wing-tip devices that help reduce the induced drag by hindering the span-wise component of velocity. Wing-tip devices used thus far, despite being bio-inspired, have simple geometries that are limited by manufacturing capabilities. However, bird wings-such as those shown in Fig 1.13- have slots cut into the wing-tips, which are noticeably different from the majority of designs seen on current aircraft. Several studies have been conducted by biologists to investigate the advantages offered by bird wings. Withers [22] extensively studied the aerodynamic properties of different bird wings at low Reynolds number

Fig. 1.13: Birds with slotted feathers [14] or 'primaries'

(1-5 x 10^4) and found that the aerodynamic properties of bird wings are different from that of an airfoil: bird wings- which operate at lower Reynolds numbers than airfoils in commercial aircraft wings- had a lower maximum lift to drag ratios (3-17) as compared to airfoils (27-60). Tucker showed that the presence of slots on the wings of a Hariss' Hawk causes the vertical diffusion of vortices, whilst the curling of its feathers during gliding made its wing non-planar and reduced the overall drag [23]. These studies have helped to establish that the aerodynamic performance of bird wings is significantly different from that of conventional aircraft wings and that the complex structures on bird wings lend them enhanced aerodynamic characteristics, such as a higher lift, better control of flow separation and better lateral stability, at low Reynolds numbers. Based on these studies, research has been conducted on engineering designs inspired from nature. The previous section shed light on how complex geometries have been shown to give better wake characteristics *i.e.*, wakes that have reduced strength. In a previous study, chevrons were cut into the trailing edge of a NACA 0012 wing to study the impact of chevrons on the self noise of a wing by Chong and Vathylakis [24]. It was found that non flat plate type serrations were effective in reducing the self noise of the wing. This study was complimented by Nedić *et al.*, [25] who used multi-scale geometries on the trailing edge of a NACA 0012, as shown in Fig 1.14 and showed that chevrons on the trailing edge of a NACA 0012 improve its lift to drag ratio. This study also

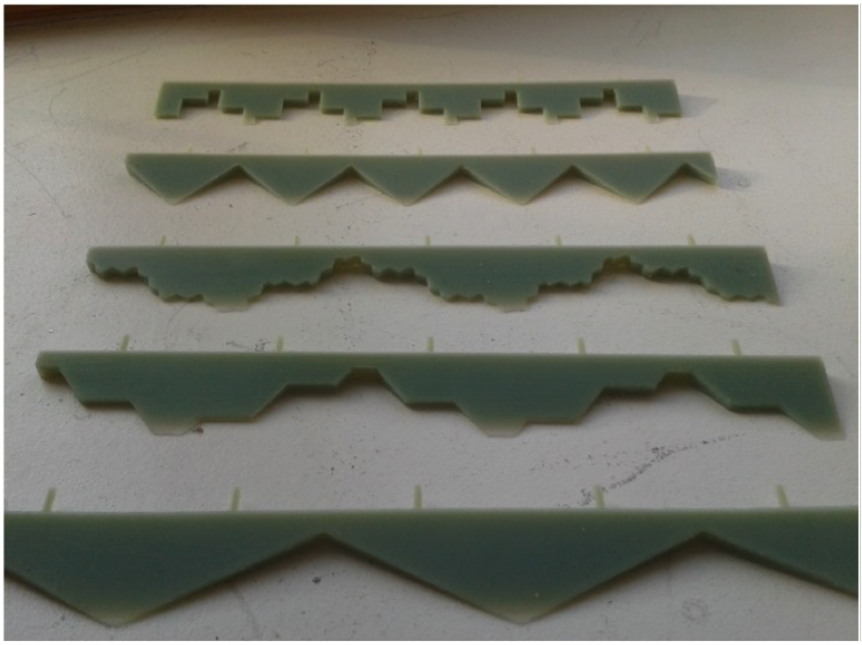

Fig. 1.14: Fractal trailing edges used in [25]

showed that the use of fractal trailing edges decreased the vortex shedding energy for chevron angles smaller than 45°. Furthermore, Prigent *et al.* [26] studied the effect of multi-scale serrations cut into the trailing edge of a NACA 0012 wing and found a lower energy associated with vortex shedding as well as lower coherence in the spanwise direction. The effect of straight, blunt and serrated trailing edge shapes on a wing were studied through Direct Numerical Simulation (DNS) and it was found that blunt trailing edges lead to periodic vortex shedding, while serrated trailing edges created a span-wise pressure gradient, leading to a smaller velocity deficit downstream of a trough, as compared to the velocity deficit downstream of a protrusion [27]. Ito [28] imitated the serrations on the leading edge of an owl wing by using jigsaw blades attached to an airfoil and found that the serrations produce higher lift and control the separation of flow over the wing only at low Reynolds numbers. These shapes are similar to the triangular teeth or chevrons that can be seen in bird wing-tips (called 'primaries').

Based on the results from Tucker's study [23], it is believed that the primary feathers located at the tip of a bird's wing can influence the structure and behaviour of the tip vortex. Our working hypothesis is that these feathers act as individual tip vortex generators, where each tip vortex is considerably smaller than the size of the tip vortex that would be created were the feathers not present. Fig 1.15 shows a schematic of how these tip vortices would be created on a simplified chevron pattern directly cut into the tip of the flat plate. Given that the pressure difference between the upper and lower surface changes along the chord (see Fig 1.4), one would expect the strength of each individual tip vortex to be lower; indeed the total combined strength of all the tip vortices could also potentially be lower compared to a tip vortex generated across the entire chord of the wing. It is, however, reasonable to assume that at some downstream distance they would merge into a single tip vortex structure. Furthermore, by generating several smaller tip vortices, one can expect a degree of mutual interaction between each vortex, which could alter the dynamics of the tip vortex and potentially reduce its coherence, resulting in faster decay rates. This is similar to the onset of the sinusoidal Crow instabilities in the trailing wake which lead to their eventual breakdown [10].

To test this hypothesis, we will investigate the aerodynamic performance and decay of tip-vortices generated by a flat plate with various chevron designs cut into the tip of the wing. The chevrons are a simplistic geometry that can be easily characterized, thus allowing us to test how various parameters of the chevron influence the overall performance. The use of a flat plate instead of an airfoil allows us to eliminate the added complexity of variable chevron thickness on an airfoil.

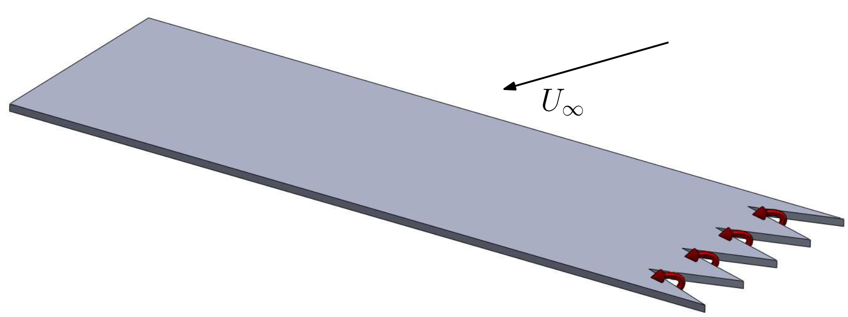

Fig. 1.15: The hypothesized development of tip vortices around chevron plates: the pressure difference between the suction and pressure surface of the plate would form smaller vortices that curl around the chevrons, as compared to a vortex generated across the entire chord of the wing.

1.4 Design of the Chevron Geometry

A chevron can be characterized by its wavelength (λ), depth ($2h$) and chevron angle (ϕ), as shown in Fig 1.16. The following expression gives the relation between these three parameters:

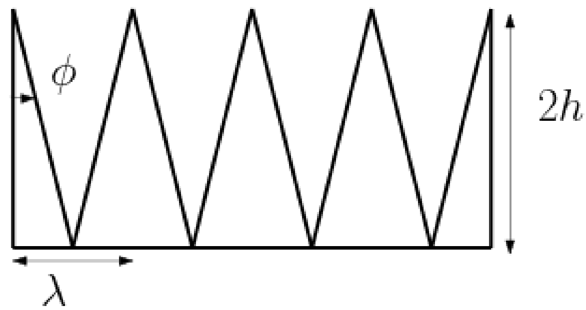

Fig. 1.16: Chevron Geometry characterized by the chevron angle (ϕ), chevron depth ($2h$) and wavelength (λ)

$$\lambda tan\phi = 4h \tag{1.4}$$

A key design requirement was that the planform area, S, remain constant in order to facilitate a meaningful comparison between the coefficients of lift, drag and moments. The coefficient of moment is defined as $C_m = \frac{M}{\frac{1}{2}\rho V_\infty Sc}$, where M is the moment about a given axis, ρ is the density of air, U_∞ is the free stream velocity, S is the planform area and c is the chord.

For this study, it was decided that the span of the flat plate would be 300 mm, whilst the chord length would be 100 mm. This gives a semi aspect ratio of 3, which is similar to the semi aspect ratio observed on birds wings, such as those shown in Fig 1.13. The schematic of the flat plate can be seen in Fig 1.17. In order to maintain the same planform area, the chevrons are applied in such a way that the area shaded in green is added while the area shaded in red is removed. If the number of chevrons is a whole number, the area added would be equal to the area removed and the total planform area would remain constant. Although this method does increase the effective span of the wing by h, the span of the planform, which we define as $b = \frac{S}{c}$, would remain as 300 mm since the planform area S and the chord length c are unchanged. Given that S represents the solid area over which the pressure difference is acting upon and hence contributing to the aerodynamic forces, we believe that it is more fruitful to use this parameter to normalize the aerodynamic forces and moments as opposed to the product of the effective span and chord.

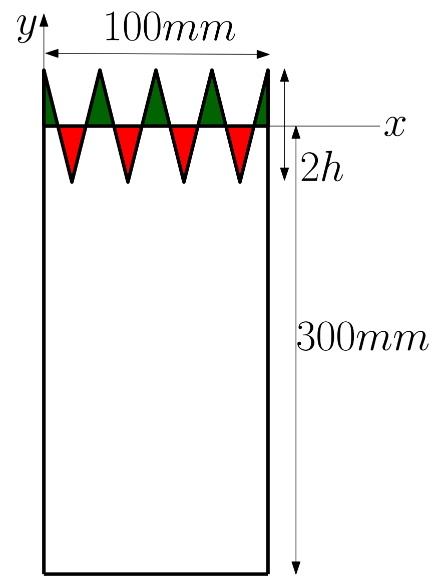

Fig. 1.17: The area added (green) and the area removed (red) from a flat plate of span 300mm and chord 100mm

In order to keep the planform area constant, the number of chevrons could only be a whole number. In this study, the number of chevrons was chosen to be four, which is comparable to the number of primaries found at the tips of bird wings, and the depth ($2h$) was varied and the wavelength was kept constant. Table 1.1 describes the five different chevron geometries that were used for this study.

Table 1.1: Table describing the chevron geometry for each plate

Plate Number	Wavelength (mm)	2h (mm)	Number of Chevrons	Chevron Angle
1	25	10	4	32.00°
2	25	20	4	22.60°
3	25	30	4	17.30°
4	25	40	4	14.08°
5	25	50	4	11.76 °

1.5 Thesis Objectives

The aim of this thesis is to answer the following questions: (i) What impact do chevrons located at the tip have on the aerodynamic performance of a flat plate? (ii) What happens to the structure of the tip vortex due to the addition of chevrons? (iii) How do chevrons affect the development of the tip vortex downstream of the flat plate?

Chapter 2

Forces and Moments on Chevron Plates

2.1 Introduction

In this section, the impact of chevrons on the aerodynamic performance is evaluated and compared to a flat plate. Time resolved forces and moments acting on the test plates were measured using a six axis force and torque sensor at a Reynolds number of 67,000.

2.2 Experimental Setup

2.2.1 Newman Wind Tunnel

All of the measurements were taken in the Newman Wind Tunnel in the Aerodynamics Lab of the Department of Mechanical Engineering, McGill University. The Newman Wind Tunnel is an open circuit tunnel with a rectangular, closed test section of cross section 2ft x 3ft and length of 9ft. Most of its structure is made of $1\frac{1}{8}$ inch plywood and the overall dimensions of the wind tunnel are 36 ft x $3\frac{1}{2}$ ft x 10ft. A schematic of the wind tunnel is shown in Fig 2.1. A bell mouth is installed at the intake, which is fitted with a curved gauze (14 x 15 mesh, 0.020x0.022 inches) and a curved honeycomb (1 inch deep). The honeycomb acts as a flow straightener before the flow is accelerated through the contraction cone (with a 6:1 contraction ratio) into the test section.

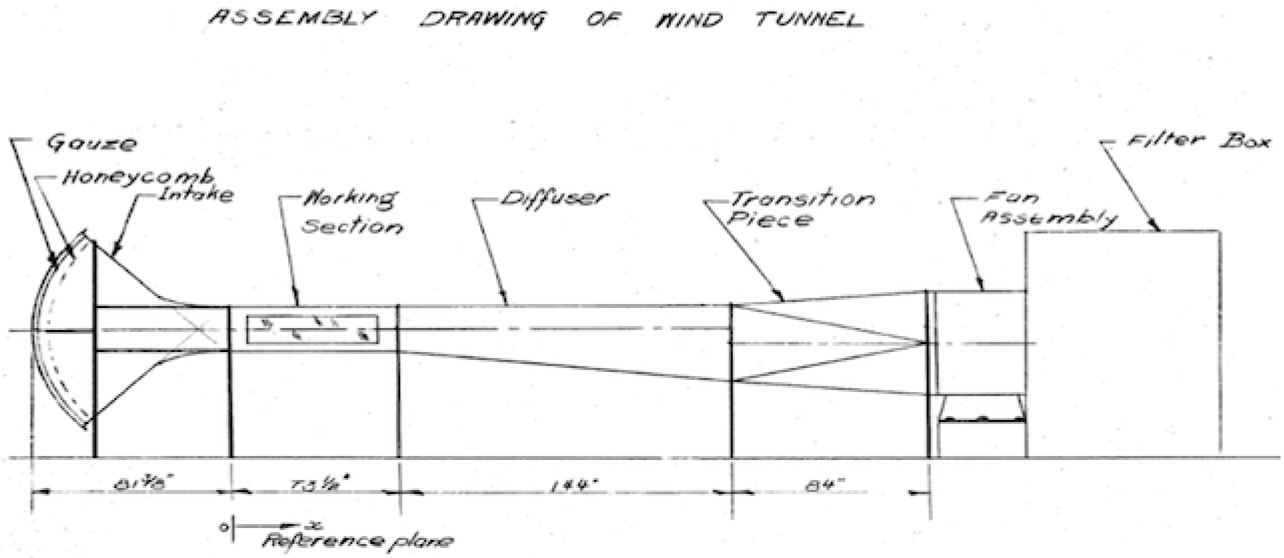

Fig. 2.1: Schematic of the Newman Wind Tunnel [29]

The test section has a background turbulence of 1.1% at a speed of 10m/s, which was also the working speed for the aerodynamic and hot-wire measurements. Details on the measurement of the background turbulence can be found in Section 3.3.2.

The test section is followed by the diffuser to decelerate the flow and a coarse steel mesh is mounted at the end of the diffuser to protect the fan. The fan unit consists of a 5 bladed axial fan that is powered by the WEG CFW 09 inverter.

The wind tunnel fan was calibrated for axial velocities between 5 m/s to 15 m/s at RPMs between 138 and 380. Equation 2.1 describes linear fit of the RPM to the axial velocity.

$$RPM = 24U_\infty + 18 \tag{2.1}$$

The calibration of the axial velocity in the test section can be seen in Fig 2.2. The temperature in the test section was measured using a 100 Ω, 3 wire National Instruments Resistance Thermometer Detector (RTD), which was connected to a National Instruments cDAQ 9174. The differential pressure was measured using a Pitot-static probe connected to a Furness Controls FCO-332 pressure transmitter with a measurement uncertainty of 0.25% of readings. The distance of the Pitot-static probe from the floor of the wind tunnel was 180 mm, which is sufficiently far from the influence of the boundary layer at the inlet of the test section, which was calculated

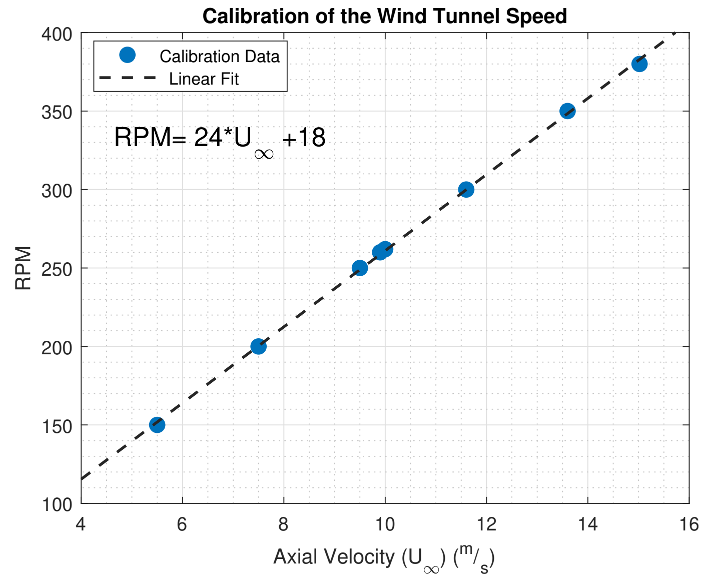

Fig. 2.2: RPM of the wind tunnel fan vs Axial velocity measured in the test section of the Newman Wind Tunnel, plot shows a linear fit to the calibration data, giving an equation RPM= $24U_\infty$ + 18

to be 5 cm, under the assumption that the boundary layer is turbulent, which is very likely an overestimation. The FCO pressure transducer was connected to a NI-USB 6363 Data Acquisition Unit (DAQ). The voltages measured by the transducer were converted to pressure using the relation 1V=100 Pa, which was provided by the manufacturer. The absolute pressure was meant to be measured using the Honeywell Model TJE Precision Gage/Absolute Pressure Transducer (rated for 100 psig), however, the pressure transducer could not receive the required excitation voltage from the National Instruments compact Data Acquisition Unit- cDAQ 9174. As a result, the absolute pressure was assumed to be 1 atm for the measurements.

2.2.2 Test Plates

Five chevron plates, with chevron geometries shown in Table 1.1, were compared to a flat plate. They were made out of 6mm thick acrylic and were cut using the Universal Laser System's VLS 6.60 in the Peter Guo-hua Fu School of Architecture. The chord length (100mm) and the average span (300mm) was kept constant, giving a semi aspect ratio ($\frac{b^2}{S}$) of 3. This aspect ratio was deemed as a good starting point for the following reasons:

1. Our hypothesis draws inspiration from birds with slotted wings (or 'primaries') such as the Steppe Eagle (*Aquila nipalensis*), Griffon Vulture (*Gyps fulvus*), Brown Eagle (*Haliaeetus leucocephalus*), etc. These bird typically have low aspect ratios ranging between 3-4 [30].

2. Blockage ratio is defined as the ratio of the frontal area of the model to the cross sectional area of the test section. A semi aspect ratio of 3 gives a blockage ratio of 5.3% at an angle of attack of 90°. While this blockage ratio is slightly over the recommended limit of 5% [31], the majority of the data presented in this thesis is at lower angles of attack, therefore, giving a lower blockage ratio.

3. The experiments were performed at a wind speed of 10m/s, giving a Reynolds number ($\frac{Uc}{\nu}$) of 67,000, which lies within the range of Reynolds' numbers that birds like the Steppe Eagle (with low aspect ratio and slotted wings) fly at (<100,000) [32].

2.2.3 Wind-Tunnel Setup

The plates were mounted on a 100 mm diameter disc with a 6 mm slot milled at its center, as shown in Fig 2.3. The disc sat flush with the floor of the wind tunnel with a gap of 0.5 mm maintained around the circumference of the disk; this is within the recommended limits of 0.005*span (=1.5 mm for the flat plate) [31]. Figure 2.4 shows how three flat head, hex drive M6 screws, 6 cm long, were used to keep the plates in place on the disc. The disc was mounted on an ATI Gamma IP68 six axis Force/Torque sensor using four flat head, hex drive, 4.5 cm long M6 screws. The range and uncertainty of the sensor is provided in Table 2.1 and Table 2.2, respectively. The disk was attached to a Newmark RM-3D-411-NC Rotary Stage, which has a resolution of ±0.002°, using a 6 mm thick aluminium plate with four 8-32 counter-bore taps for the rotary stage and four M6 counter sunk taps at the load cell end. The rotary stage was further mounted on a MiniTec frame using four M4 screws.

Table 2.1: ATI Gamma IP68 Calibrated Range (±)

F_x	F_y	F_z	T_x	T_y	T_z
32N	32N	100 N	2.5 N-m	2.5 N-m	2.5 N-m

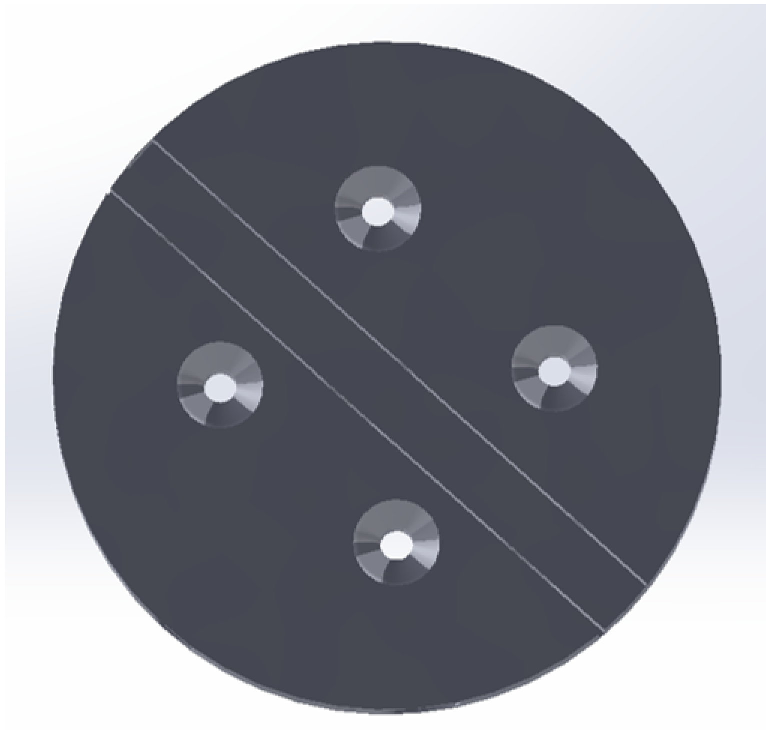

Fig. 2.3: Top View of the Disc Used for Mounting the Test Plates

The rotary stage and load cell were connected to the National Instruments USB 6363 Data Acquisition Unit (DAQ). The specifications of the DAQ are provided in Table 2.3.

2.2.4 Methodology

Normal and tangential forces, as well as moments about all three axes (pitch, roll and yaw) were measured on the test plates over angles of attack ranging from 0° to 60° in increments of 1° at a speed of 10m/s. At every angle of attack, the raw voltages from the load cell were recorded at a sample rate of 1000 Hz for 40 seconds. Once the angle of attack was changed, a pause of 10 seconds was observed before recording the load cell voltages to allow the effect of any transient forces to settle down. The bias was corrected for by measuring the raw voltages from the load cell at every angle of attack with the wind tunnel fan turned off and then subtracting these voltages from the voltages recorded with the tunnel turned on at the test speed. The raw voltages were converted into forces and moments by using the calibration file provided by the manufacturer.

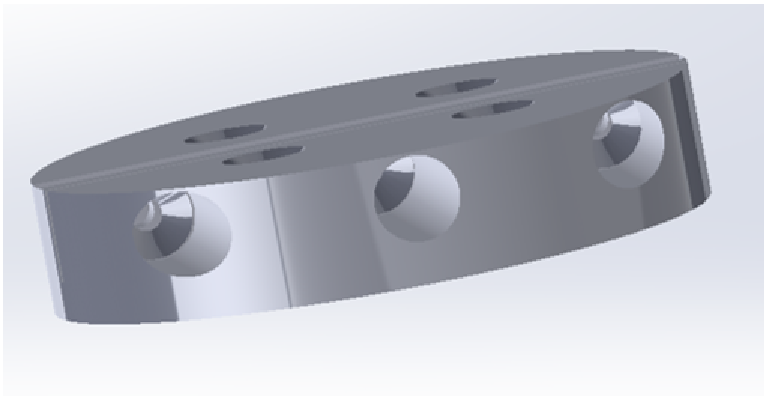

Fig. 2.4: Side View of the Disc Used for Mounting the Test Plates

Table 2.2: ATI Gamma IP68 Measurement Uncertainty (95% confidence level, percent of full scale load)

F_x	F_y	F_z	T_x	T_y	T_z
0.75%	1.00%	0.75%	1.00%	1.00%	1.50%

The entire process was automated using a LabVIEW 2017 code.

To ensure that the 0° angle of attack was captured, the rotary stage was first moved to the -5° of the “assumed” 0° and forces and moments were recorded over 65 degrees i.e., until an “assumed” +65° angle of attack. During post-processing, the data was corrected for the actual angles of attack by assuming that the 0° angle of attack is one where the the C_L was 0 and C_D was a minima. This is because, at a 0° angle of attack, a flat plate would produce no lift and have a C_L value of 0. Similarly, the total C_D on the plate would be C_{D_0}, which is the lowest value of drag that could act on the plate, based on Eq 1.3.

The chord of the test plates were aligned with the positive X axis of the load cell. Normal (X) and Tangential (Y) forces (Fig 2.5) acting on the plates were converted to the Lift and Drag forces using Equations 2.2 and 2.3.

$$L = (X sin\alpha) + (-Y cos\alpha) \tag{2.2}$$

$$D = (-X cos\alpha) + (-Y sin\alpha) \tag{2.3}$$

Table 2.3: NI USB 6363 DAQ Specifications

ADC resolution	Max. Single Channel Sample Rate	Timing Resolution	Input Range
16 bits	2.00 MS/s	10 ns	$\pm$10 V

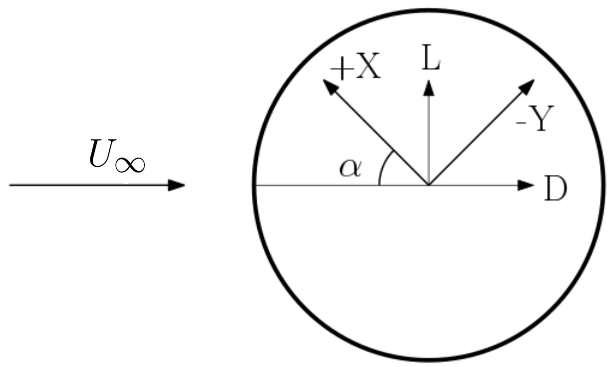

Fig. 2.5: Resolution of Tangential and Normal Forces measured by the load cell into Lift and Drag

2.3 Aerodynamic Forces and Moments on the Test Plates

2.3.1 Lift and Drag

The Coefficient of Lift, C_L, is defined as $\frac{L}{\frac{1}{2}\rho U_\infty^2 S}$, where the Lift force L is measured using the load cell, ρ is assumed to be 1.225 $\frac{kg}{m^3}$, S is the surface area using the average span (300mm) and chord (100mm) and U_∞ is calculated by using Equation 2.4

$$U_\infty = \sqrt{\frac{2\Delta P}{\rho}} \tag{2.4}$$

where ΔP is value of dynamic pressure provided by the Furness Controls differential pressure transducer.

Figure 2.6a shows how the C_L varies with an increase in angle of attack for test plates with chevron depths ($2h$ in Eq 1.16) ranging from 0mm (i.e., a flat plate) to 40 mm. Data was collected over a wide range of angles of attack (0° to 60°) for the 50 mm chevron depth test plate,

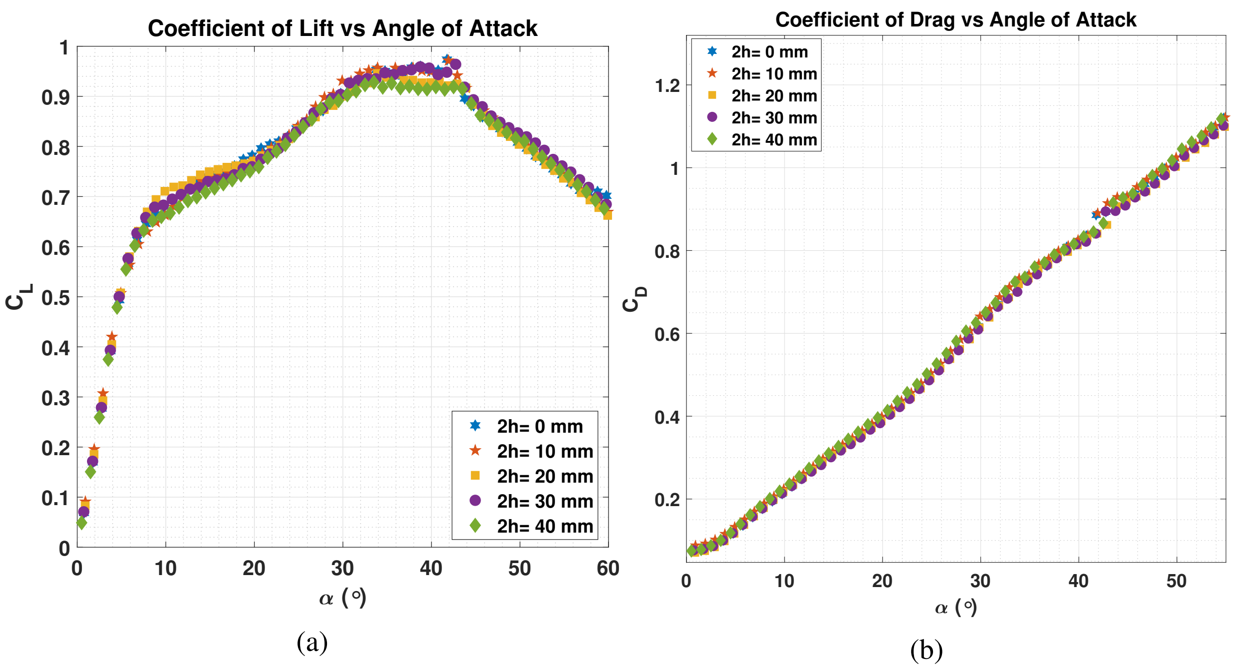

Fig. 2.6: a) Coefficient of Lift (C_L) vs Angle of Attack (α) b) Coefficient of Drag (C_D) vs Angle of Attack (α) for various chevron depths $2h$ over angles of attack from 0° to 60°, showing the regions of flow attachment, separation and stall

unfortunately, the data was not accurate because the mounting disc was found to be touching the floor of the test section, and thus corrupted the data. This was observed solely for the 50mm deep chevron plate for one set of measurements. Smaller sweeps of angles of attack were carried out for all the test plates several times thereafter and are presented in the subsequent sections for the 50 mm plate along with the other five test plates.

From Fig 2.6a, it is observed that the coefficient of lift increases linearly with an increase in the angle of attack between 0° to 5°. Between 5° and 42° angles of attack, the coefficient of lift increases linearly with a slope smaller than the theoretical slopes for a finite wing; this is a region where the flow begins to separate but hasn't completely separated yet. At an angle of attack of about 42°, there is an abrupt drop in C_L and an increase in C_D (=$\frac{Drag}{\frac{1}{2}\rho U_\infty^2 S}$) (see Fig 2.6b), which indicates stall i.e, the flow completely separates from the suction surface of the plates.

Load cell measurements were repeated for angles of attack ranging from 0° to 15° to include data for the $2h$= 50mm chevron plate; the results over 0° to 5° would show how closely the test plates follow the theoretical lift curve slope and can be seen in Fig 2.7. The theoretical lift curve slope from thin airfoil theory (a_0) is $2\pi\alpha$. However, infinite and finite wings have different lift slopes; finite wings have a component of lift force that contributes to the total drag and hence, the total lift is smaller compared to an infinite wing (airfoil) for the same angle of attack. The lift slope (a) for a finite wing, which is smaller than 2π, is given by Eq 2.5.

$$a = \frac{a_0}{1 + (a_0/\pi AR)(1+\tau)} \tag{2.5}$$

where a_0 is the lift slope for an airfoil, which is equal to 2π. The lift cure slope for a finite wing (a), therefore, depends on the aspect ratio as well as the lift distribution which is accounted for by Glauert's factor τ. The typical values of τ range from 0.05 to 0.25 [4]. Since the test plates

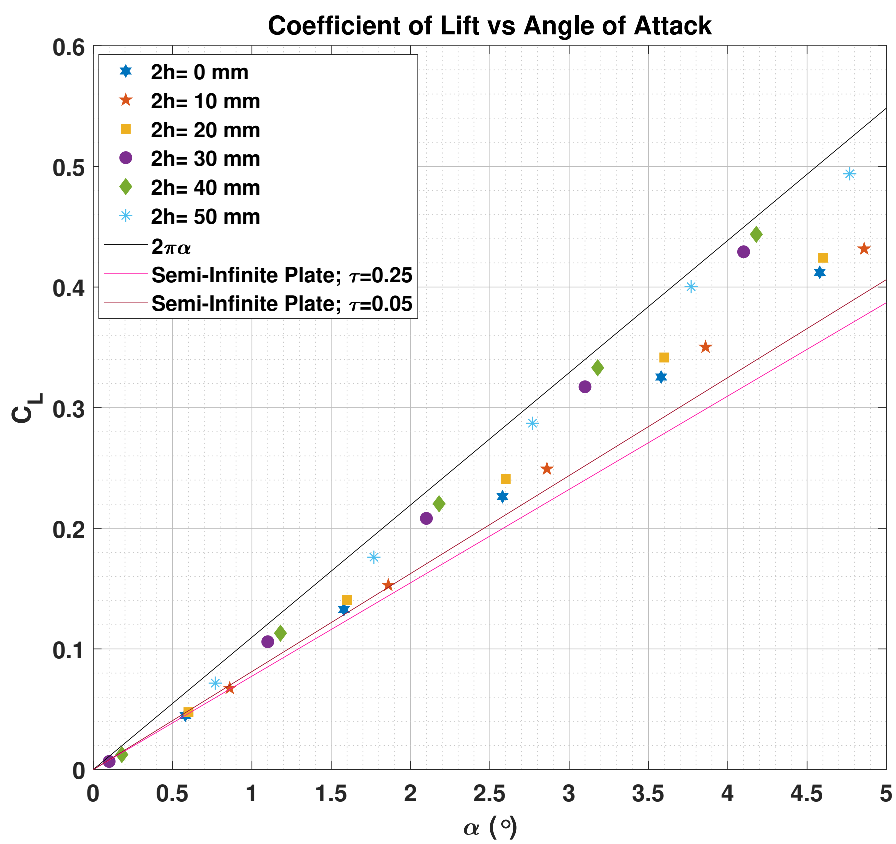

Fig. 2.7: Coefficient of Lift (C_L) vs Angle of Attack (α) for various chevron depths $2h$ over α= 0° to 5°, as compared to the C_L for an infinite plate, a semi-infinite plate with τ= 0.25 and τ= 0.05, for the same range of angle of attack. The deeper chevrons exhibit C_L values closer to the theoretical C_l values for an infinite plate, while the shallow chevron plates and flat plates have C_L values closer to the theoretical semi-infinite plates.

sit flush with the floor of the wind tunnel, they are semi-infinite. We can, therefore, calculate the theoretical lift slope using Eq 2.5 for an aspect ratio of 6 (since the semi aspect ratio of the test plates is 3) and τ= 0.05, which gives a= 5.347. From Fig 2.7, we see that the values of C_L for the test plates lie between the theoretical values for an infinite wing (=2π) and a finite wing with τ= 0.05. It is also noteworthy that the 0mm, 10mm and 20mm deep chevron plates have C_L values closer to the theoretical values for a finite wing and the 30mm, 40mm and 50mm deep chevron plates have C_L values closer to an infinite wing. This can be explained by the fact that an increase in the total span brings the 30mm, 40mm and 50mm deep chevron plates closer to infinite wings as compared to the rest of the test plates.

Fig 2.8 shows the C_L values over angles of attack between 5° to 15°. In this region, the coefficient of lift increases with an increase in angle of attack, with a smaller slope than that of a finite wing. This was also observed by Pelletier and Mueller [33] in their measurement of the forces acting on a flat plate of semi-aspect ratio of 3, with a thickness-to-chord ratio of 1.93%, a 5-to-1 elliptical leading edge and a 3° tapered trailing edge at Reynolds numbers of 80,000 and 140,000. They observed that for low aspect ratios, there was no abrupt stall and C_L either reached a plateau and remained relatively constant or even increased for increasing angles of attack. We speculate that this region is that of separated flow which takes place due to an increasing adverse pressure gradient over the suction surface as the angle of attack increases. Similar results were observed by Pelletier and Mueller for flat plate models with a semi aspect ratio of 0.5 and 1. Through flow visualization in a water tunnel with hydrogen bubbles, they observed that there was a thin region of separated flow at the suction surface near the trailing edge at low angles of attack, which increased to more than 50% of the chord after α=8°. They also observed that the flow did not re-attach to the surface after separation and therefore, the Laminar Separation Region was not present, which was confirmed by the lack of hysteresis. It was confirmed that no hysteresis was observed for the current plates, hence strengthening our belief that the plates are exhibiting a similar separation phenomena in this region.

Aerodynamic hysteresis of an airfoil refers to airfoil aerodynamic characteristics as it becomes history dependent, i.e., dependent on the sense of change of the angle of attack, near the airfoil stall angle. The coefficients of lift, drag, and moment of the airfoil are found to be multiple-valued rather than single-valued functions of the angle of attack in hysteresis loop. To check for hysteresis, we conducted the load cell measurements for the flat plate from angles of attack ranging from 0° and 15° and then again from 15° and 0° at the test speed. From Fig 2.9

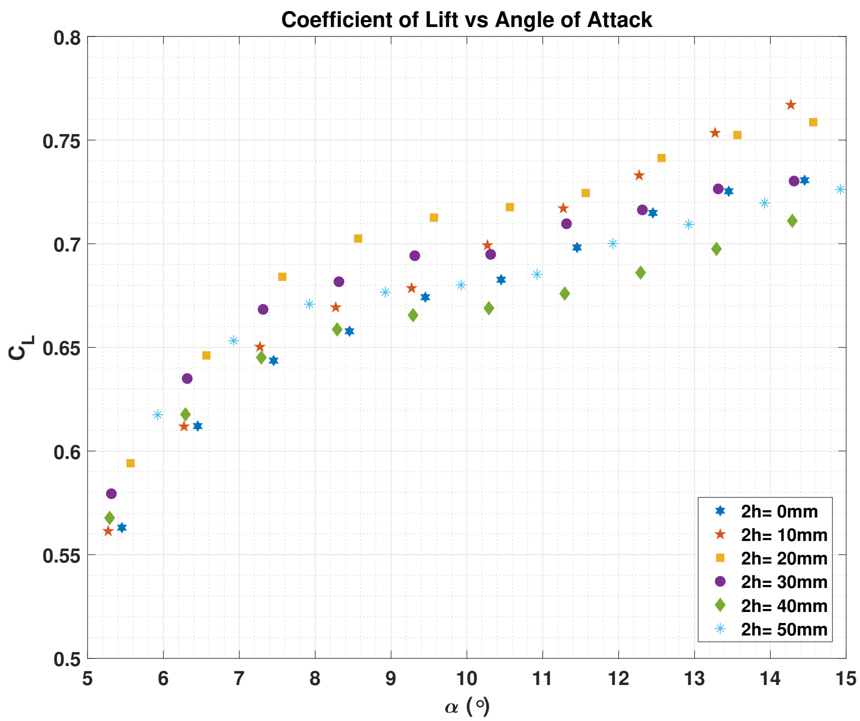

Fig. 2.8: Coefficient of Lift vs Angle of Attack for various chevron depths $2h$ over Angles of Attack between 5° to 15°, indicating a region of flow separation, but not complete stall

it can be seen that the changes in the values of C_L lie within the error bars, which are shown in Fig 2.10.

So far, we have discussed the general trends in lift and drag for all the test plates and identified regions of flow attachment (0° to 5°), separation (5° to 42°) and stall (angles of attack greater than 42°). In the following discussion, an attempt is made to answer the first question raised in the objectives: what is the impact of chevrons on the aerodynamic performance of a flat plate?

To compare the aerodynamic performance of test plates, load cell measurements were taken ten times for each plate for angles of attack ranging from 0° to 10°. This allowed us to take an ensemble average of the coefficients of lift, drag and moments at each angle of attack and define error bars based on the Student's t interval i.e., $\delta = \frac{t_{\alpha/2}\sigma}{\sqrt{n}}$, where $t_{\alpha/2}$ is the inverse of Student's t cumulative distribution function at a confidence levell of 97.5%, σ is the standard deviation of the data and n is the number of data sets (10 in our case). Since the α= 0° is corrected for during post processing, the values of the coefficients were linearly interpolated using the MATLAB function 'interp1' at angles of attack from 0° to 10° in 1° increments.

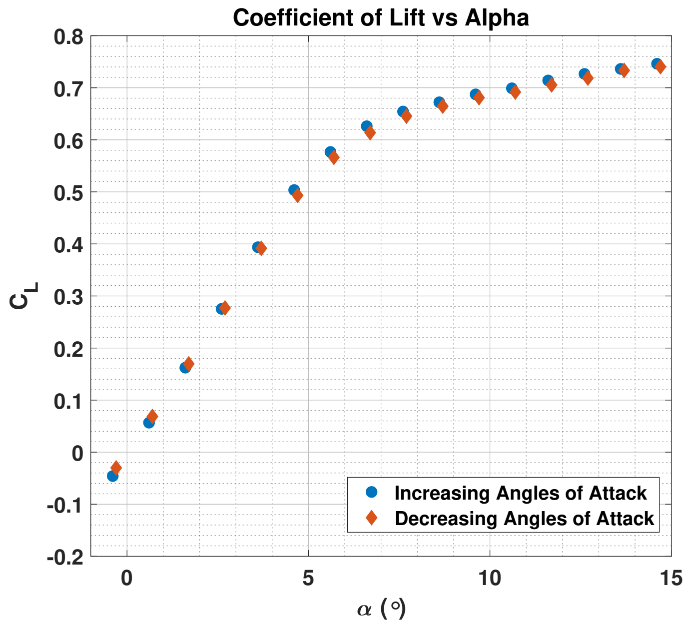

Fig. 2.9: Coefficient of Lift vs Angle of Attack over Angles of Attack between 0° to 15° to check for Hysteresis; the C_L values for a sweep with increasing angle of attack are fairly consistent with those for decreasing angles of attack.

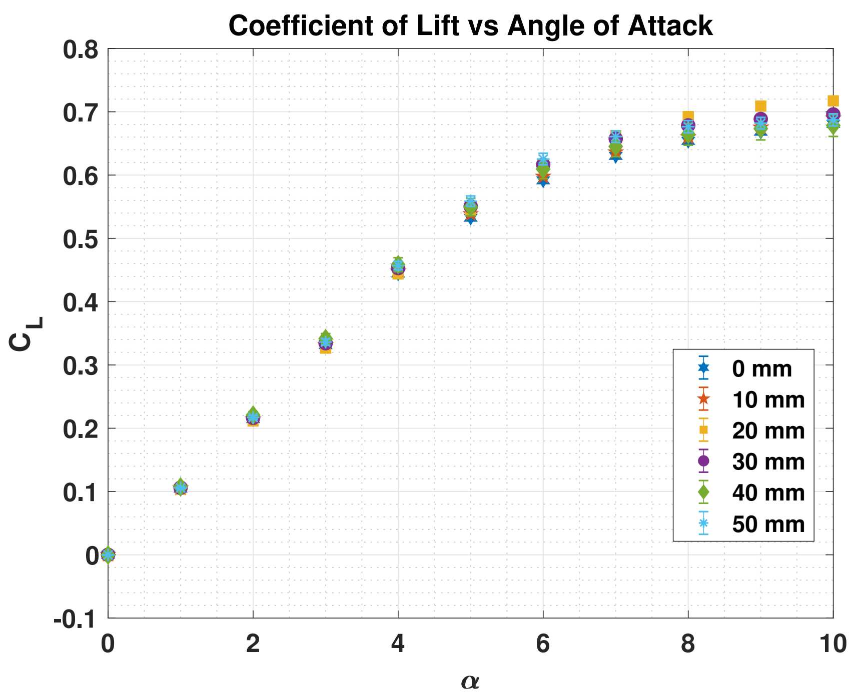

Fig. 2.10: Coefficient of Lift (C_L) as a function of angle of attack (α), for various chevron depths $2h$. Error bars are calculated using Student's t-distribution.

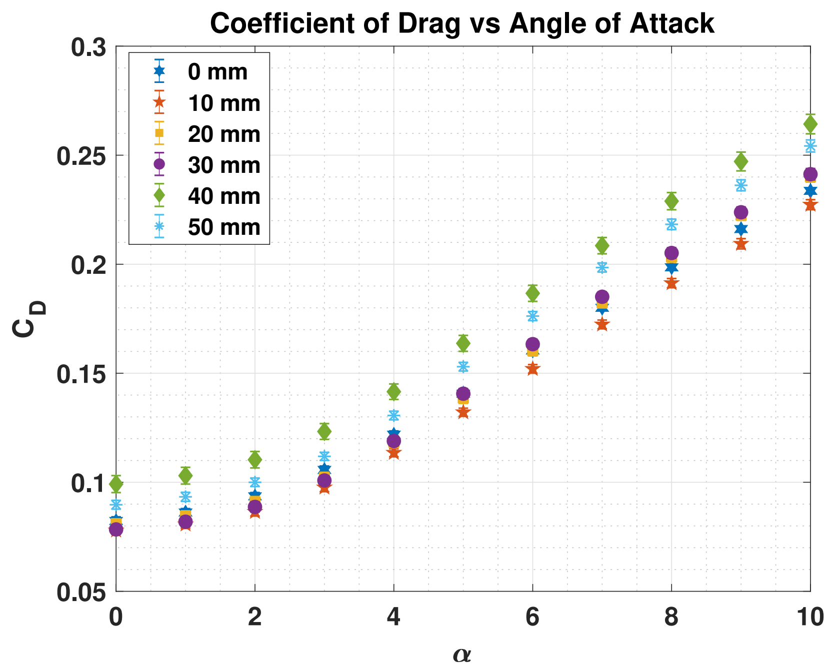

Fig. 2.11: Coefficient of Drag (C_D) as a function of angle of attack (α), for various chevron depths $2h$. Error bars are calculated using Student's t-distribution.

Figure 2.10 shows the C_L values for angles of attack from 0° to 10° for all the test plates with error bars. It is evident that the introduction of chevrons does not significantly alter the lift coefficient of the test plates and that the measurement uncertainty are considerably small (0.0026). We now turn our attention to the coefficient of drag over the same α range, shown in Fig 2.11. Over this range, the average measurement uncertainty in C_D was found to be 0.0023. The drag coefficient of the 10mm, 20mm and 30 mm deep chevron plates is not significantly different from that of the flat plate at angles of attack between 0° to 4°. At angles of attack between 5° and 10°, the 10 mm chevron plate seems to have a lower drag coefficient as compared to the flat plate, while the 20 mm and 30 mm chevron plates show drag coefficients that are similar to that of the flat plate. The 40 mm and 50 mm chevron plates have higher drag coefficient values as compared to the flat plate throughout the range of angles of attack, which can be due to a higher profile drag. In order to confirm this, C_D was plotted against ${C_L}^2$ for 0° to 5° of angle of attack. Note from Eq 1.3, a plot of C_D against ${C_L}^2$ would give a y-intercept of C_{D_0} and a slope of k (=$\frac{1}{\pi ARe}$). From Fig 2.12, it can be seen that that 40 mm and 50 mm deep chevron plates have a higher value of the y intercept i.e., of C_{D_0}. Upon doing a linear fit to the C_D vs C_L^2 data, it was found that the values of k for the chevron plates were not significantly different from the flat

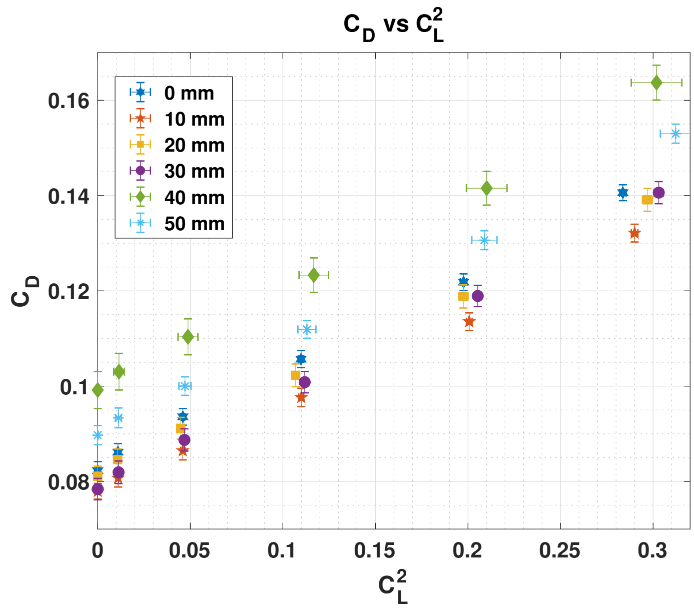

Fig. 2.12: Coefficient of Drag (C_D) as a function of C_L^2,for various chevron depths $2h$. Error bars are calculated using Student's t-distribution.

plate. Table 2.4 shows the values of C_{D_0} and k. This implies that the increase in the total drag

Table 2.4: Values C_{D_0} and k obtained by fitting a straight line

Test Plate	0 mm	10 mm	20 mm	30 mm	40 mm	50 mm
C_{D_0}	0.071	0.075	0.081	0.080	0.099	0.089
k	0.20	0.19	0.19	0.20	0.21	0.20

coefficient seen in the 40 mm and 50 mm deep chevron plates is primarily due to an increase in the profile drag i.e., C_{D_0}. The addition of the chevrons do not have a significant impact on the lift induced drag, which is evident from the insignificant change in the value of k.

Finally, Fig 2.13 shows the aerodynamic efficiency of the test plates with an increase in angle of attack. The aerodynamic efficiency of the 30 mm chevron plate is similar to that of the flat plate throughout the range of angles of attack. The 10 mm and 20mm chevron plate seems to have a higher aerodynamic efficiency as compared to the flat plate at angles of attack above 4°. This can be explained by the slight decrease in the drag coefficient, shown in Fig 2.11. The 40 mm and 50 mm chevron plates have a lower aerodynamic efficiency as compared to the flat plate, which can be explained by the higher profile drag. For all the test plates, the peak aerodynamic efficiency is at an angle of attack of 5°. Table 2.5 shows the values of the peak $\frac{L}{D}$ ratios at 5° for the test plates, as well as the percentage change in peak $\frac{L}{D}$ ratios as compared to a flat plate.

Table 2.5: Peak Aerodynamic Efficiency of all the Test Plates at 5° angle of attack

Test Plate	0 mm	10 mm	20 mm	30 mm	40 mm	50 mm
Peak $\frac{L}{D}$	3.78	4.07	3.92	3.91	3.35	3.65
δ ($\pm$)	0.039	0.049	0.063	0.062	0.098	0.051
% $\Delta\frac{L}{D}$	0	7.7	3.7	3.4	-11.4	-3.4

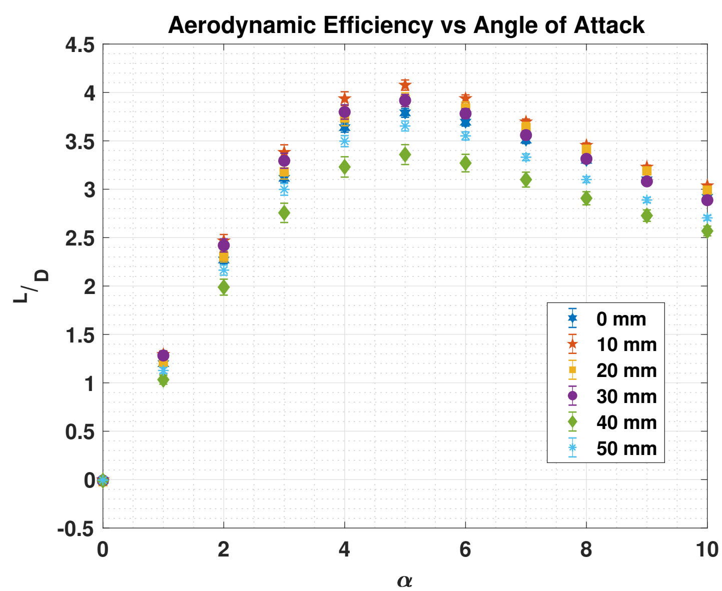

Fig. 2.13: Aerodynamic Efficiency ($\frac{L}{D}$) as a function of angle of attack (α), for various chevron depths $2h$. Error bars are calculated using Student's t-distribution.

A clear pattern is not established between the aerodynamic efficiency and the chevron depth, but it has been observed that the addition of shallower chevrons (with depths of 10mm and 20mm) either improves the aerodynamic efficiency of a flat plate or does not alter it (in the case of the 30 mm plate). Deeper chevrons have a worse aerodynamic efficiency than the flat plate, particularly the 40mm deep chevron plate due to an increase in drag.

2.3.2 Moments

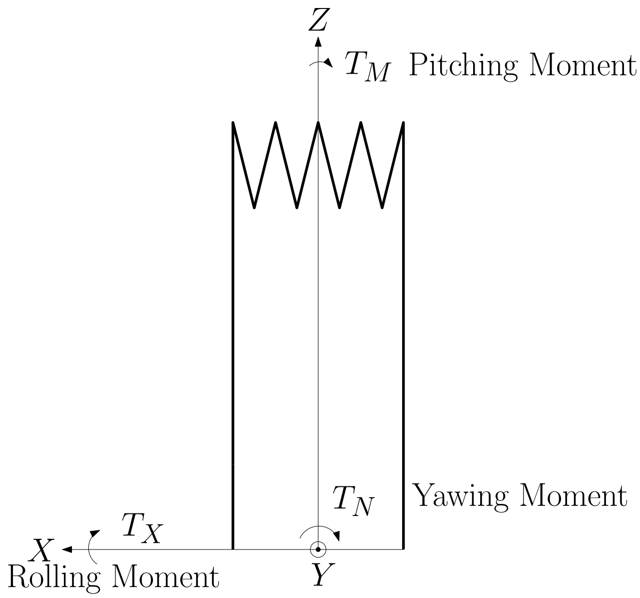

Fig. 2.14: Moments acting on a plate, where X, Y and Z axes are those of the load cell

Fig 2.14 shows the moments acting on the test plates with respect to the axes of the load cell. The moments acting about the X axis would be roll, Y axis would be yaw and Z would be pitch.

The rolling moment is created by the Lift force acting on the test plates, as depicted in Fig 2.15, which shows that the product of the lift and the moment arm (x) would be the Rolling moment. Fig 2.16 shows how the coefficient of roll moment (=$\frac{M_{pitch}}{\frac{1}{2}\rho U_{\infty}^2 Sc}$) varies over angles of attack ranging from 0° to 10° for all the test plates. No appreciable change was observed in the general trend of the roll moments on the test plates. Theoretically, the rolling moment at an angle of attack of 0 should be zero, as the lift force is zero at a 0° angle of attack. The flat plate and 10mm deep chevron plate exhibit non-zero rolling moments, which could be due to defects in the plate themselves (for example, a small bend in the plate).

The Pitching Moment is taken about the Z axis of the load cell and determines the longitudinal stability of an aircraft i.e., the ability of the aircraft to return to equilibrium if the angle of attack changes suddenly. The criterion for longitudinal stability is that the value of C_M should decrease with an increase in α i.e., the slope of the C_M vs α plot must be negative [6]. Fig 2.17 shows the coefficient of pitching moment for all the test plates about half chord. Before flow separation *i.e.*,

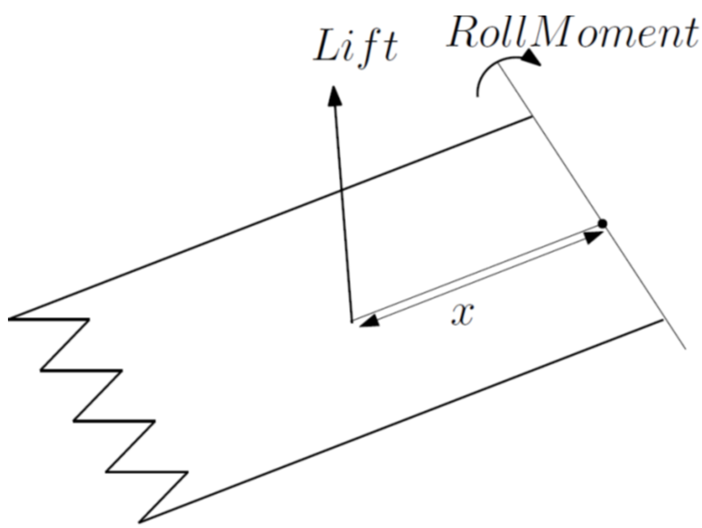

Fig. 2.15: Rolling Moment created by the lift force, where x is the moment arm

at angles of attack less than 5°, $\frac{\partial C_M}{\partial \alpha}$ is negative (the slope of C_M vs α is found to be -0.021/deg), which implies that the test plates are longitudinally stable until the flow begins to separate. The

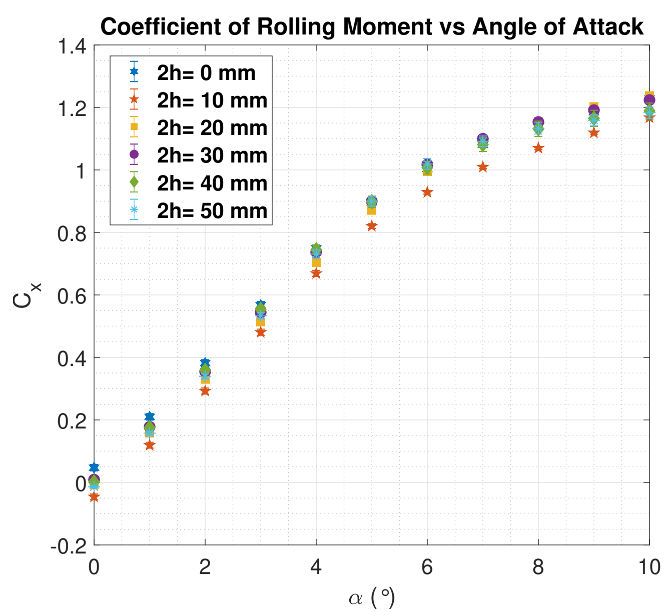

Fig. 2.16: Coefficient of Rolling Moment (C_X) as a function of angle of attack (α),for various chevron depths $2h$. Error bars are calculated using Student's t-distribution.

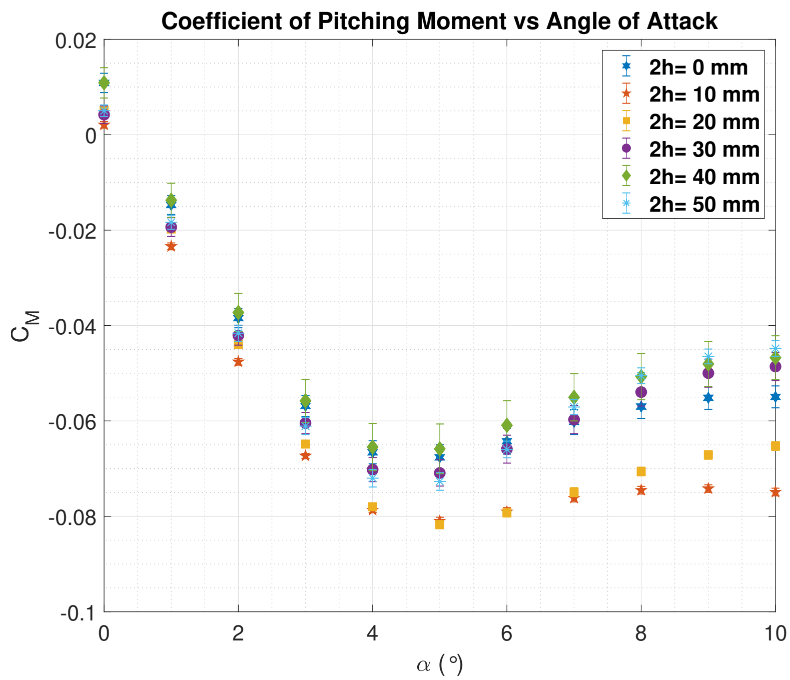

Fig. 2.17: Coefficient of Pitching Moment (C_M) as a function of angle of attack (α),for various chevron depths $2h$. Error bars are calculated using Student's t-distribution.

value of C_{M_0} lies between 0 and 0.015, which could be due to a small misalignment of the model or due to the plates not being perfectly symmetric.

The yawing moment is the moment taken about the Y axis of the load cell. It is equal to the product of the Drag force and the moment arm (y), which can be seen in Fig. 2.18. Figure 2.19

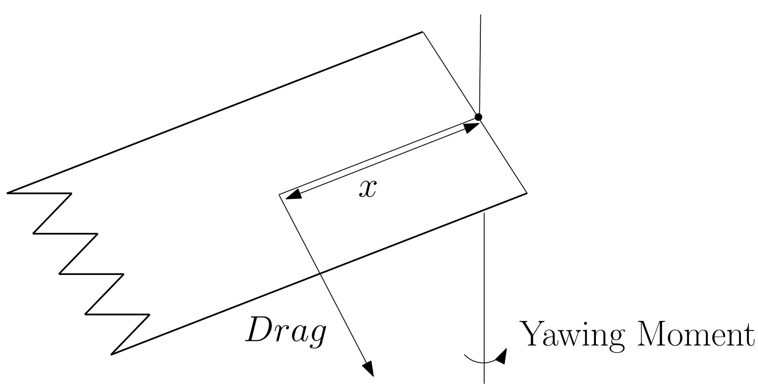

Fig. 2.18: Yawing Moment created by the drag force, where x is the moment arm

shows the coefficient of yawing moment ($=\frac{M_{yaw}}{\frac{1}{2}\rho U_\infty^2 Sc}$) for all the test plates about half chord. As the

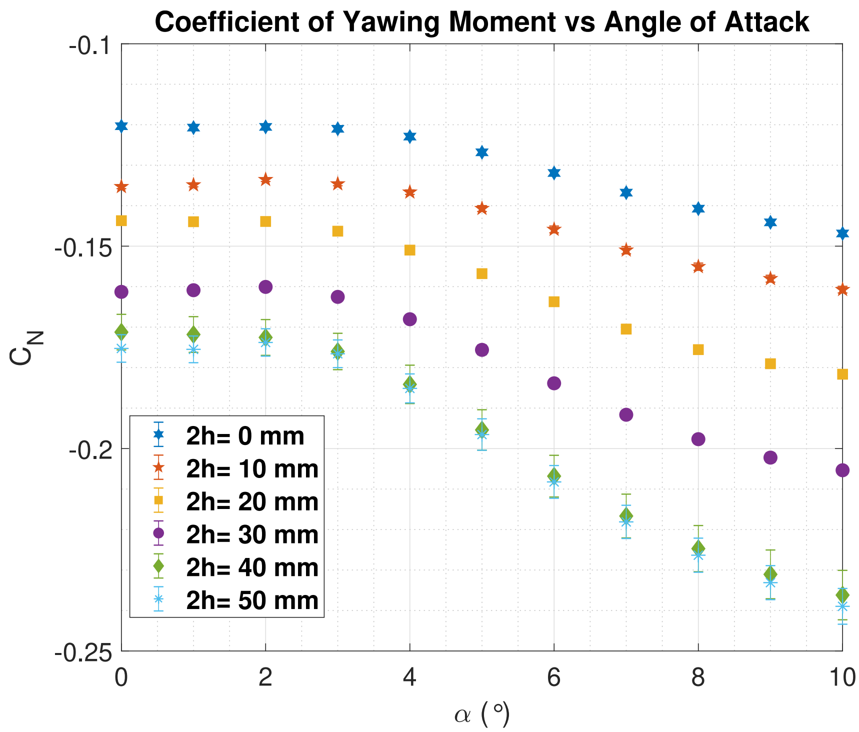

Fig. 2.19: Coefficient of Yawing Moment (C_N) as a function of angle of attack (α),for various chevron depths $2h$. Error bars are calculated using Student's t-distribution.

chevron depth increases from 10mm to 40mm, the coefficient of yawing moments becomes more negative at a 0° angle of attack and remains fairly constant up to 4°. Between 4° and 10°, the coefficient of moment decreases with an increase in the angle of attack. The 50mm plate shows the same trend, but shows roughly the same values of C_N as the 40mm plate. The value of the moment arm (x) can then be worked out using Eq 2.6.

$$
\begin{gathered}
M_{yaw} = Dx \\
\frac{M_{yaw}}{\frac{1}{2}\rho U_\infty^2 Sc} = \frac{L}{\frac{1}{2}\rho U_\infty^2 S}\frac{x}{c} \\
C_N = C_D\frac{x}{c}
\end{gathered} \tag{2.6}
$$

Fig 2.20 shows how the moment arm varies for all the test plates for a given angle of attack. The moment arm shown here is normalized with the span of each plate. One can see that the moment arm of each of the chevron plates at 0° is larger than the flat plate; in the case of the 10mm chevron plate, the moment arm is nominally higher. It increases with an increase in the

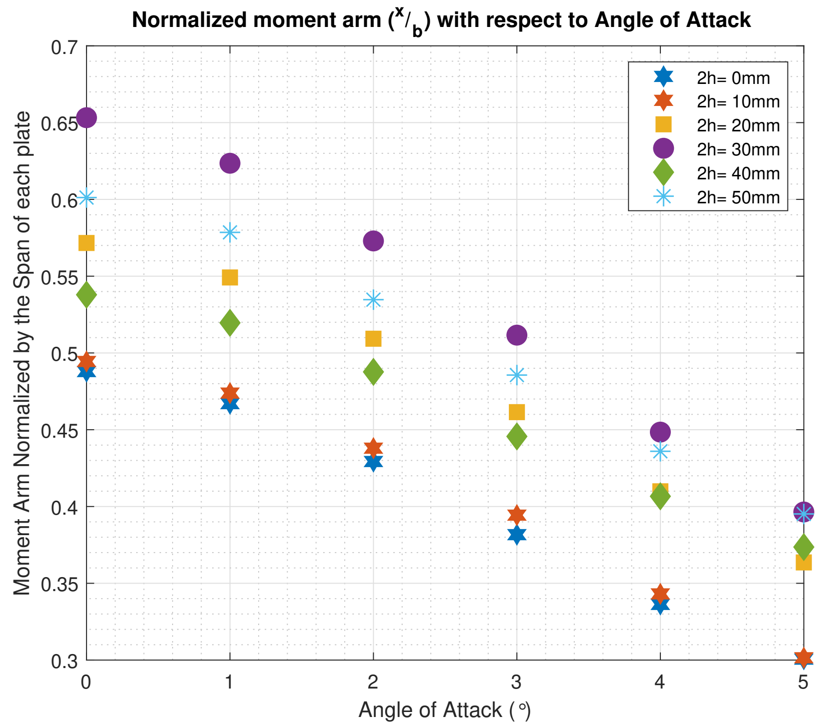

Fig. 2.20: Variation of the Normalized Moment Arm with respect to the Angle of Attack

chevron depth up till the 30mm chevron plate, with a $\frac{x}{b}$ value of 0.65. For the 40mm chevron plate, the normalized moment arm shows a sudden drop ($\frac{x}{b}$ = 0.53) and it increases again for the 50mm chevron plate to $\frac{x}{b} = 0.6$. The large drop in the moment arm of the 40mm plate can be attributed to its high value of profile drag (C_{D_o}= 0.994), but the exact reason for this large drag exhibited by the 40mm plate is unclear. The lift and drag forces act a point on the wing known as the Center of Pressure. The location of the center of pressure is determined by the pressure field around a lifting surface, which in turn, depends on the angle of attack. A change in the moment arm of the chevron plates at a given angle of attack indicates that the point where the drag acts on the plates (or the center of pressure) has shifted further towards the tip of the wing as compared to a plate without chevrons. One can then speculate that this shift in the center of pressure could be due to a shift in the position of the tip vortex itself.

2.4 Interim Summary

The objective of this section was to investigate how the presence of chevrons with varying depths affects the aerodynamic forces and moment acting on the test plates. By measuring time resolved forces and moments, we were able to find angles of attack where the flow remains attached ($0°$ to $5°$), where it begins to separate ($5°$ to $42°$) and finally, where it separates completely ($\alpha > 42°$). We then focus the bulk of our attention to the ranges of angle of attack where the flow remains attached, as this region is one where an aircraft or drone would fly. We find that the presence of chevrons does not significantly affect the coefficient of lift for all the test plates. The coefficient of drag seems to be higher for test plates with 40 mm and 50 mm deep chevrons, while the 10 mm, 20 mm and 30 mm have a slightly lower drag coefficient than the flat plate. The peak aerodynamic efficiency of the 10mm, 20mm and 30mm deep chevron plates was found to be 7.7%, 3.7% and 3.4% higher, respectively, than the flat plate at an angle of attack of $5°$. Meanwhile, the 40mm and 50mm plates had a significantly lower efficiency by 11.4% and 3.4%, respectively, as compared to the flat plate. This sudden drop in efficiency of the deeper chevron plates was due to an increase in the profile drag. Finally, the coefficients of rolling and pitching moments are not significantly affected by the presence of the chevrons, but the yawing moment at a $0°$ angle of attack becomes more negative with an increase in the chevron depth. The moment arm was then computed and was found to increase with an increase in the chevron depth up to the 30mm chevron plate. The 40mm chevron plate saw a sudden drop in the moment arm (although, it was still larger than that of the flat plate) and the 50mm chevron plate saw an increase in the moment arm, as compared to the 40mm plate.

Having determined the angle of attack corresponding to the maximum aerodynamic efficiency of the test plates as $5°$, we turn our attention to the tip vortex itself and how its structure is altered due to the presence of the chevrons. This is important to determine how chevrons affect the tip vortex as it forms and develops.

Chapter 3

Analysis of the Tip Vortex

3.1 Introduction

In the previous chapter, the aerodynamic forces and moments on the chevron plates were compared to the flat plate. In this section, we study the downstream development of the tip vortex for each of these plates. The motivation is to address the last two objectives presented in Chapter 1: what happens to the structure of the tip vortex due to the presence of chevrons? How does the vortex develop as we go downstream of the wing? The former is important as it gives an insight into the shape and size of a tip vortex. The latter addresses the issue of a minimum separation between aircraft during take-off and landing: a tip vortex that decays faster would require a smaller separation between two aircraft and therefore, help in increasing airport capacity.

3.1.1 Structure of the Tip Vortex

A tip vortex can be characterized by its tangential velocity (U_θ) and radial velocity (U_r). Fig 3.1 shows how the tangential and radial velocities can be described by the u, v and w velocity components in cartesian coordinates of the test section, using Eq 3.1 and 3.2.

$$U_\theta = W cos\theta + V sin\theta \tag{3.1}$$

$$U_r = W sin\theta - V cos\theta \tag{3.2}$$

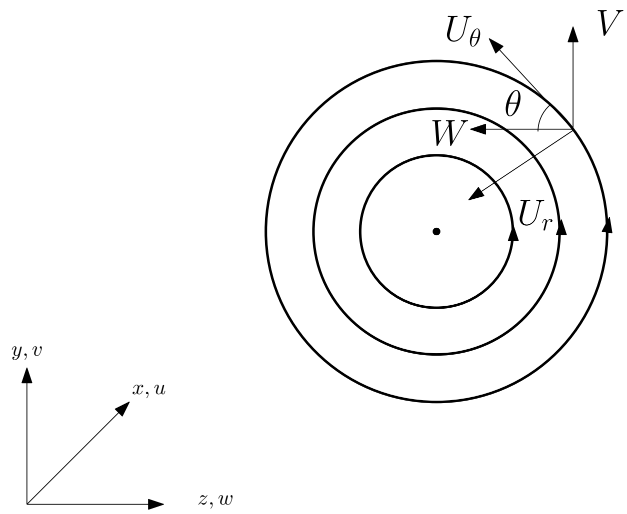

Fig. 3.1: U_θ and U_r using Cartesian velocity components

The planar cross-section of a tip vortex is divided into two tiers: an inner tier, or the core, where the tangential velocity, U_θ is proportional to the radial distance from the vortex center, r up to a critical radius called the Core Radius, r_c. In the outer tier, the tangential velocity is inversely proportional to the distance from the vortex center. The radial velocity (U_r) is normally negligible [34] in the tip vortex.

The formation of a tip vortex around a lifting surface, as described by Green [34], can be explained using three different arguments:

1. The pressure difference between the suction and pressure surfaces of the wing that accelerate the oncoming flow around the wing tip. This was explained in more detail in Section 1.2.

2. Tip vortices form a bridge between the starting vortex and the bound vortex: According to the Kutta-Joukowski theorem, L=$\rho U_\infty \Gamma$, where Γ is the circulation around the lifting body. In the case of an airfoil, the value of Γ is such that the flow leaves the trailing edge smoothly. This is known as the Kutta condition. Based on experimental results from Prandtl and Tietjens [4], it was found that when the flow begins to develop around an

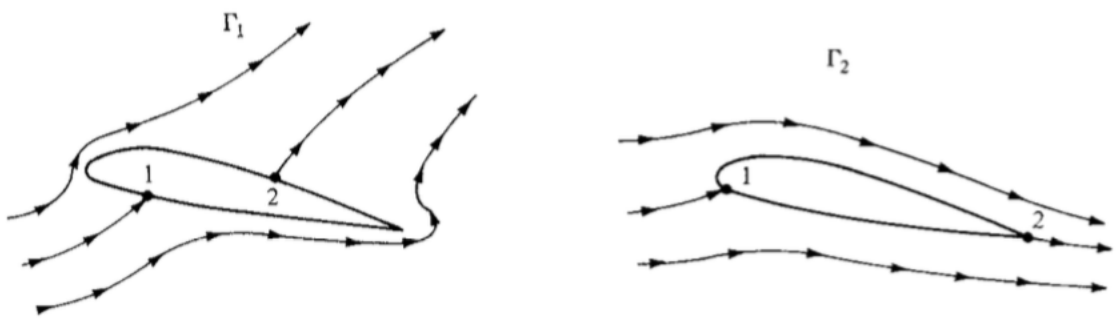

Fig. 3.2: Different values of circulation over an airfoil, where points 1 and 2 are stagnation points [4]

airfoil, it curls around the sharp trailing edge of an airfoil and leads to high velocity and therefore, vorticity gradients, as shown in Fig 3.2. As a result, the stagnation point (Point 2 in Fig 3.2) shifts towards the trailing edge. However, in the first few moments when the flow around an airfoil is developing, the high vorticity leads to the formation of a vortex called the starting vortex. This starting vortex is flushed downstream as the stagnation point shifts to the trailing edge. According to Kelvin's circulation theorem, the net circulation about a closed path must be zero. Therefore, an equal and opposite vortex is formed around the airfoil. In the case of a finite wing, this vortex is the bound vortex. Finally, according to Helmholtz laws, a vortex cannot end in a fluid and the starting and bound vortices are connected by the tip vortices. This is illustrated in Fig 3.3.

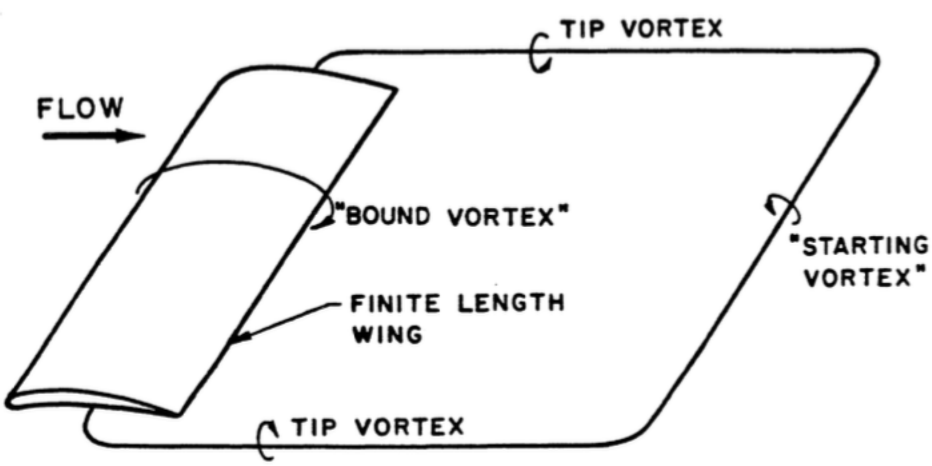

Fig. 3.3: Tip vortex as a bridge between the bound vortex and starting vortex [34]

3. The presence of a shear layer near the wing-tip: The velocity vector over the surface of the wing is not parallel to the free stream velocity vector, leading to vorticity due to the presence of velocity gradients, thereby forming tip vortices.

However, the actual formation and downstream development of tip vortices involve complex processes and detailed studies have been conducted on the same. Chow *et al.* [35] presented a study on the initial development of a tip vortex around a rounded wing-tip and found that tertiary and secondary vortices merge into a primary vortex within one chord length from the trailing edge. They also found that this primary vortex becomes axis-symmetric, with the axial velocity (u in Fig 3.1) higher than the free-stream velocity. Green and Acosta [36] found that this axial velocity surplus reverses and becomes a velocity deficit at 10c downstream of the wing. However, some authors show that the deficit forms at the trailing edge, in the case of Stinebring, *et al.* [37], at a downstream distance of 0.073c. Therefore, it has been experimentally found that the axial velocity within the vortex core can be 'wake' like (or have a deficit with respect to the free stream) or be 'jet' like (higher than the free stream velocity). Batchelor [38] showed analytically that the nature of the axial velocity is determined by the balance between the radial circulation gradient and the dissipation of momentum. Anderson and Lawton [39] found that the axial velocity depends on the angle of attack of the wing and the tip shape: wings with a rounded tip and a high angle of attack lead to a jet like flow, as opposed to wings with a square tip and at low angle of attack, which form a wake like axial velocity profile.

It has been observed that the formation and development of tip vortices is affected by wing shape, tip geometry and the nature of the boundary layer over the wing itself. Sarpkaya [1] observed that the radius of the tip vortex generated by a rectangular planform that is square cut is 30% larger than that of the same planform with a rounded tip. Shekarriz *et al.* [40] found that this increase in the radius of the tip vortex is due to the formation of the primary vortex from several shear layer vortices that are generated at the tip, which merge downstream. Stinebring *et al.* [37] found that the axial velocity in the core decreases and core size increases on roughening a smooth, round wing-tip. Giuini [2] showed that a squared wing tip produces a higher number of smaller vortices as compared to rounded tips. Bailey *et al.* [41] showed that squared wing tips form a tip vortex due to three distinct vortices merging together. Iversen [42] showed that tip vortices show little growth or decay over the first 20 wing spans downstream of the wing. Thus, the tip vortex shed from one wing develops independently from its counterpart shed by the opposite wing. Finally, it was found by Crow [10], that these tip-vortex pairs will merge and form a single counter-rotating vortex pair, which develops sinusoidal instabilities (or Crow's instabilities) and forms a vortex ring that ultimately dissipates. Sarpkaya and Daly [43] found that this dissipation is rapid and Chevalier [44] found that an aircraft which is in close proximity of a wake that has already formed a vortex ring would face a very small risk, as the vortex ring was found to dissipate within 10-20 seconds of its formation.

As a result, there has been a concentrated effort in developing methods that would aid in faster dissipation of tip vortices to address the issue of spacing between aircrafts at airports. Jacob *et al.* [45] used jets in the wing-tips to introduce instabilities in the tip vortex to facilitate their dissipation and found that the tip vortex pair had an increased separation and an increase in the growth rate of the vortex core. Lee *et al.* [46] proposed blowing air in the span-wise direction from the wing tip through slots. As mentioned earlier, the primary vortex is formed from flow that separates from the wing-tip. Blowing air in the span-wise direction deflected the flow around the wing-tip outwards and increase the effective span. It also displaced the tip vortex outwards. Heyes and Smith [47] combined the two effects *i.e.*, they investigated the efficacy of blowing air through slots in the wing-tips periodically. By subjecting tip vortices to periodic perturbations at different mass flow rates of air, it was found that the vortex core was larger, peak tangential velocities were lower and axial velocity deficit was larger, as compared to a wing without pulsed jets of air. The exact amount of increase in the vortex core radius and axial velocity deficit and decrease in the peak tangential velocities was a function of the mass flow rate of air through the jets and the frequency of pulsation: a higher mass flow rate of air lead to a weaker tip vortex. Another method that has been found to be effective in increasing vortex dissipation rate is increasing the free stream turbulence. Sarpkaya and Daly [43] found that a pair of tip vortices decay at a faster rate when surrounded by turbulence due to vortex bursting, as compared to when the vortex pair is surrounded by weak turbulence, where Crow's instabilities cause the demise of the vortex pair. Ahmadi-Bloutaki [48] also found that increasing the free stream turbulence to 4.6% from 0.5%, using a grid turbulence generator, lead to the formation of a tip vortex on a NACA 0015 wing section, that had a larger core radius and smaller peak tangential velocity with an increase in streamwise distance.

It is well established that vortex formation and downstream development is affected by the wing-tip geometry and that modifying the tip geometry could potentially aid in the faster dissipation of tip vortices. This section focuses on how introducing chevrons of varying depths at the wing-tips of a flat plate would affect the tip vortex. To capture the tip vortex and study its downstream development, hot-wire anemometry was used. Hot wire anemometers are intrusive flow measurement devices *i.e.*, they are placed in the flow field to measure the velocity components of the flow. A concern while using hot wires to capture a tip vortex is vortex wandering. Vortex wandering is a low-frequency motion of the vortex core, which could be self induced or due to free stream turbulence. Bandyopadhyay et al [49] found that vortex wandering is due to instabilities within the vortex core that cause packets of fluid in the core to be pushed out. Baker *et al.* [50] proposed that the wandering is a consequence of free stream turbulence. Devenport *et al.* [3] found that the effects of wandering are very small at downstream distance of $\frac{x}{c} < 1$ and need not be corrected for. Since this study captures the tip vortex at downstream distances of $\frac{x}{c}$ = $0.5, 1, 1.5, 2, 2.5$ and 3, it becomes important to correct for vortex wandering. The following section looks at this in more detail.

3.1.2 Vortex Wandering and Correction

Vortex wandering is a low frequency motion of the vortex which results in errors in the mean velocity and turbulence measurements made with fixed probe, as shown in Fig 3.4. The fixed probe may measure the average vortex center to be at a point (the origin in Fig 3.4), but since the vortex is moving, it may, at a given instant of time, be at a position different from what the fixed probe measures on average (y_v, z_v in Fig 3.4). Accurate measurements of the tangential and

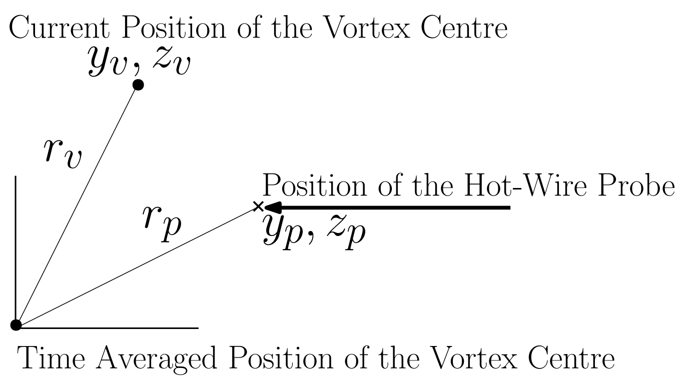

Fig. 3.4: Vortex Wandering while using a fixed probe, adapted from [3]

axial directions (z and x, respectively) require velocity measurements in the frame of reference that moves with the wandering. A fixed probe, however, measures velocities in a fixed frame of reference. Devenport *et al.* [3] devised the following method to correct the velocities measured by a fixed probe for wandering:

1. The measured profiles of axial and tangential velocities along the y=0 were fitted with families of curves based on the Lamb-Oseen vortex, given by Eq 3.3. Coefficient D_i was found through a non-linear least square curve fit of the time averaged velocity profile (measured by using a hot wire probe) by using the MATLAB function 'lsqcurvefit'. The coefficient c_i defined the radial scale and to avoid complex results, was kept above $[2{\sigma_z}^2(1-e^2)]^{\frac{1}{2}}$.

$$U_\theta(0, z_p) = \sum_{i=1}^{n} \frac{D_i}{z_p} \left[1 - exp\left(\frac{-{z_p}^2}{c_i}\right)\right] \tag{3.3}$$

   The number of terms n for the series fit was chosen to be half the number of measured points, based on the recommendation of Devenport *et al.* [3].

2. The position of the vortex center (y_v, z_v) was assumed to be given by a non-isotropic Gaussian probability density function described by Eq 3.4, where σ_y and σ_z are assumed to be equal to the root mean square wandering amplitudes and e is the correlation coefficient, given by $\frac{\overline{vw}}{\sigma_v \sigma_w}$, where $\overline{vw}$ are the velocity fluctuations and σ_v, σ_w are the standard deviations of the velocity signals. The correlation coefficient is that of the Reynolds stresses to ensure that the vortex axis and the principal axis of the Reynolds stresses are aligned, which was required by Devenport *et al.*

$$P_v(y_v, z_p) = \frac{1}{2\pi\sigma_y\sigma_z(1-e^2)} exp\left[\frac{-1}{2(1-e^2)}\left(\frac{{z_v}^2}{{\sigma_z}^2} + \frac{{y_v}^2}{{\sigma_y}^2} - \frac{2e y_v z_v}{\sigma_y \sigma_z}\right)\right] \tag{3.4}$$

   For the first iteration, the values of e, σ_y and σ_z were guessed by the user.

3. The corrected tangential velocity profiles, $U_\theta(r)$, were determined by using Eq 3.5, where a_i and B_i are given by Eq 3.6 and 3.7, respectively.

$$U_{\theta corrected} = \sum_{i=1}^{n} \frac{B_i}{r} \left[1 - exp\left(\frac{-r^2}{{a_i}^2}\right)\right] \tag{3.5}$$

$${a_i}^2 = \frac{1}{2}{c_i}^2 - {\sigma_y}^2 - {\sigma_z}^2 + \frac{1}{2}\left[(2{\sigma_y}^2 + 2{\sigma_z}^2 - {c_i}^2)^2 - 16{\sigma_y}^2{\sigma_z}^2(1-e^2) + 8{\sigma_y}^2 c_i^2\right]^{1/2} \tag{3.6}$$

$$B_i = D_i(2{\sigma_y}^2 + {a_i}^2) / \left[(2{\sigma_y}^2 + {a_i}^2)(2{\sigma_z}^2 + {a_i}^2) - 4e^2{\sigma_y}^2{\sigma_z}^2\right]^{1/2} \tag{3.7}$$

4. Using the corrected velocity profiles and the pdf, $\overline{v_c w_c}$ at the center, y_v=0 and z_v=0, was determined using Eq 3.8, where $\overline{v_c w_c}$ are the corrected fluctuating velocity components at the vortex center.

$$\overline{vw_c} = \iint_{-\infty}^{\infty} P_v(y_v, z_v)V_c(0-y_v, 0-z_v)W_c(0-y_v, 0-z_v)dydz - V_c(0,0)W_c(0,0) \tag{3.8}$$

Similar expressions were used to compute $\overline{{v_c}^2}$ and $\overline{{w_c}^2}$ at the center. These calculated corrected values of Reynolds stresses were compared to the values of Reynolds stresses measured at the center using the hot wire probe and new values of σ_y, σ_z and e were calculated using Eq 3.9, 3.10 and 3.11, respectively.

$${\sigma_{y,new}}^2 = {\sigma_{y,old}}^2 \overline{{w_{meas}}^2} / \overline{w_c}^2 \tag{3.9}$$

$${\sigma_{z,new}}^2 = {\sigma_{z,old}}^2 \overline{v_{meas}}^2 / \overline{v_c}^2 \tag{3.10}$$

$$e_{new} = \frac{\overline{vw}_c}{\sigma_{y,new}\sigma_{z,new}} \tag{3.11}$$

5. Steps 1 to 4 are repeated until the difference between the measured and corrected σ_y, σ_z, $\overline{v^2}$, $\overline{w}^2$ and $\overline{vw}$ (or the relative error) was less than 0.1%.

This analytical method was validated by Heyes et al [51], who studied the tip vortex in free stream turbulence using PIV, and confirmed Devenport *et al.*'s assumption that the wandering of the tip vortex followed a non-isotropic Gaussian pdf. Furthermore, they found that failure to account for vortex wandering leads to up to a 12.5% over-prediction of the core radius and a 6% under prediction of the peak tangential velocity. Measurements taken by using fixed probes, therefore, need to be corrected for wandering. Another issue with the use of an intrusive flow measurement device like the hot wire is that the probe could perturb the tip vortex and cause it to wander. However, Devenport *et al.* [3] found the tip vortex to be insensitive to the introduction of a fixed probe and found the contribution of the presence of a hot wire to wandering to be minimal.

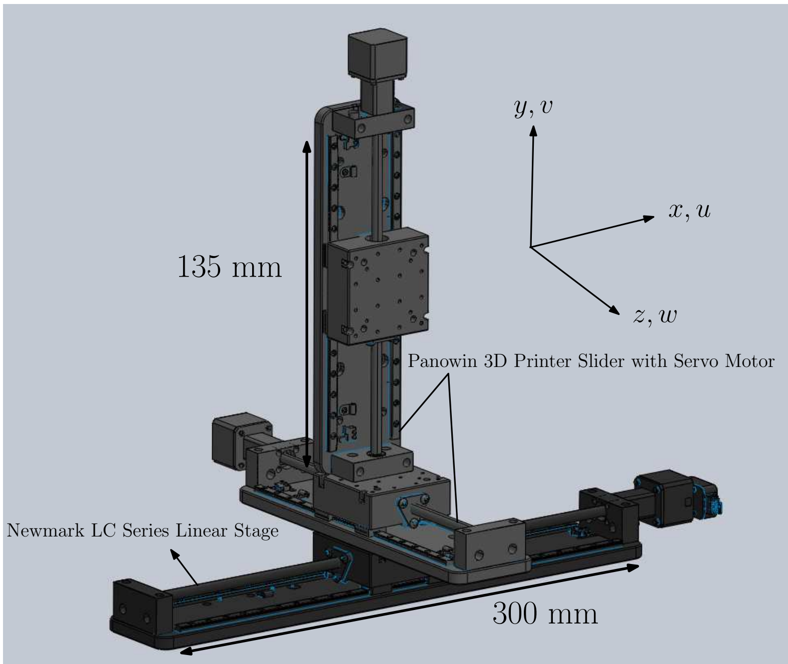

Fig. 3.5: Three linear stages used to move in the x, y and z directions in the test section

3.2 Experimental Setup

3.2.1 Wind Tunnel Setup

The mounting disk for the test plates was the same as the one described in Sec 2.2.3. To measure the tip vortex downstream of the test plates, three linear stages were used to allow motion in the x, y and z directions, as shown in Fig 3.5. A Newmark LC Series 300mm travel length linear stage was screwed into the floor of the test section of the wind tunnel, using four 1/4 inch wood screws, 400mm downstream of the edge of the chord of the test plates. It was controlled using the Newmark Motion Controller and enabled motion in the axial (x) direction. To move the hot-wire in the y and z directions, two Panowin 3D Printer Slider with 17HS4401 Motion King Stepper Motor and a travel length of 135 mm were used. The general specifications of the stepper motors are provided in Table 3.1. The stepper motors were controlled using a TB6600 Stepper Motor Driver Controller, which supports micro-steps and current control. Since the stepper motors were rated for 1.3 A, the micro stepper was set to 1.0 A of current control and a micro step value of 4 (Step Angle=Motor Step Angle/Micro Step; in our case, $\frac{1.8°}{4}$=$0.45°$) through

Table 3.1: Specifications of the Motion King Stepper Motor

Step Angle (deg)	Rated Current (A)	Step Accuracy
1.8	1.3	$\pm 5\%$

DIP switches on the controller. The controller was, in turn, connected to the NI-USB 6363 DAQ unit, which was further connect to a computer. The enable control, number of micro-steps and direction of motion of the motor could be input through a LabVIEW code. The linear stages were calibrated and it was found that 7675 steps make the traverse move over the entire travel range, giving a resolution of 0.0175mm. The printer slider in the y direction was mounted on the other slider (in the z direction; see Fig 3.5) through four M3 Hex Head, 5 mm long screws. Finally, the printer slider in the z direction was mounted onto the Newmark LC linear stage through a 6 mm thick aluminium plate with four M6, flat head, hex drive, 5mm long screws on the Newmark stage end and four M3 flat head, hex drive, 5 mm long screws on the Panowin printer slider end.

A 10mm thick plastic bar was mounted on the linear stage in the y direction using five M3 flat head, hex drive screws , as shown in Fig 3.6. This bar, in turn, was connected to a 400 mm long bar through three M6, flat head, hex drive, 30 mm long screws. The length of 400mm was chosen as it was deemed an appropriate distance between the hot wire and the mechanism of the stepper motors, which could add to the electrical noise. A slot for a HiTec HS-85BB Servo Motor was milled into this bar. The Servo motor specifications are presented in Table 3.2

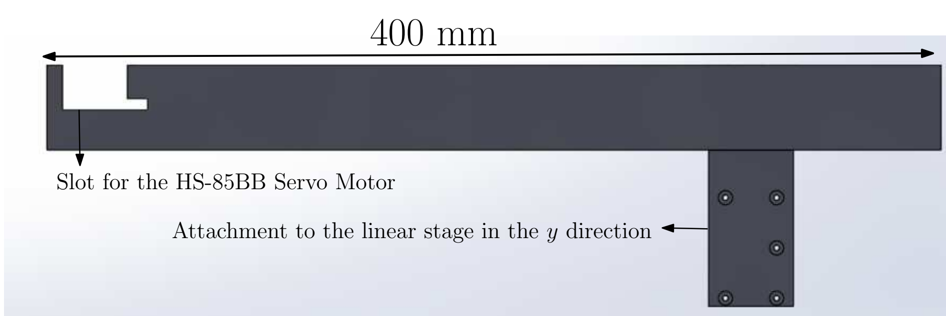

Fig. 3.6: Attachment of bars to the linear stage in the y direction

One servo motor was mounted into the slot in the bar using two M3, hex drive, flat head, 5mm long screws. This servo allowed for yawing motion of the probe holder. The second servo was

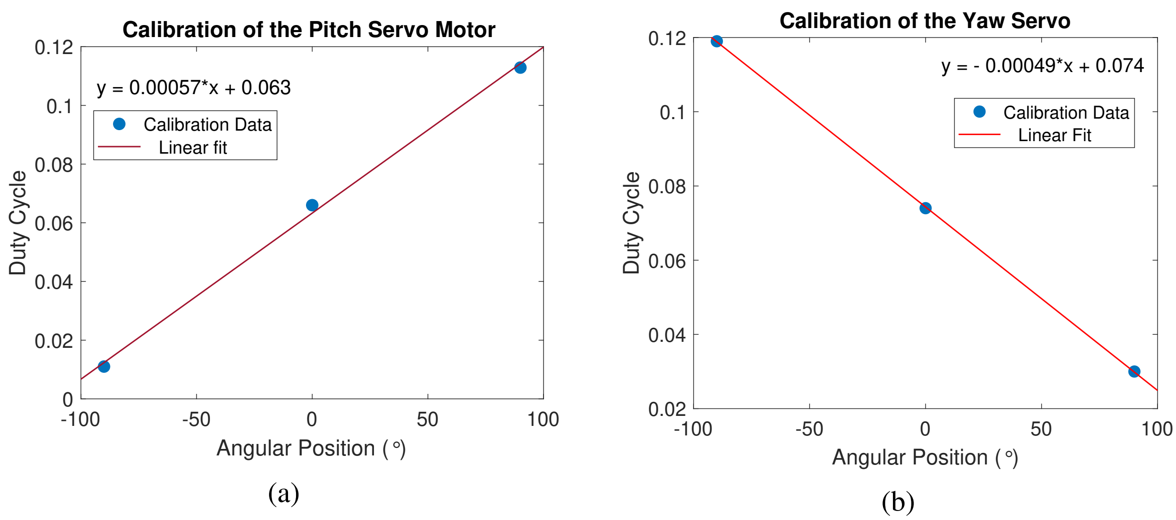

Fig. 3.7: a) Calibration for the Servo Motor for Pitching b) Calibration for the Servo Motor for Pitching

mounted on the first servo motor and allowed for pitching motion of the probe. Both servo motors were connected to the NI-USB 6363 DAQ and were controlled using LabView codes that sent a duty cycle of a Pulse Width Modulation (PWM) signal. Both servo motors were calibrated and a relation between the duty cycle value and angular position of the motors was obtained, which is described in Fig 3.7.

Table 3.2: Specifications of the HiTec HS-85BB Servo Motor

Voltage Range	Pulse Cycle	Pulse Width
4.8V-6.0V	20 ms	900-2100 μs

A mount (see Fig 3.8), which acted as an interface between the hot wire probe and the servo motors, was 3D printed using FormLabs Form2 Stereolithography printer (which has a layer resolution of 0.025 mm) using their proprietary standard black V4 photopolymer resin. The mount had clearance holes for two M2 flat head, hex drive, 5mm long screws to attach with the servo and one clearance hole for an M2 screw to keep the probe in place. The assembly of the entire setup can be seen in Fig 3.9.

Finally, the measurements were made using an Auspex 4 Sensor Vorticity probe with the sen-

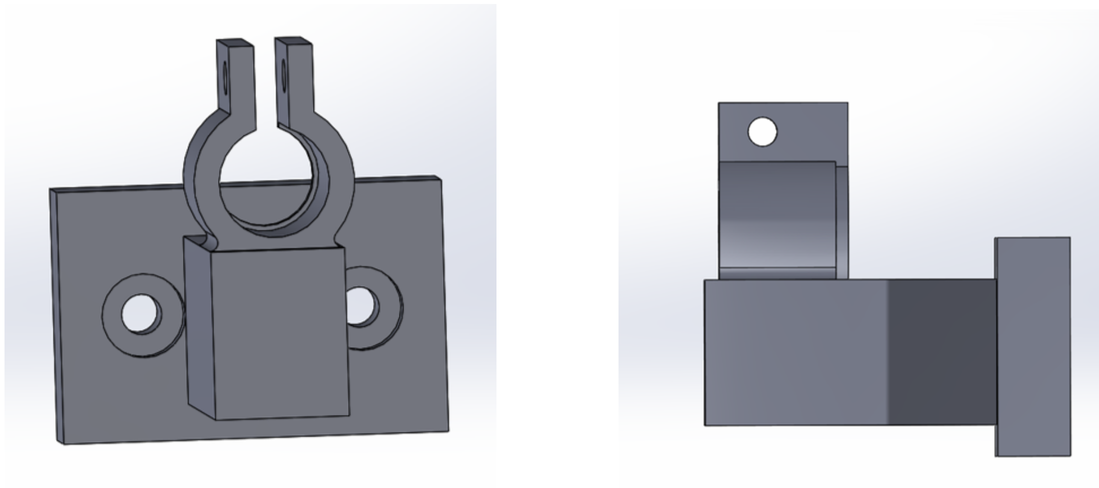

(a) (b)

Fig. 3.8: a) Front view of the mount b) Side view of the mount

sor diameter of 5 microns and sensor length of 1mm; the configuration of the wires is shown in Fig 3.10. The probe body was a round stainless steel tubing with 0.25 inches outer diameter. The four sensors were connected to four of the six channels of the AA Labs AN-1003 Constant Temperature Anemometer (with option 04 for high frequency operation), loaned from the University of Ottawa. The four outputs of the CTA were connected to the NI-USB 6363 DAQ.

3.3 Methodology

3.3.1 Hot-Wire Calibration

Each channel in the CTA was calibrated using the method described in [53]. For each channel, the gain was set to 1, the overheat ratio (OHR) was 1.5, the D.C. Offset was 3V and a low-pass filter of 14 kHz was used. The two pairs of cross wires were calibrated using velocity pitch-map calibration, the method for which is described as follows:

1. Set a pair of cross wires to a given pitch angle
2. Acquire voltages from the two channels over a range of wind speeds (U_b= 5m/s, 7.5m/s, 10m/s, 12.5m/s and 15m/s in our case)

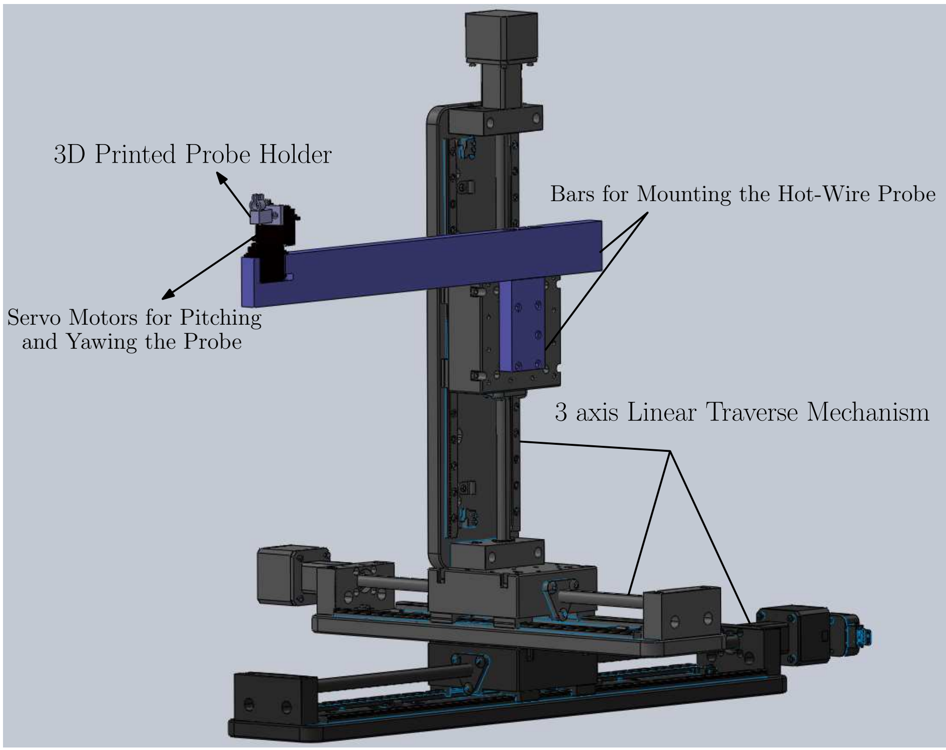

Fig. 3.9: Final Assembly of the setup for Hot-Wire Measurements

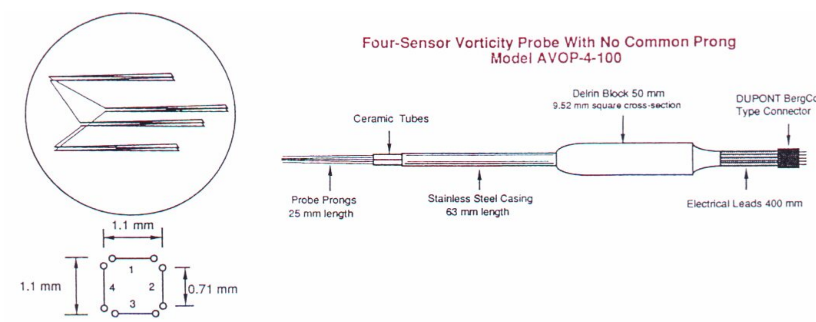

Fig. 3.10: Four Sensor Hot-Wire Probe [52]

3. Repeat the process over a range of pitch angles (θ= -21°, -14°, -7°, 0°, 7°, 14° and 21° in our case; see Fig 3.11)

4. Fit the voltages to a third order surface polynomial to obtain a calibration for voltages for pitch angles and velocities

5. U and V are obtained using $U = U_b cos\theta$ and $V = U_b sin\theta$

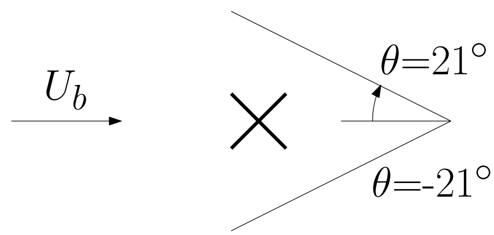

Fig. 3.11: Calibration of a Cross Wire

This process was repeated for the other pair of cross wires in the yaw direction. The two pairs of cross wires were re-calibrated if the change in temperature in the test section was greater than 1°C. An example of the velocity pitch-map calibration can be seen in Fig 3.12.

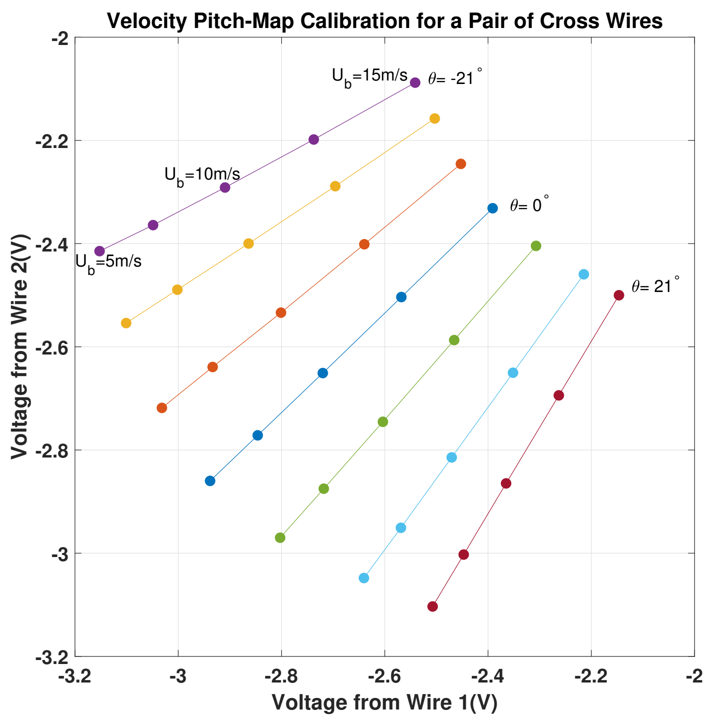

Fig. 3.12: Velocity Pitch-Map Calibration for a Pair of Cross Wires

3.3.2 Background Turbulence

One of the characteristics of a wind tunnel is its background turbulence intensity, which is the ratio of the root mean square of the velocity fluctuations and the free stream velocity *i.e.,* $\frac{u_{rms}}{U_\infty}$, where the velocity fluctuations, u are given by the difference between the instantaneous velocity, U_i and the mean velocity, U. This is known as Reynolds decomposition. The instantaneous velocity is measured in the test section without the model, and the fluctuating component of the velocity is computed. The turbulence intensity gives an idea of how turbulent the oncoming flow is. The contribution to the noise could be electrical (due to stepper and servo motors), mechanical (due to the motion of the linear traverses) or due to unsteadiness in the wind tunnel itself. To measure the background turbulence at the test speed of 10 m/s, the four sensor hot wire probe was placed at half the height of the test section and moved at downstream distances of $\frac{x}{c}$= 0.5, 1, 1.5, 2, 2.5 and 3. The turbulence intensity in the longitudinal *i.e.,* in the direction of x, u was computed by using T_u=$\frac{u_{rms}}{U_\infty}$. Similar measurements were taken for v and w and are shown in Fig 3.13. The largest value of T_u is 1.09%, while T_v and T_w is 0.2% and 0.19% at the farthest downstream position.

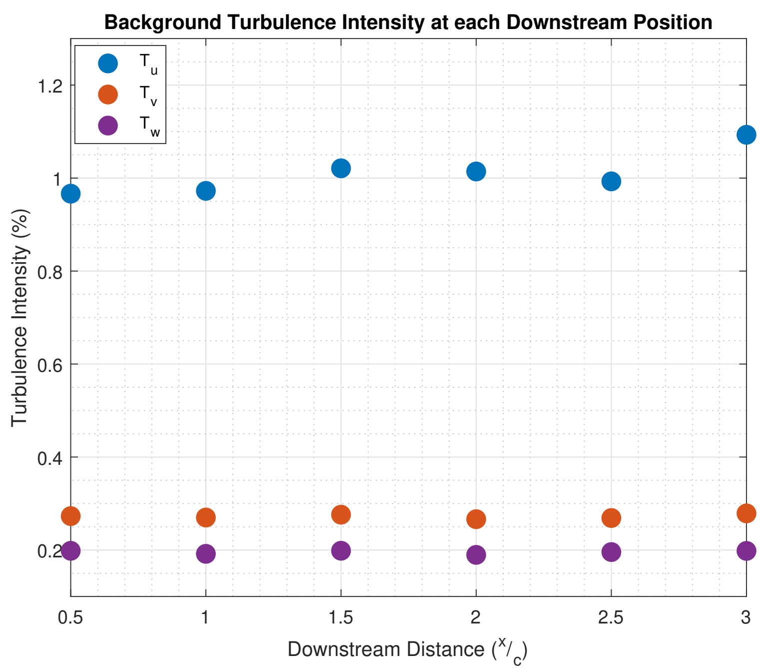

Fig. 3.13: Turbulence Instensity in the Wind Tunnel test section for all three components of velocity; T_u seems to have a maximum value of 1.09%, while T_v and T_w are 0.2% and 0.19% on an average

3.3.3 Grid Capturing the Tip-Vortex

In this section, we discuss how the tip vortex was measured using the hot-wire probe. The three axis traverse system was used to move the hot-wire over a 33mm x 33mm grid in the $y - z$ plane, from z values ranging from -0.1<z/c< 0.23 and y values ranging from -0.26<y/c< 0.07, with 1 mm increments in both directions. This plane of measurement was chosen based on measurements to capture tip-vortices performed by Ahmadi-Baloutaki *et al* [48]. Each test plate was set at a 5° angle of attack (the angle of attack corresponding the the peak $\frac{L}{D}$ ratio), found by force measurements using the ATI Gamma IP68 sensor. The trailing edge of the test plates at an angle of attack of 0° was chosen as the the global origin (0,0,0). Grid measurements were taken at downstream distances (in the x direction) of 0.5c, 1c, 1.5c, 2c, 2.5c and 3c from the trailing edge. Fig 3.14 shows how the vortex was captured using a grid and Fig 3.15 shows an example of the V and W velocities captured through the grid. The measurements were taken at a sample rate of 30 kHz for 30 seconds using the NI-USB 6363 DAQ. The sample rate was chosen to be 30 kHz because the low-pass filter on the CTA was set at 14 kHz; according to the Nyquist theorem, to avoid aliasing, the sampling frequency should be more than twice the frequency of the highest frequency that we hope to capture. Data was acquired for 30 seconds as that was the amount of time required for the mean values of the signals to converge.

3.3.4 Mean Velocity Profile Measurements

Section 3.1.1 described the structure of a tip-vortex; if a hot-wire probe is moved from the center of the tip-vortex along the y axis (see Fig 3.1), the V component of velocity would be zero and the tangential velocity would be equal to W (as θ becomes 0). Assuming that the vortex is axisymmetric, this velocity profile can characterize the tip vortex by measuring the core radius and the peak tangential velocity. To measure this velocity profile, the center of the vortex has to be found using the grid described in the previous section. The center of the tip vortex is defined as the point at which both- the V and W components of velocity are 0 [48]- and was found using the point of intersection of the contours where V and W are 0. Fig 3.16 shows the V and W velocity contours for one measurement plane and the corresponding point where the zero contours of V and W intersect. The hot-wire probe was moved to this point and then moved in the y direction in 1 mm increments to measure the tangential velocity profile of the tip vortex. At each point

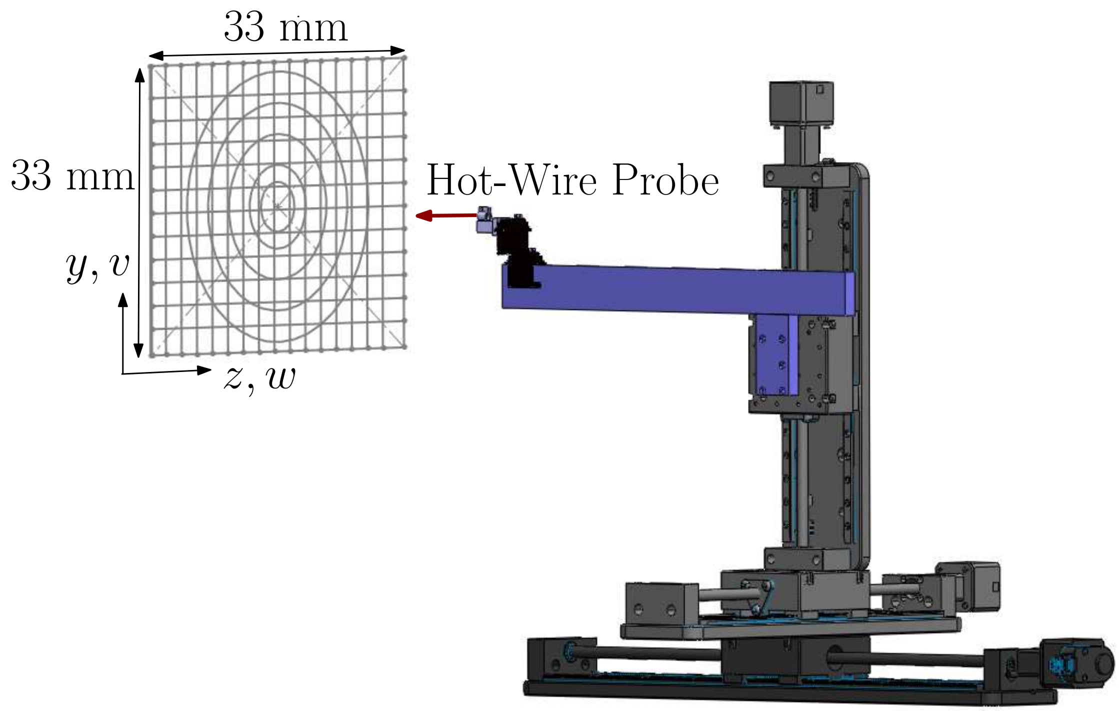

Fig. 3.14: Three Axis Traversing Mechanism Capturing the Tip-Vortex through a 33 mm×33 mm Grid

in the y direction, data was acquired at a sample rate of 30 kHz for 60 seconds, this increase in sampling time was set to decrease statistical uncertainty in the measurements.

Finally, to check for vortex wandering, the hot wire probe was moved to the center of the vortex and data was acquired at the center at a sample rate of 30 kHz for 600 seconds. A long data sample was necessary because sample time is inversely proportional to the lowest frequency that we can measure in the flow, and vortex wandering is a low frequency motion of the vortex center.

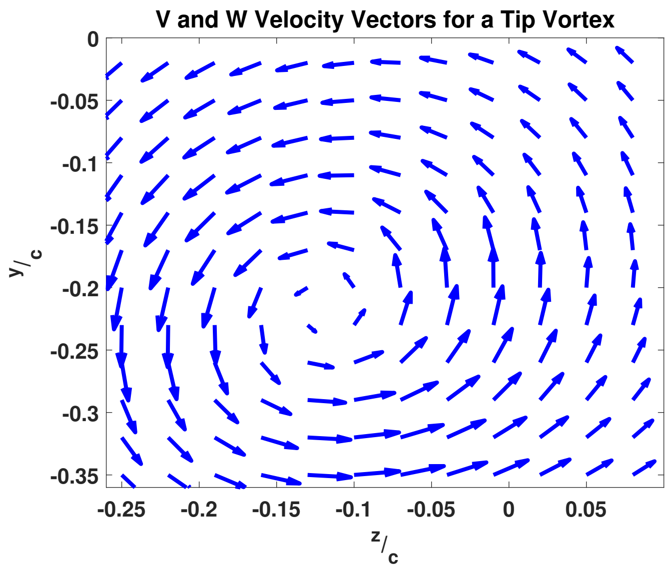

Fig. 3.15: V and W components of velocity of a tip vortex at $\frac{x}{c}$=1 for a flat plate

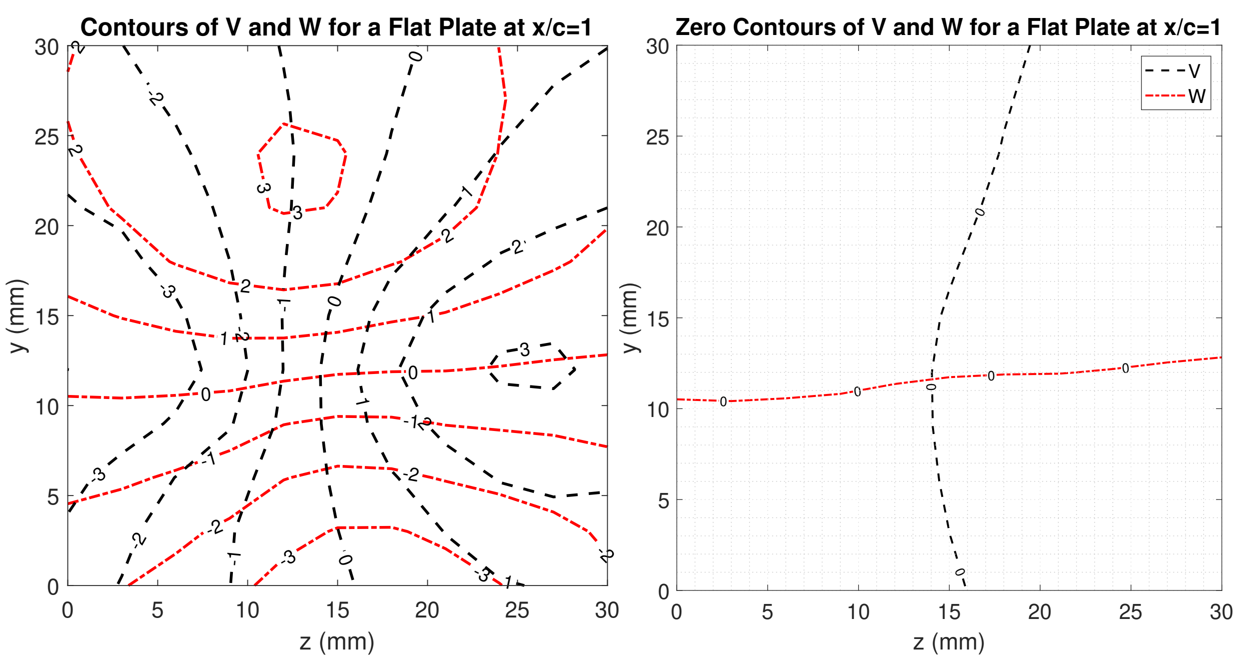

(a) (b)

Fig. 3.16: Contour plots of the V and W components of velocities measured for a flat plate at 1c

3.4 Position of the Tip Vortex

The position of the tip vortex affects the aerodynamic forces and moments acting on a lifting surface by influencing the downwash speed, which results in a change in the downwash angle (depicted in Fig 3.17). If the tip vortex lifts up, *i.e.,* move in the direction of the lift, the downwash speed becomes smaller (as the distance between the tip vortex and the wing is larger), leading to a decrease in the induced angle, α_i. A lower α_i leads to a smaller lift induced drag according to Eq 1.2. The position of the vortex center also affects the overall pressure distribution over the lifting surface, thereby changing the position of the Center of Pressure, which is the point where the total lift and drag act on a wing surface. This change in the center of pressure leads to a change in the pitching, rolling and yawing moments, as explained in Section 2.3.2.

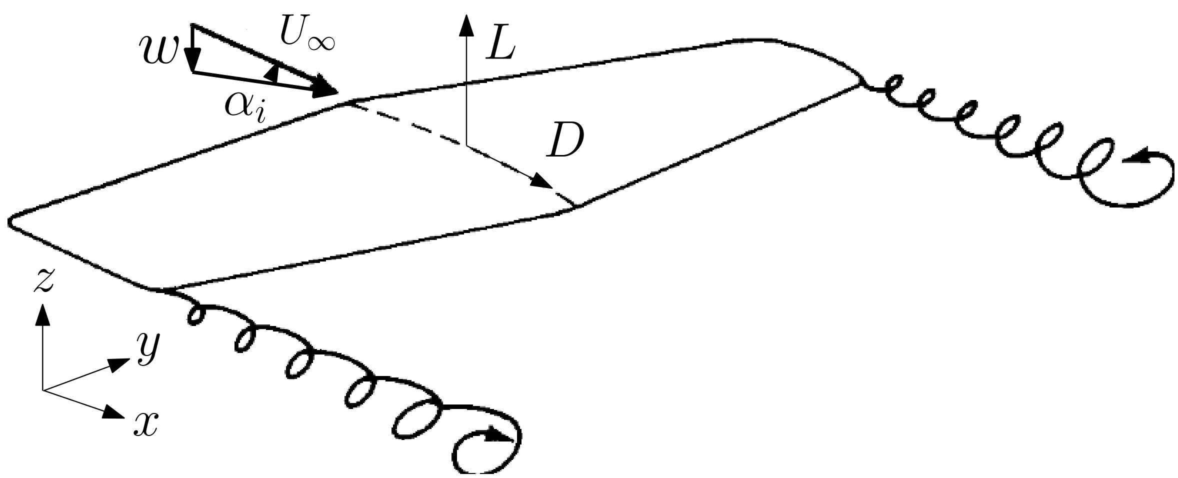

Fig. 3.17: Figure depicting the effect of the position of the vortex on a lifting surface (adapted from [4]); the position of the vortex affects the downwash speed, leading to a change in the downwash angle

The center of the tip vortex was found using the method described in Section 3.3.3. The tip vortex measured for the flat plate at different downstream locations is shown in Fig 3.18. Note that the trailing edge of the flat plate at a 0° angle of attack is fixed as the origin.

Fig 3.19 shows the position of the center of the tip vortex in the z direction (*i.e.,* in the direction of the lift force), while Fig 3.20 shows the position of the vortex center in the y direction, with respect to the origin for each test plate. The presence of the chevron plates moves the

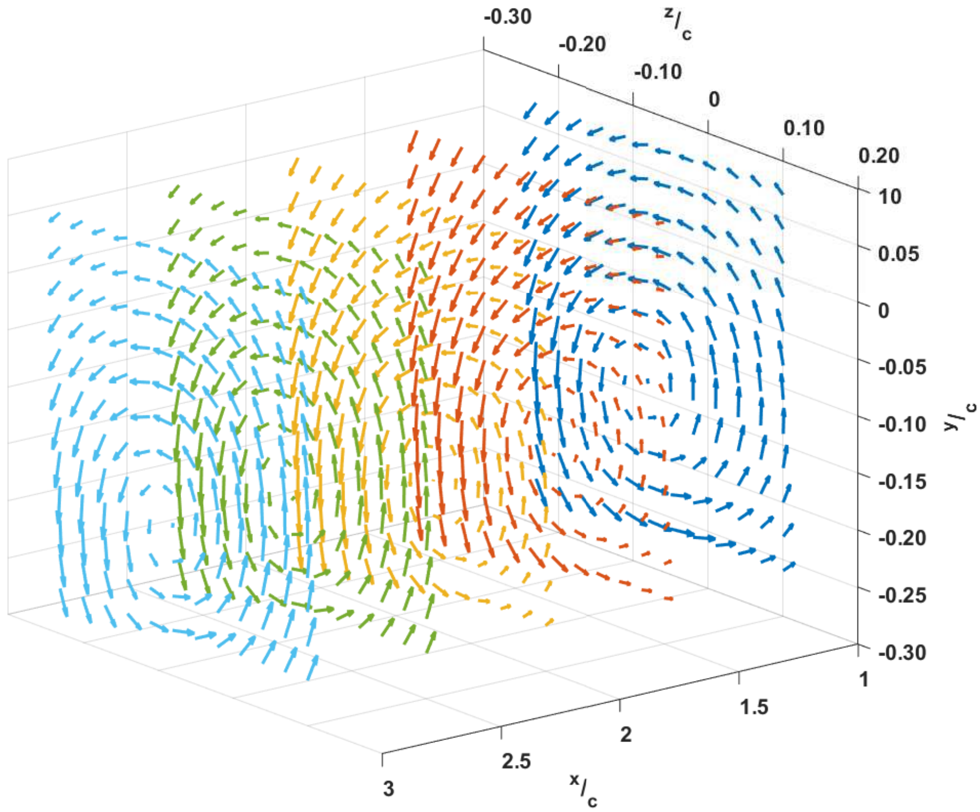

Fig. 3.18: V and W components of velocities at each downstream position for a flat plate, depicting the change in the position of the vortex center

tip vortex towards the wing root and in the direction of lift. In general, as the chevron depth increases, the vortex center moves further in the z direction- the 10mm and 20mm chevron plates have vortex centers ($\frac{z}{c}$) between 0.1c and 0.15c from the origin, while the 40mm and 50mm chevron plates have vortex center at roughly 0.15c from the origin. The vortex center of the 30mm chevron plate lies between 0.09c and 0.15c. All the chevron plates have $\frac{z}{c}$ values of vortex centers that are greater than those of the flat plate. The 'lifting' of the vortex center leads to a smaller induced drag due to a smaller downwash angle. It is also observed that the chevron plates have vortex centers that are pushed towards the root of the wing, as compared to the flat plate. Again, as the chevron depth increases, the vortex centers are shifted towards the root of the wing. This would affect the pressure distribution over the test plates, that could lead to a change in the Center of Pressure, and therefore, the moment arm. A change in the pressure distribution

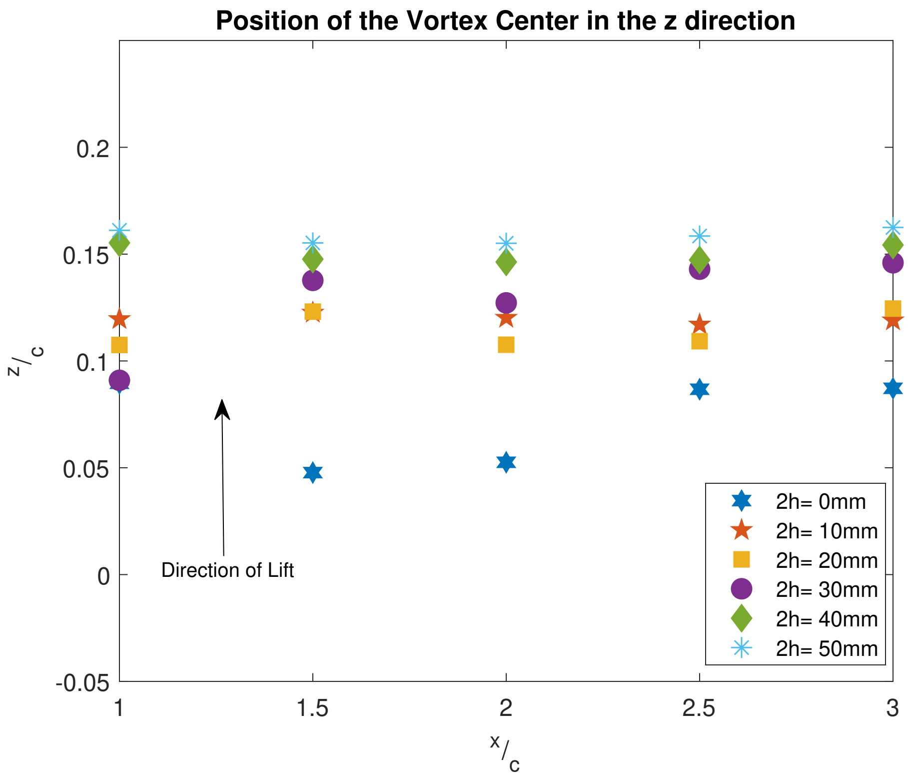

Fig. 3.19: Normalized z coordinates of the vortex center for each test plate

could also explain the observed difference in profile drag in the test plates. The exact pressure distribution over the test plates, however, would have to be studied using pressure taps on the wing surface. We could also speculate that the movement of the vortex centers towards the wing root would lead to tip vortex pairs in an aircraft wing or drone to move closer to each other, leading to faster mutual interaction and dissipation [10]. The following section looks at the tip vortex itself in more detail.

3.5 Size and Strength of the Tip Vortex

Fig 3.21 shows the contours of the U, V and W components of velocities, measured across a 33mm $\times$ 33mm grid. One can clearly see that the tip vortex is axisymteric and therefore, measuring the velocities along the y axis would sufficiently characterize the tangential velocity and the core radius. The tangential velocities were measured at six downstream positions (x=

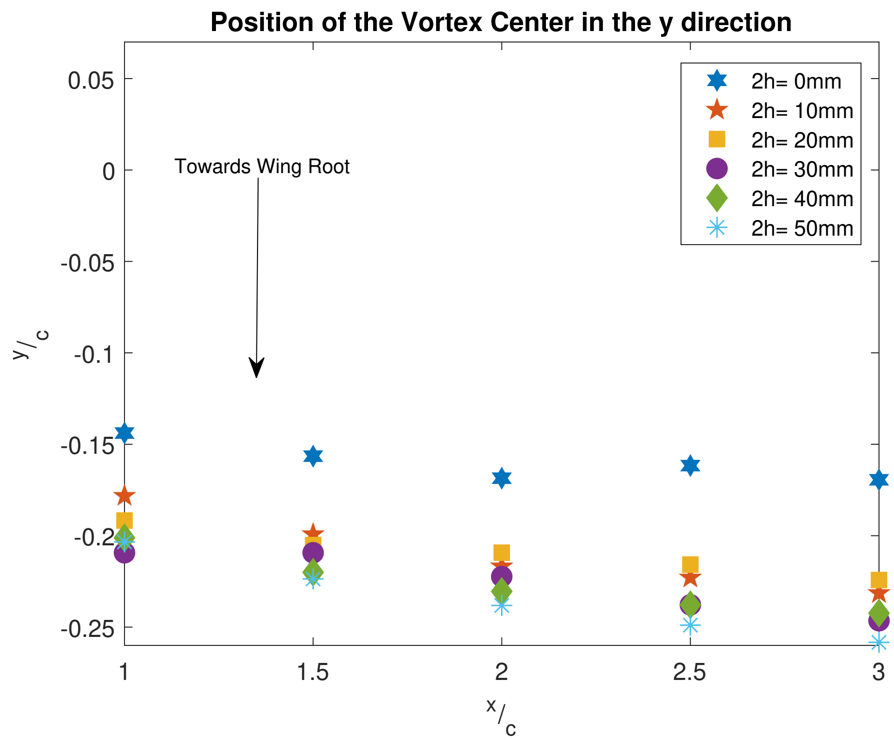

Fig. 3.20: Normalized y coordinates of the vortex center for each test plate

0.5c, 1c, 1.5c, 2c, 2.5c and 3c) for each of the test plates. At $\frac{x}{c}$= 0.5, the tangential velocities for each flat plate showed peaks at two radii for each test plate, which is shown in Fig 3.24. This indicates a double core structure of the tip vortex, consistent with Devenport *et al.*'s observation. They observed the presence of a double core that disappeared with an increase in streamwise distance and attributed it to the initial conditions, based on Engel *et al.* [54]'s study of the tip vortex on a NACA 0012 wing. Using helium bubble flow visualization, they found the presence of a primary vortex at half chord on the suction side of the NACA 0012 wing alongwith a corotating secondary vortex that merged with the primary vortex at about 1c. As a result of this double core structure in the tip vortex at 0.5c, the majority of this study focuses on downstream distances of 1c to 3c.

The strength of a vortex can be characterized by its circulation, Γ, which is given by the line integral around a closed curve of the velocity field, or $\oint_C V\,dl$. A large core radius and small peak tangential velocity indicate lower circulation and therefore, a weaker vortex. Fig 3.22 shows the tangential velocities for a flat plate at all five downstream positions, while Fig 3.23

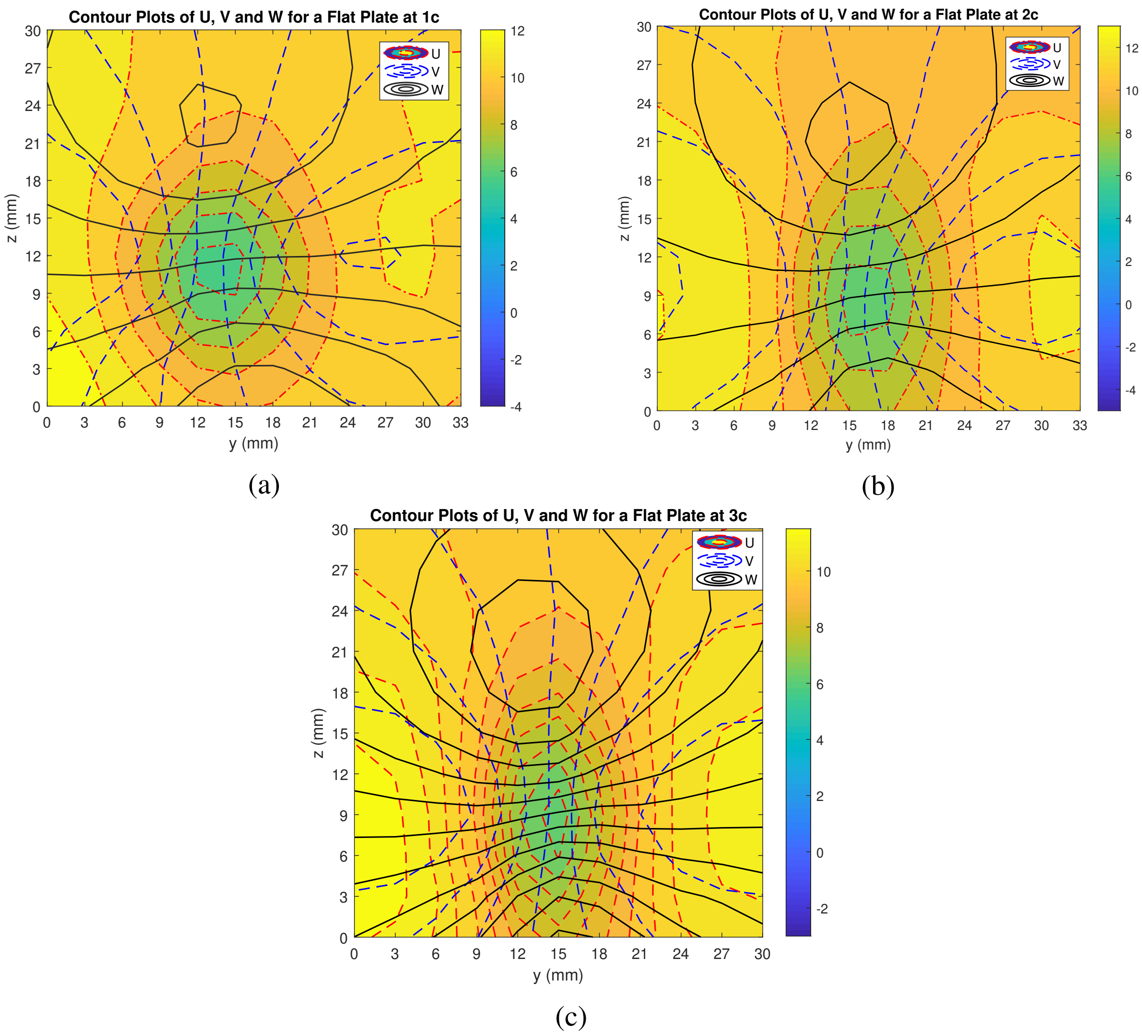

Fig. 3.21: Contour plots of the U, V and W components of velocities measured for a flat plate at a) 1c, b) 2c and c) 3c

shows the tangential velocities for the test plates at $\frac{x}{c}$= 1. To compare the strength of the tip vortex for each chevron plate at each downstream position, we focus our attention on the peak tangential velocity and the corresponding core radius. This comparison is only possible if the general tangential velocity profile of the tip vortex of each test plate is the same. This was ascertained by normalizing the tangential velocity with the peak tangential velocity and radial distance with the core radius for each plate at each downstream position, as the flow in the core of the tip vortex has been shown to be self similar, with the tangential velocities normalized by the peak tangential velocity and radial distances normalized by the core radius, for a fully developed tip vortex. The normalized tangential velocities are expected to follow the curve given by Eq 3.12 up to $\frac{r}{r_c} < 1.2$ [55].

$$\frac{U_\theta}{U_{\theta_{max}}} = \frac{1}{0.716(\frac{r}{r_c})}\left(1 - exp\left(- 1.2526 \left(\frac{r}{r_c}\right)^2\right)\right) \tag{3.12}$$

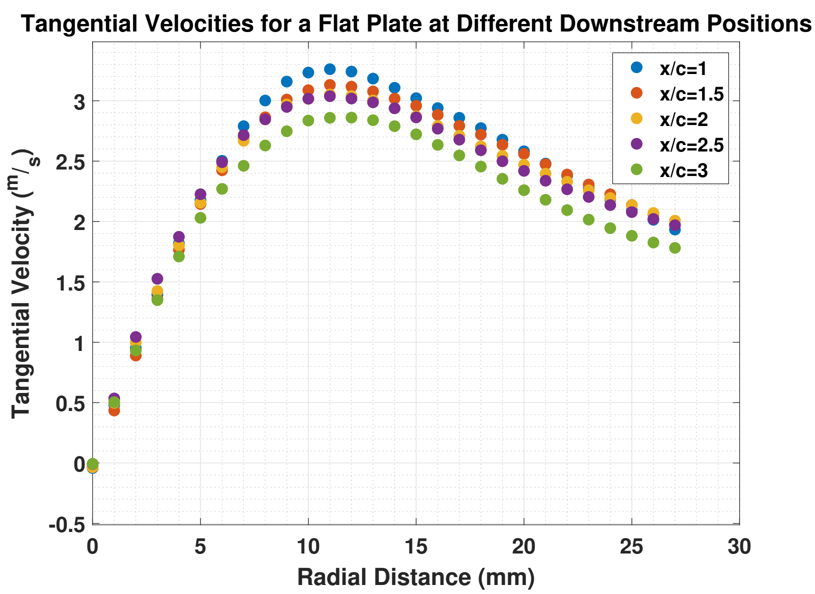

Fig. 3.22: Tangential Velocity Profiles at Different Downstream Positions for a Flat Plate

Fig 3.25 shows the normalized tangential velocity profiles for the flat plate at each downstream position, while Fig 3.26 shows the same for all the test plates at 3c. One can see from both figures that the core of the tip vortex for each plate is self-similar up to roughly $1.2r_c$ and closely follows the analytical solution given by Eq 3.12, after which the normalized tangential velocities deviate significantly from the analytical solution. Note that this solution and the assumption of

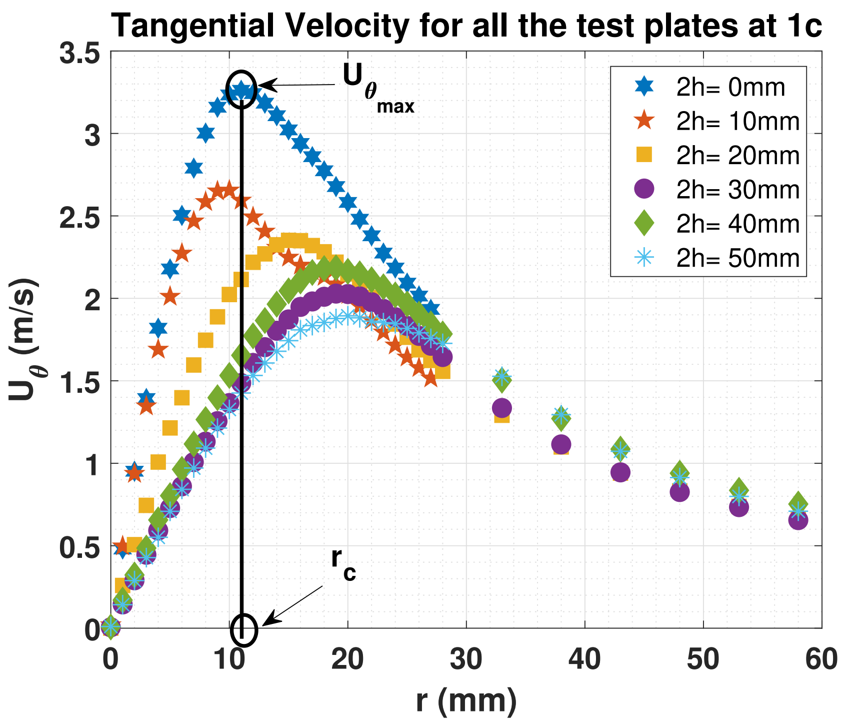

Fig. 3.23: Tangential Velocity Profiles for all Test Plates at $\frac{x}{c}$=1

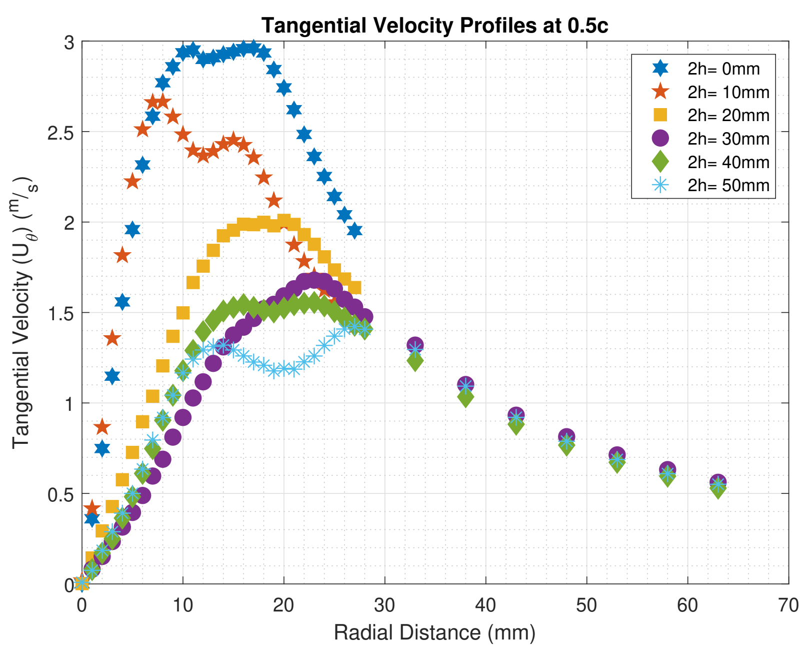

Fig. 3.24: Tangential Velocity Profiles for all Test Plates at $\frac{x}{c}$=0.5, showing a double core structure for each test plate

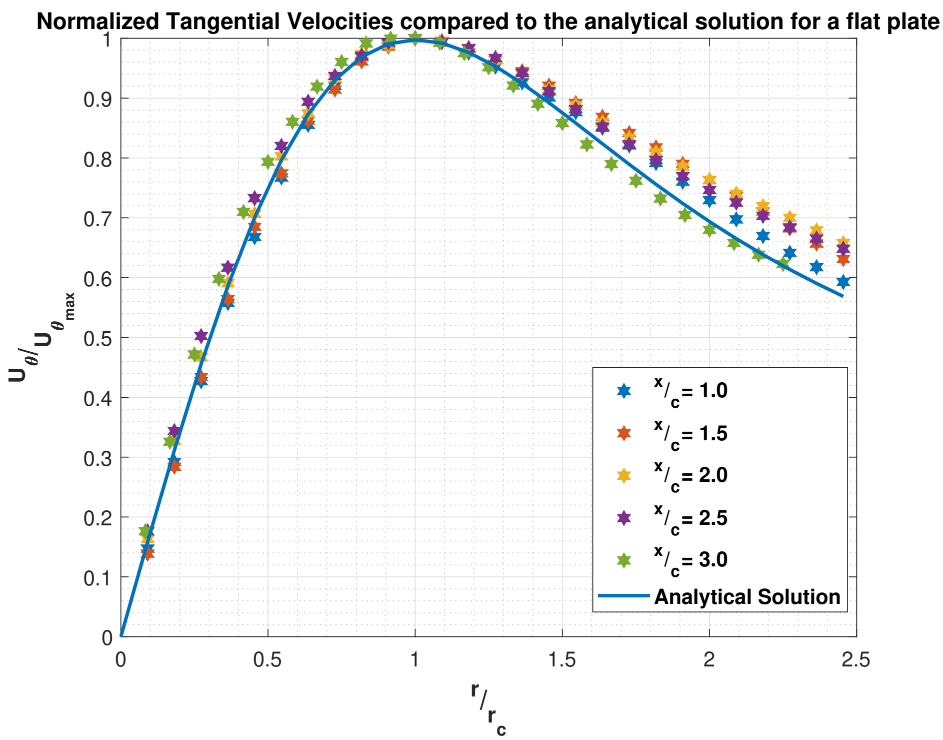

Fig. 3.25: Normalized Tangential Velocity Profiles of the Flat plate at each downstream position compared to the analytical solution

self similarity is only valid if the vortex is fully formed, which may or may not be the case for the measurements presented in this thesis at downstream distances of 1< $\frac{x}{c}$ < 3. More analysis on this is presented in Section 3.6.1. However, for the following analysis, it is suffice to keep in mind that the general profile of the tangential velocities is the same for every test plate, and therefore, the peak tangential velocity and corresponding core radius would adequately characterize the tip vortex and allow a meaningful comparison between the different test plates.

Fig 3.27 shows the peak tangential velocities at each downstream position for all the flat plates. One can see that the peak tangential velocities for the chevron plates are significantly lower than the flat plate at each downstream location. This observation could corroborate our initial hypothesis: the presence of chevrons could lead to the formation of several smaller tip vortices that would interact with each other and result in a tip vortex that is weaker. In order to validate this, detailed planar velocity measurements would have to be taken, using particle image velocity for example; this is, however, beyond the scope of the current thesis. There is a clear pattern between the chevron depth and the tangential velocity- deeper chevrons lead to smaller

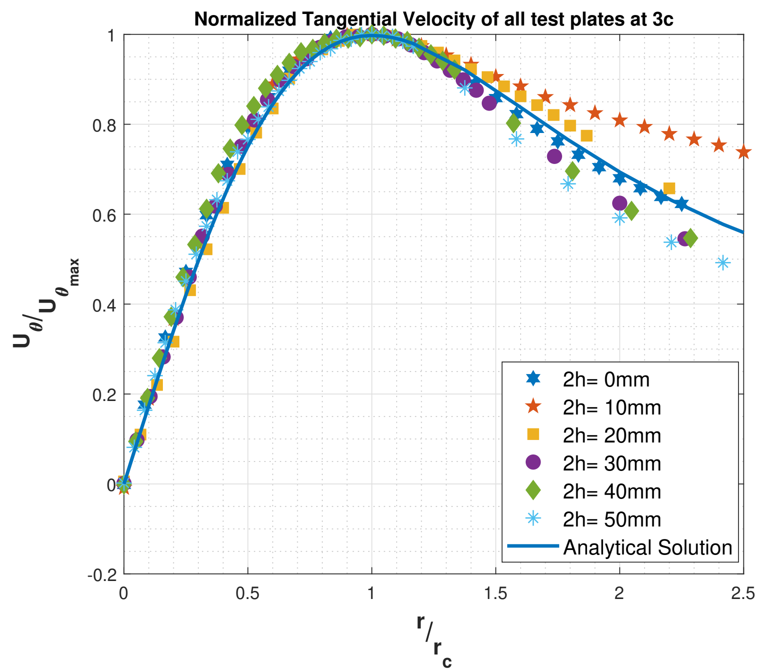

Fig. 3.26: Normalized Tangential Velocity Profiles of every test plate at 3c compared to the analytical solution

peak velocities. It is also of interest to compare the rate at which the peak tangential velocities decrease with an increase in downstream distance, as it gives a better picture of whether or not the presence of chevrons leads to tip-vortices that dissipate faster. To compute this, we performed a power law fit of the form $\frac{U_{\theta max}}{U_\infty} \propto \left(\frac{x}{c}\right)^{-n}$ to the peak tangential velocities at five downstream positions of each plate. Table 3.3 shows the 'decay rate' for each chevron plate and the percentage change in decay rates as compared to the flat plate. All the chevron plates, barring the 40mm plate, have a higher decay rate than the flat plate. It is to be noted here that these power fits were performed for peak velocities at $1 < \frac{x}{c} < 3$, which is merely five data points. An issue with power law fits is that their uncertainty decreases as the spatial range over which they are applied

Table 3.3: Decay Rate of the Tip Vortex for all the Test Plates

Test Plate	0 mm	10 mm	20 mm	30 mm	40 mm	50 mm
Decay Rate (n)	0.1038	0.1896	0.1310	0.2284	0.08541	0.2148
% change in decay rate	0	+82.7	+26.2	+120.0	-17.7	+106.9

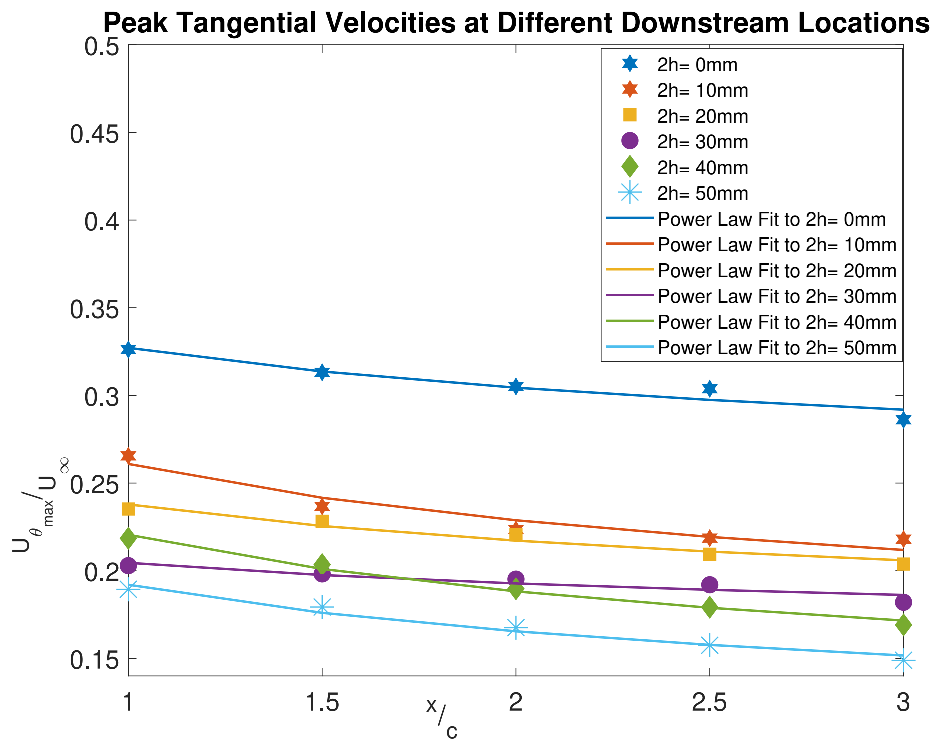

Fig. 3.27: Peak Tangential Velocities Normalized by the Free Stream Velocity (U_∞) for Test Plates with the corresponding power law fits at $\frac{x}{c}$= 1, 1.5, 2, 2.5 and 3

increases. Therefore, an alternative way to look at whether or not the peak tangential velocities are decaying faster is to look at their normalized 'decay rate', by normalizing the peak tangential velocity at each downstream position with the value of $U_{\theta_{max}}$ at $1c$. This is shown in Fig 3.28. One can see that the peak tangential velocities of the 10mm, 40mm and 50mm chevron plates decrease significantly faster than the flat plate. The 20mm plate seems to have a decrease in the normalized peak tangential velocity which is comparable to the flat plate and the 30mm chevron plate seems to have a lower decay rate than the flat plate. This is contrary to the results given by the power law fit, that indicate a faster decay rate for the 30mm chevron plate and a lower decay rate for the 40mm plate, as compared to the flat plate.

The core radius is an important parameter to compare the effect of the chevrons, as it indicates the size as well as the strength of the vortex. Fig 3.29 shows the core radius (r_c) of the tip vortices for the test plates at every downstream location. The chevron plates have a larger vortex core as compared to the flat plate, barring the 10mm chevron plate, which has a smaller vortex core. For the 30mm, 40mm and 50mm chevron plates, the core radius increased with an increase in the

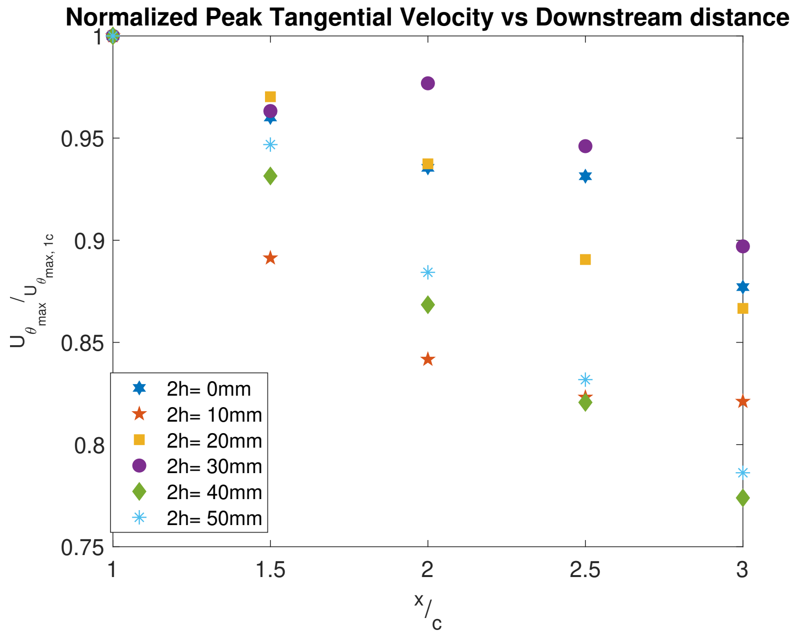

Fig. 3.28: Peak Tangential Velocities Normalized by the Peak Tangential velocity at $\frac{x}{c}$= 1, with an increase in downstream distance

streamwise distance. This implies that the tip vortex is weaker i.e., it has a low peak tangential velocity and large core radius as compared to a flat plate.

At this point, it is important to ensure that these lower peak tangential velocities and higher core radii exhibited by plates with chevron wing tips are due to the presence of the chevron tips and not due to wandering. It has been shown by Bailey *et al.* [56], who studied the effect of wandering on a tip vortex in grid generated turbulence, that wandering can lead to a rapid decrease in the peak tangential velocities and increase in the core radius. To check whether or not the tip vortex was wandering, 10 minute long measurements of u, v and w were taken at the center of the tip vortex, as described in Section 3.3.4 and the power spectral density was computed.

The autocovariance $R(s)$ is a multi-time statistic that is given by $\overline{u(t)u(t+s)}$ and gives the correlation coefficient of a quantity (say, velocity) between time t and $t+s$ at a single point. The autocovariance forms a Fourier transform pair with twice the power spectral density, $E_{ij}(f)$, which is given by $\frac{1}{\pi}\int_{-\infty}^{\infty} R_{ij}(s)e^{-ifs}ds$. Therefore, $R(s)$ will be equal to $\int_{\infty}^{\infty} E_{ij}(s)e^{ifs}df$. If i=j and s=0, one can see that $\overline{u_{ii}}^2$=$\int_{\infty}^{\infty} E_{ii}(f)df$. Therefore, an integral of the power spectral density over a bandwidth of frequencies would give the turbulent kinetic energy within that bandwidth.

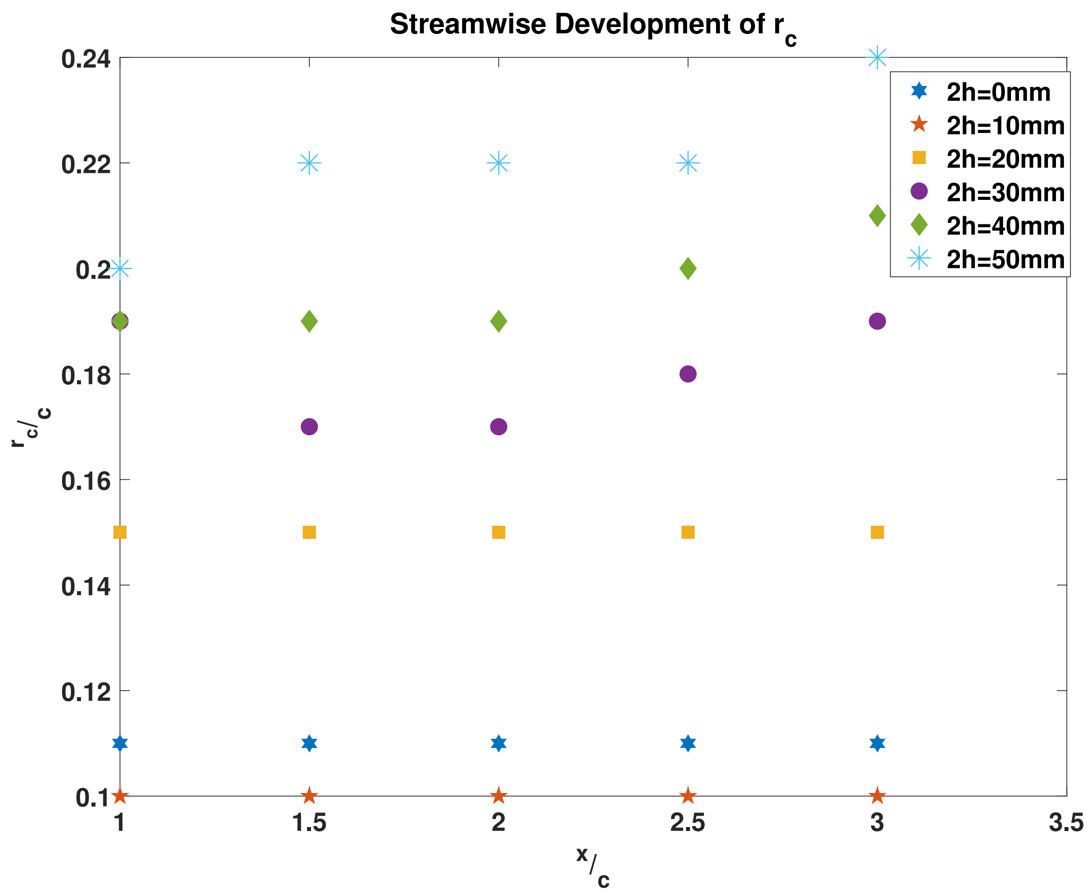

Fig. 3.29: Core Radii Normalized by the chord length (=100mm) for Test Plates at $\frac{x}{c}$= 1, 1.5, 2, 2.5 and 3

E_{ii} plotted against frequency gives a temporal description of contribution to energy by all the possible sources of energy in the flow field. According to Kolmogorov's first hypothesis, at sufficiently high Reynolds numbers, the statistics of the smaller scales have a universal form, uniquely determined by the dissipation rate of the turbulent kinetic energy (ϵ) and the viscosity (ν). This range of scales is called the universal equilibrium range. According to Kolmogorov's second similarity hypothesis [57], at high Reynolds numbers and length scales larger than those of the equilibrium range, but still smaller than the integral length scale (which is the largest scale in the flow), the statistics of motion are going to be determined by ϵ alone and are independent of ν. This range of scales is called the inertial sub-range. Kolmogorov used dimensional analysis for theoretically deriving the shape of the spectrum in the inertial sub-range and found that the slope of the spectrum is equal to $\frac{-5}{3}$. A more rigorous explanation of the same can be found in

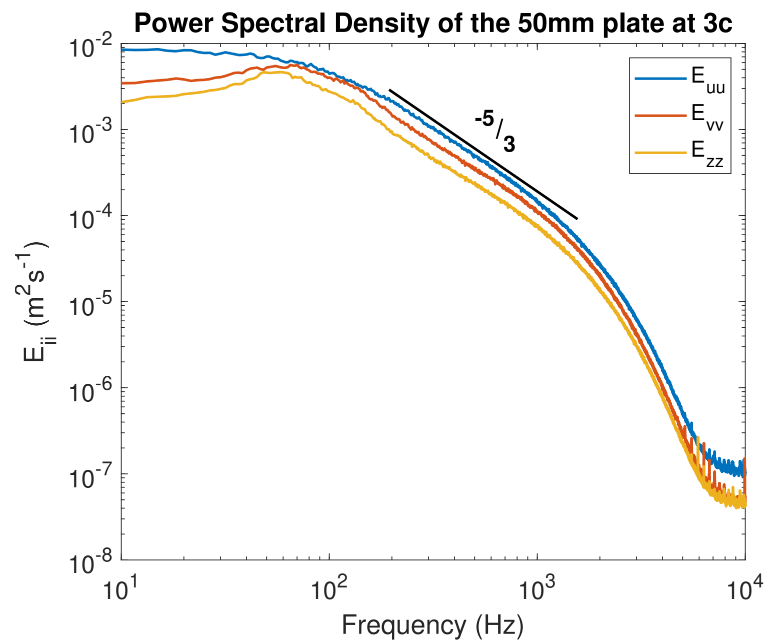

Fig. 3.30: Power Spectral Density (E_{ii}) of u, v and w at the vortex center of the 50mm chevron plate at 3c, showing a slope of $^{-5}/_{3}$, thereby indicating turbulence in the core

textbooks on turbulence by Tennekes and Lumley [58] and Pope [57]. As an example, consider the power spectral density of u, v and w at the vortex center of the 50mm deep chevron at 3c, shown in Fig 3.30, which has a slope of $\frac{-5}{3}$, from which it can be inferred that the flow at the core is turbulent.

To study whether or not the vortex was wandering, the cross power spectral density coefficient ($\frac{E_{yz}^2}{E_{yy}E_{zz}}$) of v and w was plotted at 3c , since wandering is a planar motion that affects both components of velocities simultaneously [56]. The farthest downstream location (3c) was chosen, because wandering is shown to increase in amplitude with an increase in streamwise distance [3]. Fig 3.31 shows the cross power spectral density coefficient of the test plates at 3c. The flat plate shows spikes in the cross power spectral density coefficient over a wide band of frequencies. The 10mm chevron plate shows a broadband peak at 10Hz, a narrower and sharper peak at 100Hz and a final slightly broader peak at 300Hz. Using the definition of Strouhal number (St= $\frac{fL}{U_\infty}$), and substituting U_∞ = 10 m/s, f = 300 Hz and assuming the Strouhal number, St to be 0.2, we find that the characteristic length L = 6.6 mm. The thickness of the test plates is 6 mm, therefore, indicating that the spike in frequency at 300 Hz could be due to vortex shedding. The 20mm, 30mm, 40mm and 50mm chevron plates show a clear spike between 50Hz and 70Hz. Bailey

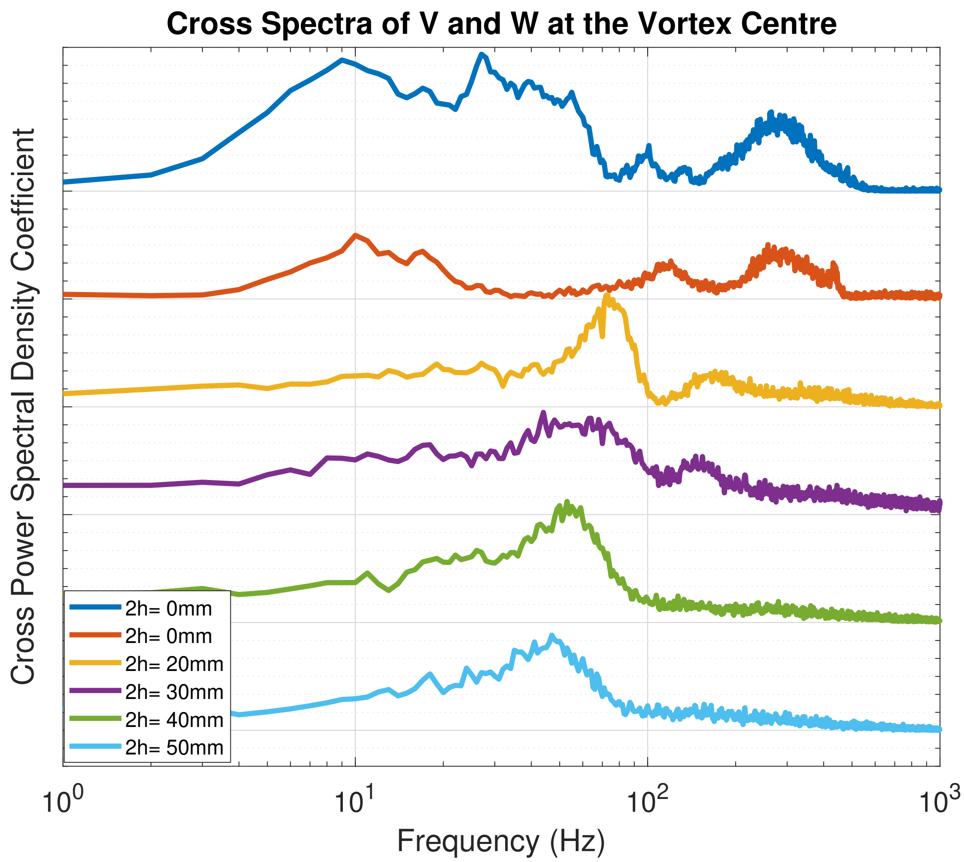

Fig. 3.31: Cross Spectral Power Density Coefficient of the test plates at 3c

et al. [56] identified these spikes in the cross spectra at frequencies below 100Hz as wandering. Therefore, there was a need to correct the mean velocity profiles for vortex wandering.

3.6 Correction of the Tangential Velocity Profiles

In section 3.1.2, we had discussed Devenport *et al.*'s [3] iterative method for correcting the tangential velocity profiles measured by a hot wire probe to account for wandering of the tip vortex. This correction was implemented on our measurements for the flat plate, the 10mm and 20 mm chevron plates by choosing the number of terms in each series (n) in Eq3.3 as half the number of measured points. Fig 3.32 shows the tangential velocity profile measured for the flat plate at 1c and its corresponding correction. Convergence was achieved within four iterations for

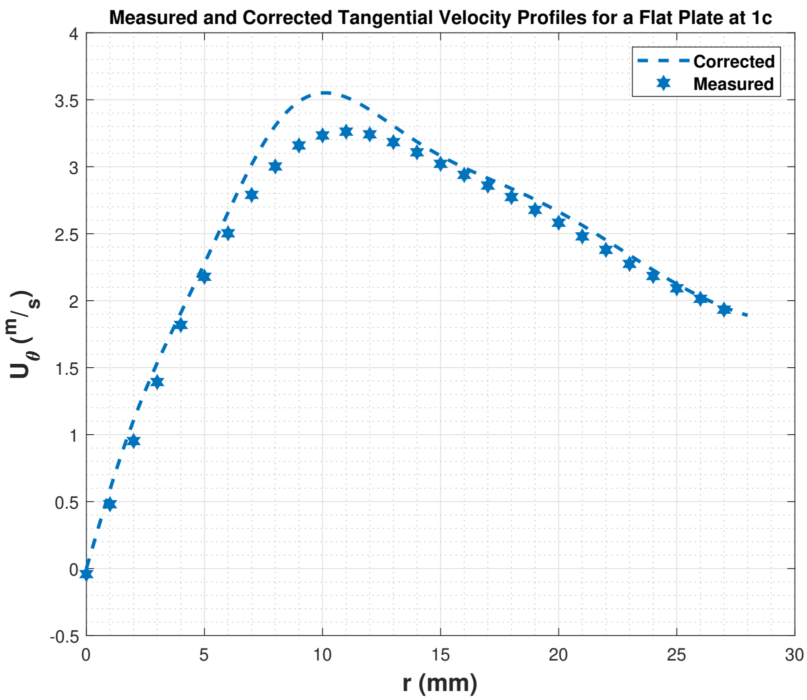

Fig. 3.32: Measured and Corrected Tangential Velocity Profiles for a Flat Plate at 1c

this case and Fig 3.33 shows the maximum difference between the measured and the corrected profiles at each iteration. The corrected and uncorrected (measured) peak tangential velocities normalized by the free stream velocity and core radii normalized by the chord length are shown in Fig 3.34 and Fig 3.35, respectively. It is evident that wandering has an effect on the values of the peak tangential velocities and the core radius size: the corrected peak tangential velocities are higher and the core radii are smaller as compared to the uncorrected values. Based on these corrected profiles, the decay rate was calculated again and is shown in Table 3.4. Despite the correction for wandering, the peak tangential velocities of the chevron plates are significantly lower than the flat plate at each downstream position. The corrected core radii of the 10mm chevron plate are smaller and 20mm chevron plate are larger than the corrected radii of the flat plate, which was also the case for the uncorrected data. While there is a difference in the absolute values of the peak tangential velocities and the core radii of the corrected and uncorrected data, from the onset, the objective of this study was to compare the effect of chevron wing tips on the tip vortex to that of the flat plate. Therefore, in a comparative sense, the results remain unchanged: the presence of chevrons decreases the peak tangential velocity and increases the size of the vortex core in a tip vortex.

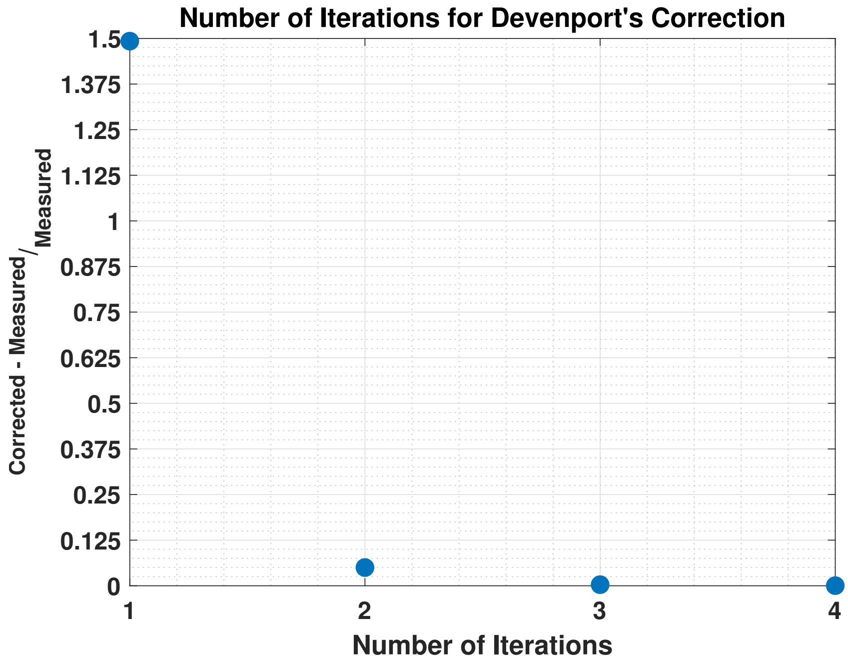

Fig. 3.33: Maximum relative difference between the corrected and measured values of σ_y, σ_z, $\overline{v^2}$, $\overline{w^2}$ and $\overline{vw}$ at each iteration for the correction applied to a Flat Plate at 1c

Another important factor to consider is the accuracy of the correction method itself. These corrections have not found to be very accurate if $\frac{\sigma_{y,z}}{r_c}$ is greater than 60% [59]. Fig 3.36 shows the wandering amplitudes ($\sigma_{y,z}$) normalized by the core radius (r_c) at each downstream location. The wandering amplitudes are higher in the chevron plates as compared to the flat plate, but remain well within the 60% limit and can be relied upon.

This correction could not be implemented on the 30mm, 40mm and 50mm deep chevron plates as the the error did not converge to a point below the tolerance of 0.1%. If the tolerance was increased to 1%, the resulting velocity profiles were oscillatory and the minimum c_i values were greater than the core radius (r_c). Fig 3.37 shows one such case. This can be attributed to

Table 3.4: Corrected Decay Rate of the Tip Vortex for the 0mm, 10mm and 20mm chevron plates

Test Plate	$2h$=0 mm	$2h$=10 mm	$2h$=20 mm
Decay Rate (n)	0.1409	0.2394	0.1152
% change in decay rate	0	+69.9	-18.2

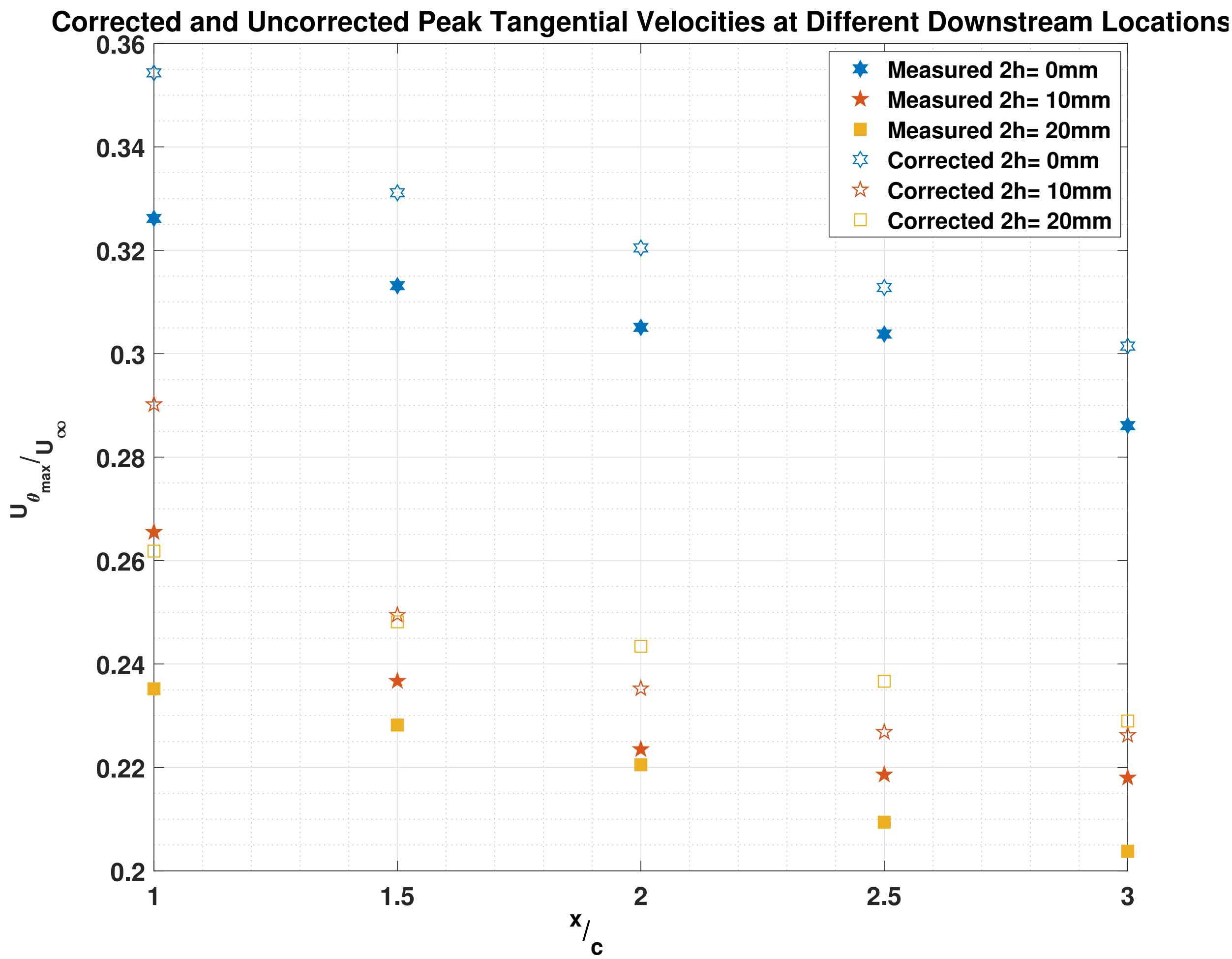

Fig. 3.34: Corrected and Uncorrected Peak Tangential Velocities for the 0mm, 10mm and 20mm chevron plates

the fact that the correction is only valid if the core of the tip vortex is laminar. Bailey *et al.* [56] noted that Devenport *et al.*'s correction did not apply well in the case of high turbulence and became increasingly sensitive to the number of terms (n) in the series fit: smaller values of n lead to poor fits and larger values provided oscillatory velocity profiles. They also noted that a large wandering amplitude iterated to a large minimum value of c_i which exceeded the core radius r_c, leading to an incorrect determination of the location of the peak tangential velocity. Finally, they observed that a small scatter in the measured velocity profiles lead to a large oscillation in the corrected profile. Since we observed this in our implementation of the correction to the velocity profiles of the 30mm, 40mm and 50mm chevron plates, it became important to compute

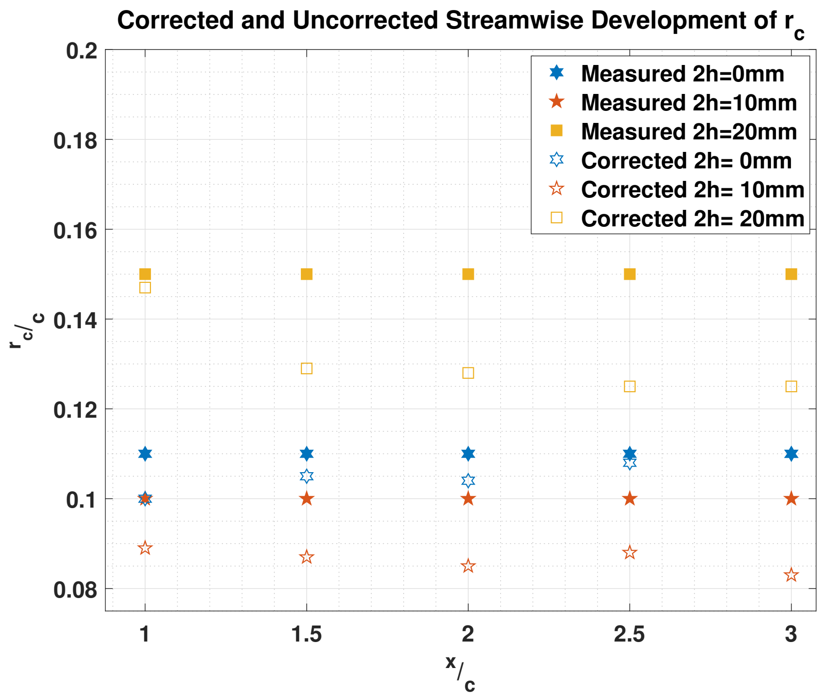

Fig. 3.35: Corrected and Uncorrected Core Radii for the 0mm, 10mm and 20mm chevron plates

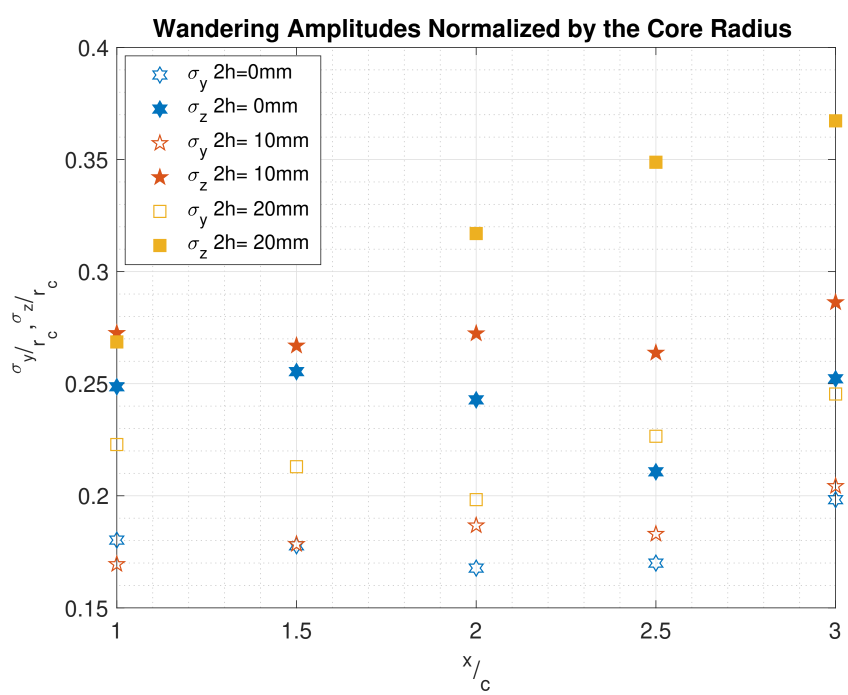

Fig. 3.36: Wandering Amplitudes (σ_y,σ_z) normalized by the core radius at each downstream position for the 0mm, 10mm and 20mm chevron plates

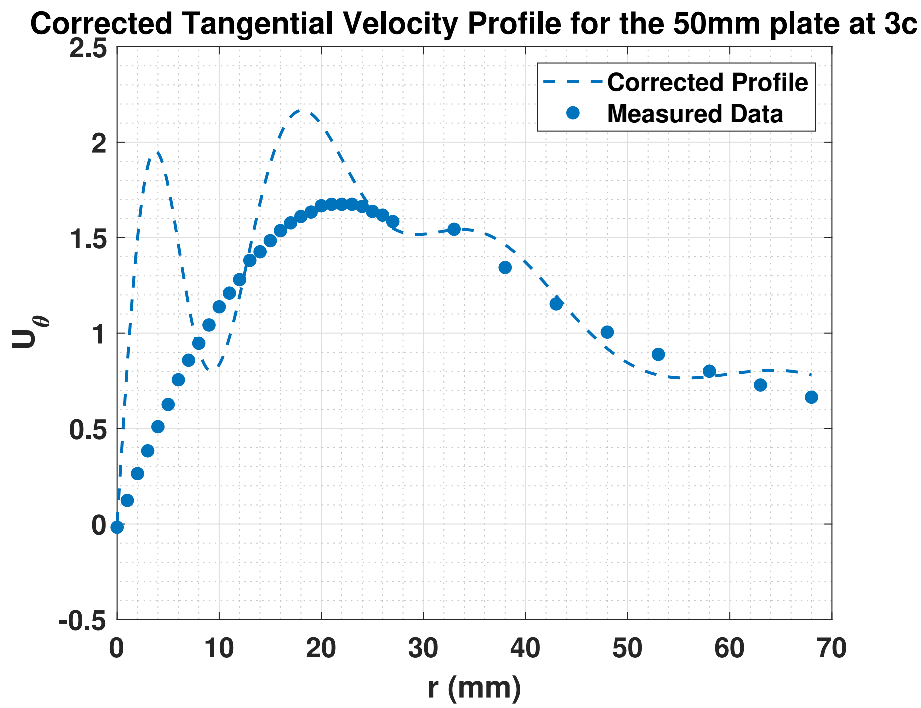

Fig. 3.37: Devenport *et al.*'s correction applied to the 50mm chevron plate at 3c

the frequency spectra at the center of the tip vortex.

3.6.1 Frequency Spectra at the Center of the Tip Vortex

The frequency spectra (F_{zz}) of w at the time averaged vortex center was used to indicate whether or not the flow in the core is turbulent. Fig 3.38 shows F_{zz} plotted against the frequency for all the test plates at 3c. The deeper chevron plates have a turbulent core, as opposed to the plates with shallow chevrons, and therefore, their tangential velocity profiles cannot be corrected by Devenport *et al.*'s correction. An alternative to correct these velocity profiles is by using the zero crossing technique proposed by Bailey *et al.* [56], which uses two four sensor hot wire probes to measure the velocity profiles in a frame of reference that is attached to the wandering axis. It was deemed that this correction method was beyond the scope of this thesis, due to the lack of sufficient anemometer channels to collect the required data. The 20mm chevron plate seemed to have a slope of the frequency spectrum that is closer to the $\frac{-5}{3}$ than the 0mm and 10mm plates, as shown in Fig 3.38. Therefore, the validity of Devenport *et al.*'s correction to the

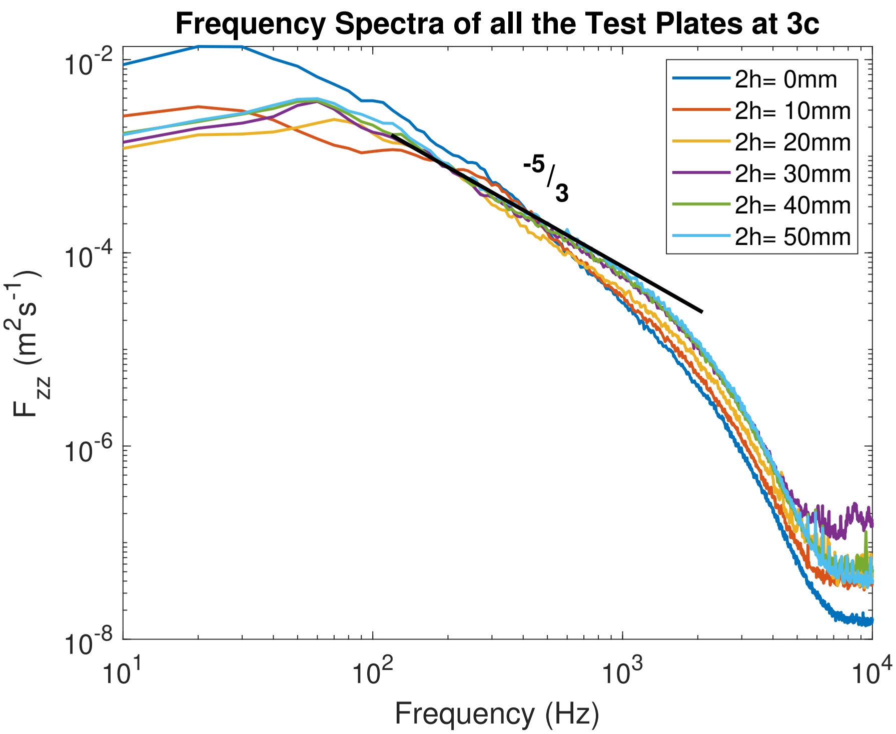

Fig. 3.38: F_{zz} for all the test plates at 3c.

tangential velocity profiles for this plate is uncertain.

We can speculate that the turbulence in the vortex core can be attributed to the fact that the vortex is still going through the roll up process, since our farthest measurements have been taken at a downstream distance of 3c. It has been shown by Katz *et al.* [60] that during the initial formation of a vortex, its core is turbulent due to the boundary layer on the wing and the axial velocity gradient in its core. There is no study that is unanimously agreed upon, that determines when the vortex roll-up is complete. Birch *et al.* [61] reported that the strength (or circulation) of a vortex was constant after a downstream distance of 1.5c and used the constant circulation as a criterion for determining when vortex roll up is complete. In contrast, Phillips [55] deemed the vortex roll up process to be complete when the spiral wake was distinct from the vortex core, which continues up to several chord lengths downstream of the wing. Green [34] identified the roll-up process to be complete when the vortex tangential velocity and circulation does not change with streamwise distance. Therefore, it is hard to determine whether or not the tip vortex roll up is complete at our farthest measurement plane of 3c.

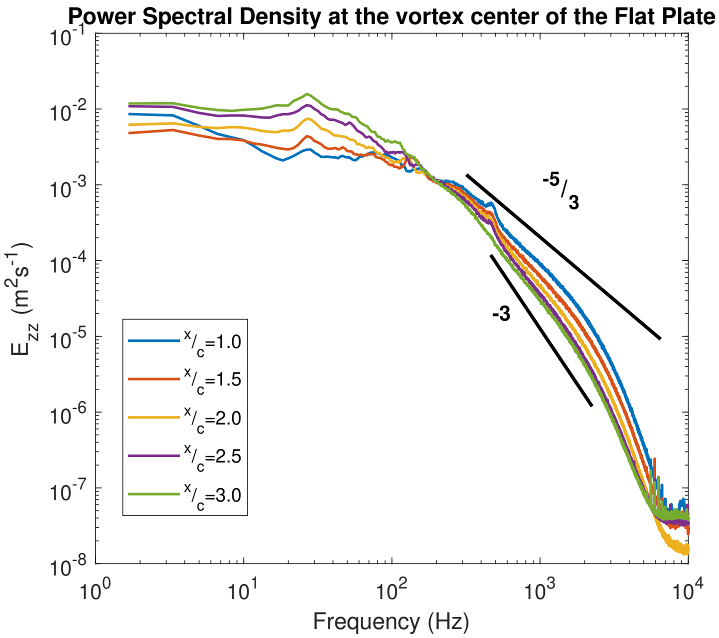

Fig. 3.39: F_{zz} of the flat plate for downstream distances $^x/_c$ = 1, 1.5, 2, 2.5 and 3. The slope of the spectra with respect to the frequency is -3 at every location, indicating a laminar core throughout

Since all the test plates are subjected to the same background turbulence in the test section, the only variable is the depth of the chevrons and one can speculate that deeper chevrons lead to the formation of vortices with a turbulent core that have a roll up process that lasts farther downstream than 3c. Bandyopadhyay *et al.* [49] observed that the mechanism of vortex decay is through 'stripping', where there is an exchange of momentum between fluid packets inside and outside the core. A turbulent core would therefore lead to an enhanced exchange of momentum, leading to lower peak tangential velocities and large core radii. This raises the question of whether or not the vortex core is turbulent at every downstream location and whether or not the bandwidth of frequencies over which the slope of F_{zz} with respect to the frequency is $\frac{-5}{3}$ is the same. The latter would give us information on whether the core becomes more turbulent with streamwise distance or not.

Fig 3.39 shows the power spectral density of w at the vortex center in the flat plate at downstream distances of $^x/_c$ = 1, 1.5, 2, 2.5 and 3. The power spectral density of w showed that the flat plate had a laminar core at every downstream position in the measurement plane, identified by the slope of the power spectral density, which was shown to be -3 by Devenport *et al*. This warranted the question of whether or not the tip vortex is turbulent in the near field of the test plates i.e., at ${}^{x}/_{c} < 1$. The power spectral density of w at the vortex center of the flat plate at ${}^{x}/_{c}$= 0.5 has a ${}^{-5}/_{3}$ slope, as shown in Fig 3.40. It can, therefore, be concluded that in the case

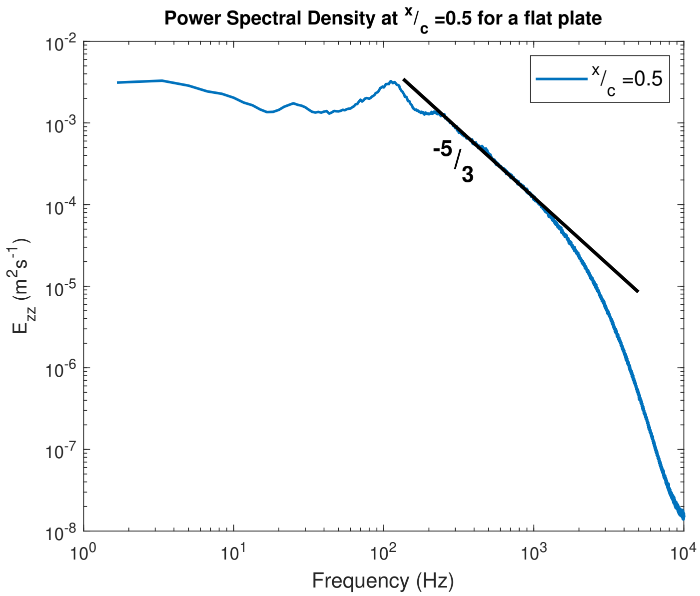

Fig. 3.40: F_{zz} of the flat plate for a downstream distances ${}^{x}/_{c}$= 0.5. The slope of the spectra with respect to the frequency appears to be ${}^{-5}/_{3}$, which implies that the vortex core is turbulent in the near field and laminarizes by${}^{x}/_{c}$ =1.

of the flat plate, the vortex core laminarizes by a downstream distance of 1c. A laminar core is explained by Mayer and Powell [62], who found that the vortex core is laminar in the absence of a large axial flow, irrespective of the Reynolds number. Furthermore, through Direct Numerical Simulation and Large Eddy Simulations, it has been shown that even if the axial flow is sufficient to destabilize the vortex, the turbulence generated diminishes the axial flow to a stable level, after which the vortex core returns to a laminar state [63].

The Power Spectral Density of w at the vortex center of the 10mm, 20mm , 30mm and 40mm chevron plates at downstream positions of ${}^{x}/_{c}$= 0.5, 1, 1.5, 2, 2.5 and 3 are shown in Fig 3.41, Fig 3.42, Fig 3.43, Fig 3.44 and Fig 3.45, respectively. In the 10mm chevron plate, the vortex core appears to be turbulent at downstream distances of 0.5c, 1c and 1.5c, which is indicated by the ${}^{-5}/_{3}$ slope of the power spectral density of w with respect to the frequency. At ${}^{x}/_{c} > 1.5$, the slope of the power spectral density is closer to -3, than $\frac{-5}{3}$ and therefore, the vortex core is laminar.

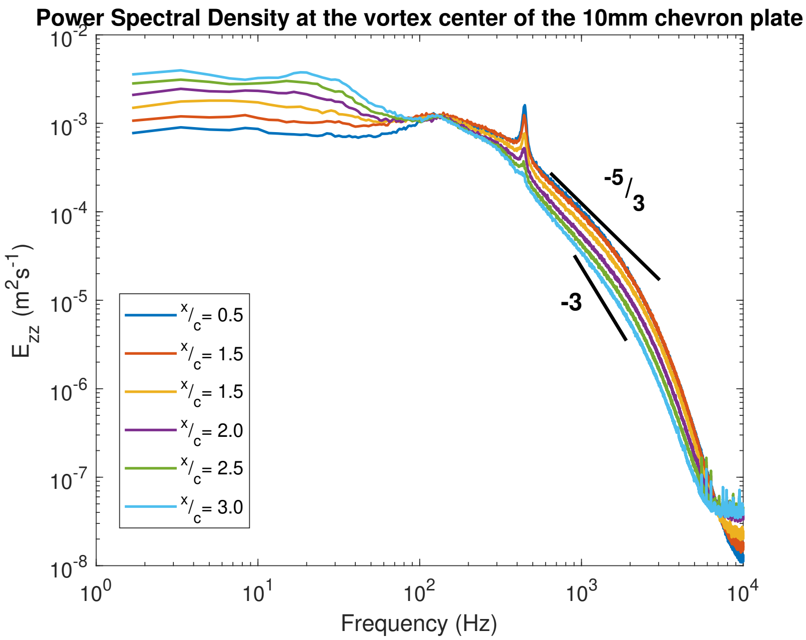

Fig. 3.41: F_{zz} of the 10mm chevron plate for a downstream distances $^x/_c$= 0.5, 1, 1.5, 2, 2.5 and 3. The slope of the spectra with respect to the frequency appears to be $^{-5}/_3$, for $^x/_c$= 0.5, 1 and 1.5, which implies that the vortex core is turbulent initially and laminarizes by$^x/_c$ =2.

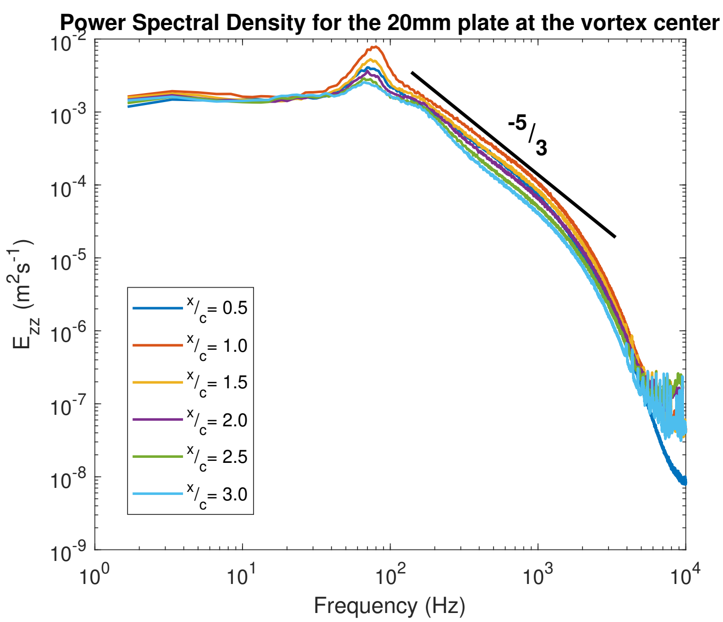

Fig. 3.42: F_{zz} of the 20mm chevron plate for a downstream distances $^x/_c$= 0.5, 1, 1.5, 2, 2.5 and 3. The slope of the spectra with respect to the frequency appears to be $^{-5}/_3$ at every downstream position, which implies that the vortex core is turbulent throughout.

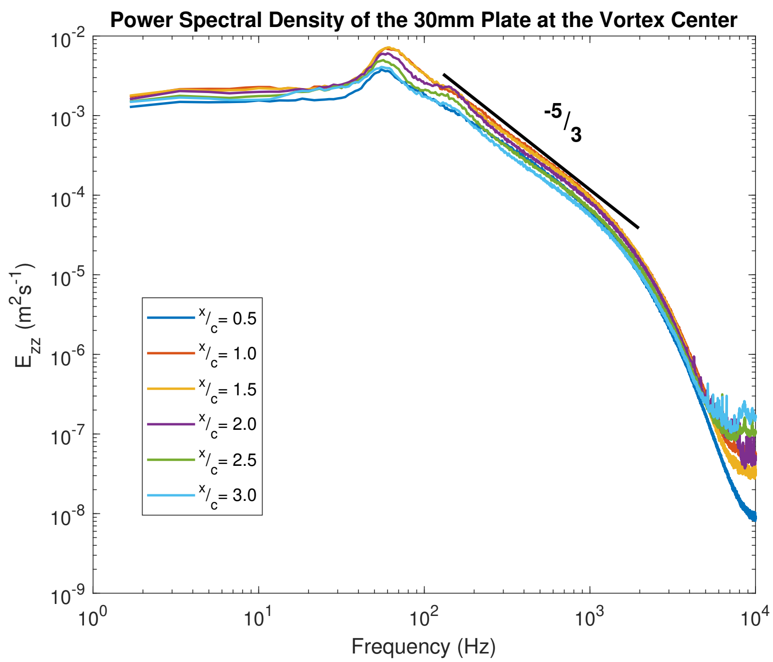

Fig. 3.43: F_{zz} of the 30mm chevron plate for a downstream distances $^{x}/_{c}$= 0.5, 1, 1.5, 2, 2.5 and 3. The slope of the spectra with respect to the frequency appears to be $^{-5}/_{3}$, at every downstream position, which implies that the vortex core is turbulent throughout.

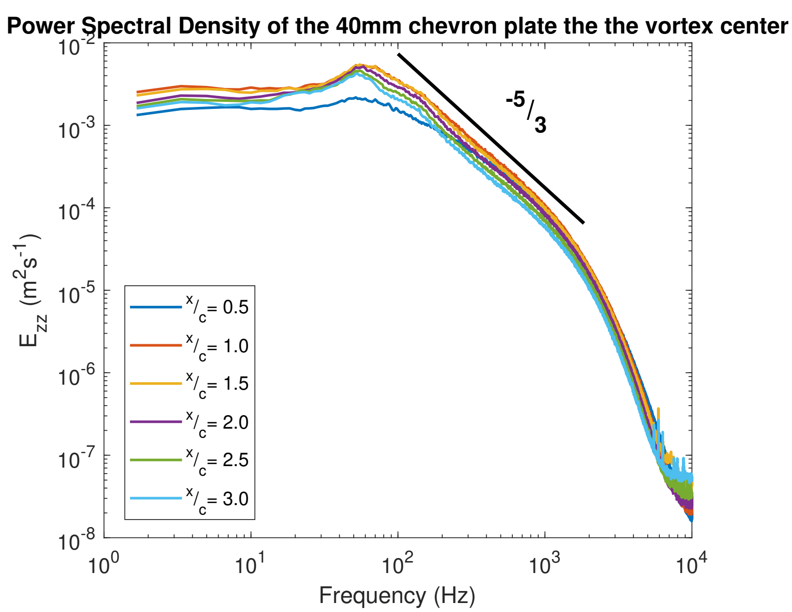

Fig. 3.44: F_{zz} of the 40mm chevron plate for a downstream distances $^{x}/_{c}$= 0.5, 1, 1.5, 2, 2.5 and 3. The slope of the spectra with respect to the frequency appears to be $^{-5}/_{3}$ at every downstream position, which implies that the vortex core is turbulent throughout.

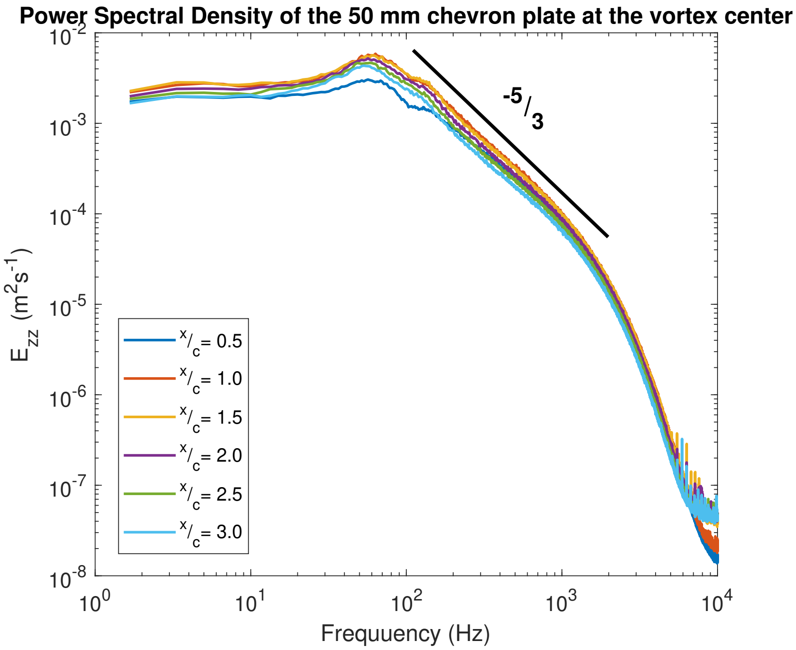

Fig. 3.45: F_{zz} of the 50mm chevron plate for downstream distances $^{x}/_{c}$= 0.5, 1, 1.5, 2, 2.5 and 3. The slope of the spectra with respect to the frequency appears to be $^{-5}/_{3}$ at every location, indicating turbulence in the core throughout

The 20mm, 30mm, 40mm and 50mm chevron plates exhibit a turbulent core at every downstream location. One can, therefore, speculate that the tip vortex for the 20mm, 30mm, 40mm and 50mm plates is still in its formation stage and therefore, exhibits a turbulent core. We can further speculate that if the tip vortex for these chevron plates laminarizes (at a farther downstream distance than 3c), its peak tangential velocity would be significantly lower and core radius would be larger as compared to the flat plate tip vortex, resulting in a weaker, more stable vortex with a laminar core. It is observed that the flat plate shows a turbulent vortex core in the near field, *i.e.,* at a downstream position of $^{x}/_{c}$= 0.5, and the vortex core becomes laminar by a downstream distance of 1c. Since the presence of shallow chevrons with $2h$= 10mm leads to a laminar core further downstream than the flat plate and the deeper chevrons show a turbulent core at every measurement plane, it is also safe to speculate that the turbulence in the core is due to the presence of chevrons- whether it is due to axial velocity profiles in the tip vortex formed over chevron plates or whether it is owing to the fact that the vortex roll up in chevron plates exhibits a turbulent core is unclear. We now consider the mean axial velocity profiles of the tip vortices to study if they are linked to the turbulence in the core. Singh and Uberoi [64] have shown that the presence of a large axial velocity gradient at the core leads to the production of turbulence, which gradually decays downstream. The following section, therefore, looks at the axial velocity profiles of the tip vortex for all the test plates.

3.6.2 Mean Axial Velocity Profiles

As mentioned in Section 3.1.1, in previous experiments, tip vortices have exhibited an axial velocity deficit [3] or an axial velocity surplus [35] in the core, and the profile of the axial velocity has been shown to depend on the angle of attack as well as the shape of the wing tip [39]. Fig 3.46 shows the difference between the mean axial velocity and the free stream velocity, normalized by the free stream velocity ($\frac{U-U_\infty}{U_\infty}$) with respect to the radial distance normalized by the core radius for a flat plate at downstream positions of 1c, 1.5c, 2c, 2.5c and 3c. It is observed that at the center of the vortex, there is an axial velocity deficit at each downstream position, however, the axial velocity deficit becomes a surplus at a radial distance of about 0.3 r_{core}. It can also be

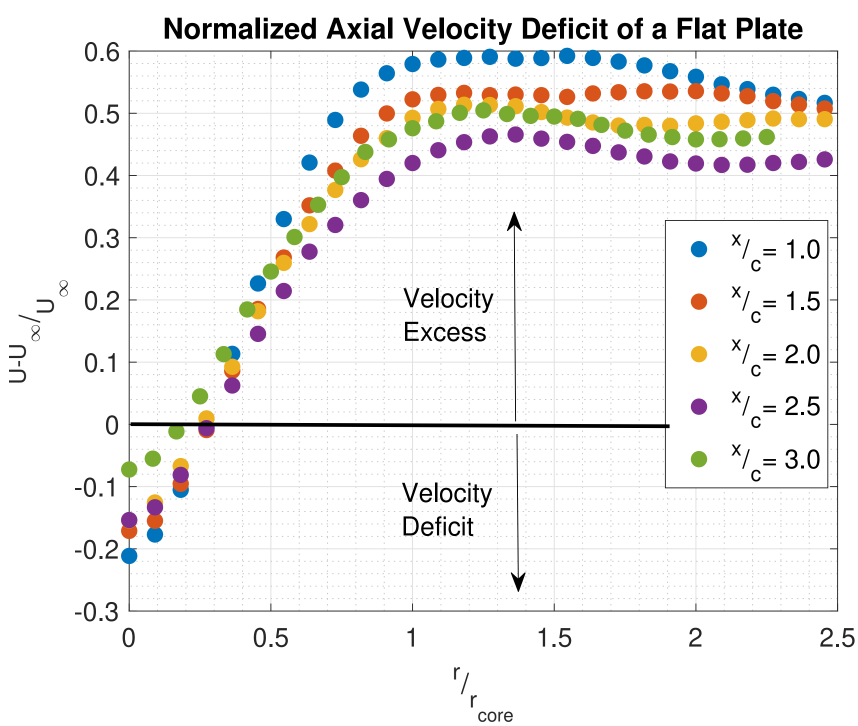

Fig. 3.46: $\frac{U-U_\infty}{U_\infty}$ plotted against $\frac{r}{r_c}$ for a Flat plate at downstream positions $^x/_c$= 1, 1.5, 2, 2.5 and 3

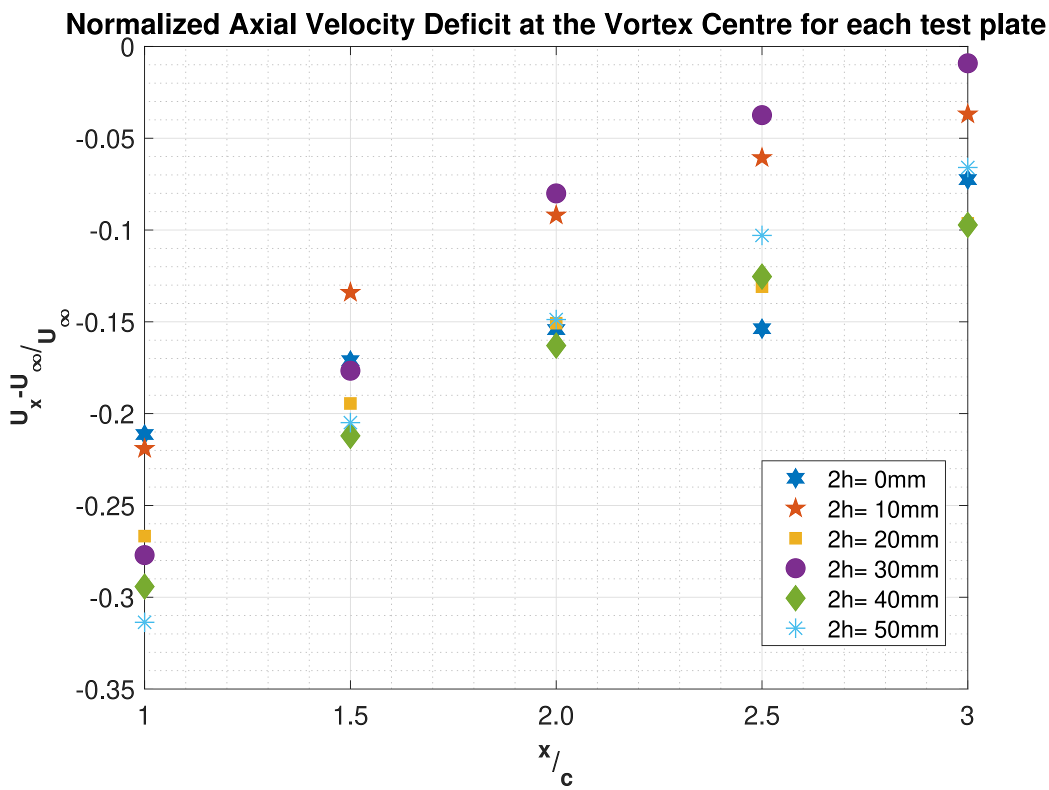

Fig. 3.47: $\frac{U-U_\infty}{U_\infty}$ at the vortex center for each test plate at downstream positions ${}^{x}/_{c}$= 1, 1.5, 2, 2.5 and 3

observed that the axial velocity deficit at the vortex center becomes smaller with an increase in the streamwise distance.

The normalized axial velocity deficit at the center of the tip vortex for downstream positions of $\frac{x}{c}$= 1, 1.5, 2, 2.5 and 3 for all the test plates are shown in Fig 3.47. At $\frac{x}{c}$ =1, the normalized axial velocity deficit increases as the depth of the chevrons increases. At the farthest downstream position ($\frac{x}{c}$ = 3), the 50mm chevron plate, which has the largest axial velocity deficit at 1c, has a nominally higher axial velocity deficit as compared to the flat plate. This can be attributed to the turbulent core of the 50mm plate- a turbulent core would lead to a higher diffusion of the axial velocity. As it was mentioned earlier, Ragab *et al.* [63] showed that the presence of a large axial velocity at the vortex center would lead to a higher turbulence, which in turn, would diffuse the axial velocity and eventually laminarize the core.The 10mm chevron plate, that has a slightly higher velocity deficit than the flat plate at $\frac{x}{c}$= 1, is initially turbulent and laminarizes at $\frac{x}{c}$= 2. At $\frac{x}{c}$= 3, its axial velocity deficit is lower that the flat plate. The 30mm chevron plate has a significantly larger axial velocity deficit at 1c and has a turbulent core at every downstream position. At 3c, it has the lowest axial velocity deficit amongst all the test plates. The 20mm and 40mm chevron plates have a difference in the axial velocity deficit at 1c (with the 40mm plate having a higher axial velocity deficit), however, at 3c, they have roughly the same axial velocity deficit, which is higher than the flat plate.

Fig 3.48 shows the mean axial velocity gradient ($\frac{UdU}{dx}$) at downstream positions of $\frac{x}{c}$= 1, 1.5, 2, 2.5 and 3, computed by performing a power law fit to the measured axial velocity at the vortex center at each downstream position. The axial velocity gradient at 1c does not have a clear pattern with chevron depth, however, it decreases with downstream distance for each test plate. Furthermore, the axial velocity gradient at each downstream position for the flat plate is significantly smaller than that for the chevron plates.

Clearly, the axial velocity in the core is linked to its turbulence- whether the axial velocity deficit is the cause of the turbulence, or its effect is unclear. It is clear, however, that the presence of the chevrons affect the overall form of the tip vortex by changing the peak tangential velocities, the axial velocities, the core radius and by affecting the turbulence in the vortex core. The

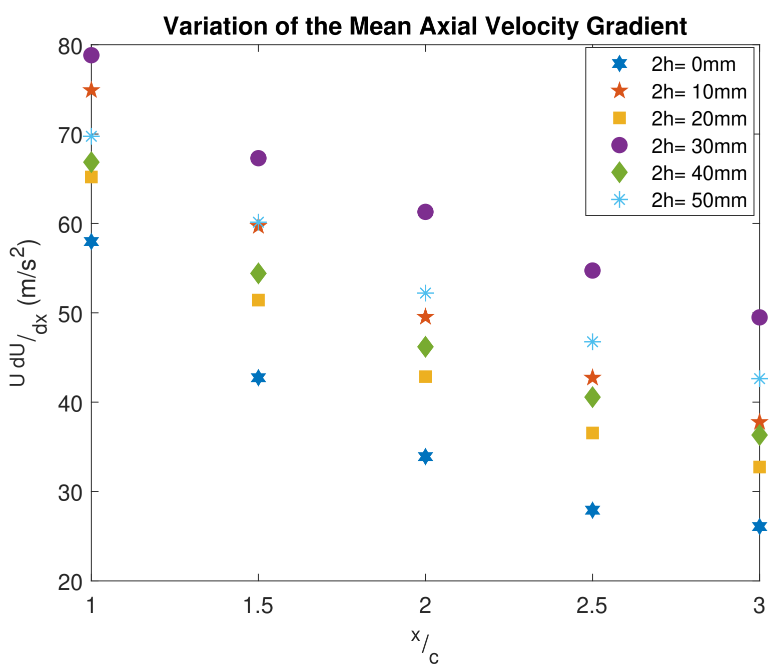

Fig. 3.48: Mean Axial Velocity gradient ($\frac{UdU}{dx}$) at downstream positions of $\frac{x}{c}$= 1, 1.5, 2, 2.5 and 3

following section looks at how chevron wing tips affect the wandering of the tip vortex.

3.7 Cross Power Spectra at the Vortex Center

Section 3.1.2 shed light on the phenomenon of vortex wandering and an analytical method to correct for it. Experimentally, vortex wandering poses a challenge for studies with fixed probes, as it leads to errors in the mean and turbulence measurements by smoothing out the mean and instantaneous velocities. One of the factors that vortex wandering is attributed to is the free stream turbulence in the wind or water tunnel. It has been shown that an increase in the free stream turbulence leads to an increase in the amplitude of vortex wandering [65]. Practically, vortex wandering- when subjected to atmospheric turbulence- can aid in the decay of aircraft trailing vortices by initiating instabilities that lead to the breakdown of tip vortices. Therefore, it is of interest to study how the presence of chevrons would affect the wandering of the tip vortex. As mentioned earlier, vortex wandering is a planar motion and affects both- V and W components of velocity. The cross power spectral density coefficient gives us information on the contribution of energy to both- V and W components over a range in frequencies. Fig 3.49 shows the cross power spectral density coefficient for the flat plate and Fig 3.50 shows the same for the 50 mm chevron plate.

The cross power spectral density coefficients for the two extreme cases- the flat plate and the 50 mm chevron plate- are significantly different. The flat plate shows contribution to energy over a wide range of frequencies: the most discernible peaks are at 10Hz, 30Hz, 100Hz and 300Hz, whereas, the 50mm chevron plate shows a single peak at 48Hz at each downstream location, which is associated with vortex wandering. In the case of the flat plate,the large bandwidth of frequencies over which the cross spectral power density coefficient shows a peak indicates that the contribution to wandering comes from several sources. The cross power spectral density coefficient of the 10mm, 20mm, 30mm and 40mm chevron plates is shown in Fig 3.51, 3.52, 3.53 and 3.54, respectively.

The 10mm plate exhibits a peak at 135Hz and 440Hz, which become smaller with an increase in streamwise distance. At $\frac{x}{c}$= 2.0, 2.5 and 3, there is peak at 10Hz which grows with streamwise distance. The depper chevron plates *i.e.,* the 20mm, 30mm and 40mm chevron plates have peaks at less than a frequency of 100 Hz. The 30mm plate show peaks between 145 and 220 Hz, in

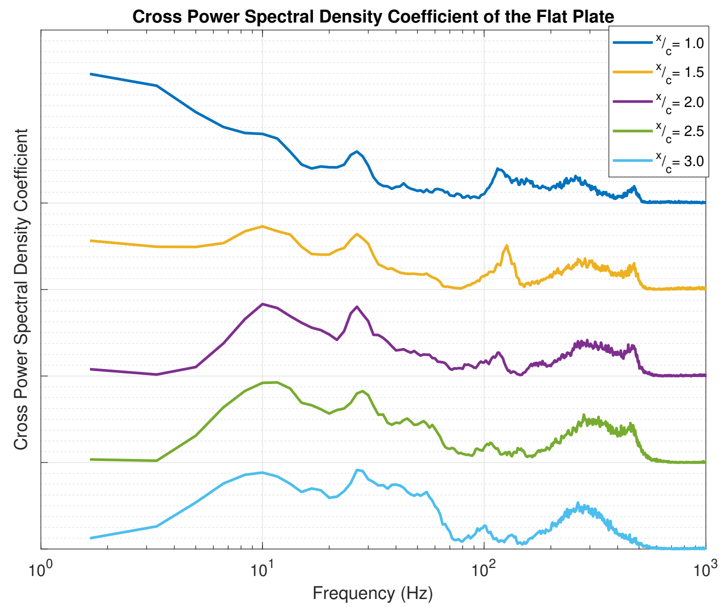

Fig. 3.49: Semi log plot of the Cross Power Spectral Density Coefficient for the Flat Plate at $\frac{x}{c}$= 1, 1.5, 2, 2.5 and 3; the spectra have been shifted down by 0.4 for clarity

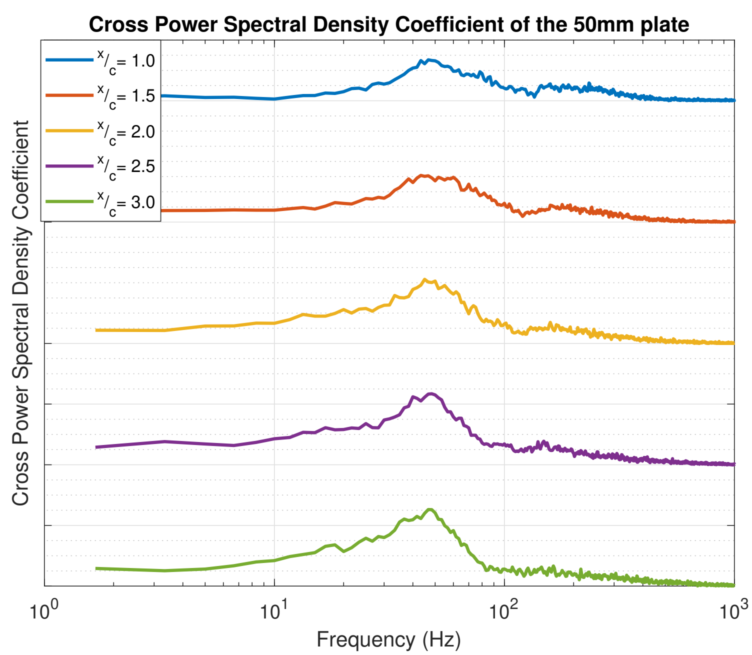

Fig. 3.50: Semi log plot of the Cross Power Spectral Density Coefficient for the 50mm chevron plate at $\frac{x}{c}$= 1, 1.5, 2, 2.5 and 3; the spectra have been shifted down by 0.4 for clarity

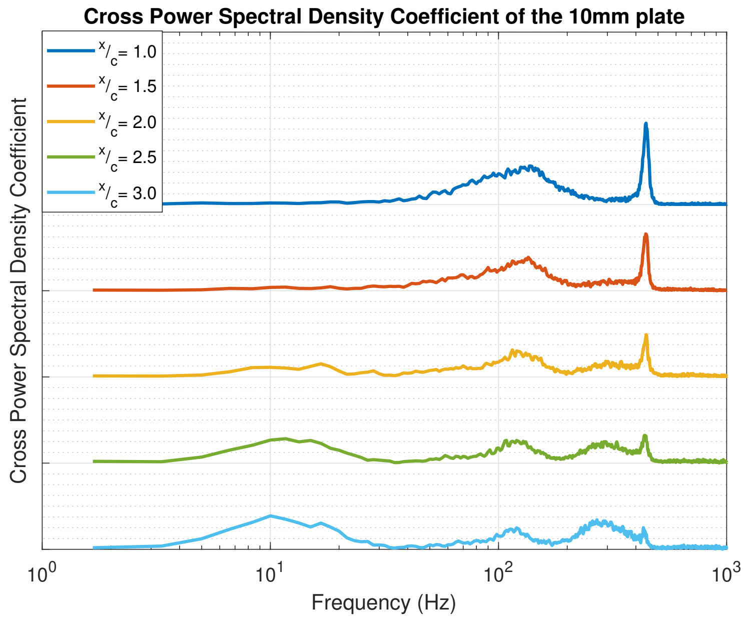

Fig. 3.51: Semi log plot of the Cross Power Spectral Density Coefficient for the 10mm chevron plate at $\frac{x}{c}$= 1, 1.5, 2, 2.5 and 3; the spectra have been shifted down by 0.4 for clarity

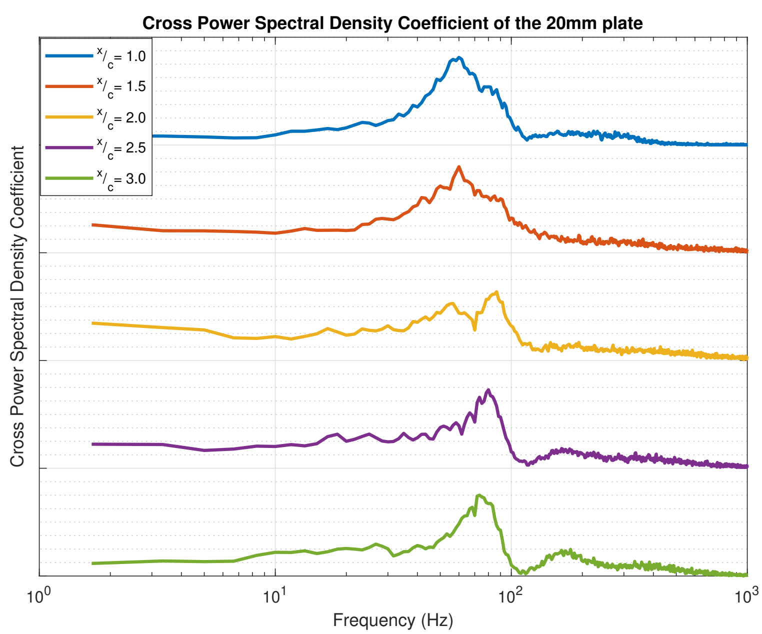

Fig. 3.52: Semi log plot of the Cross Power Spectral Density Coefficient for the 20mm chevron plate at $\frac{x}{c}$= 1, 1.5, 2, 2.5 and 3; the spectra have been shifted down by 0.4 for clarity

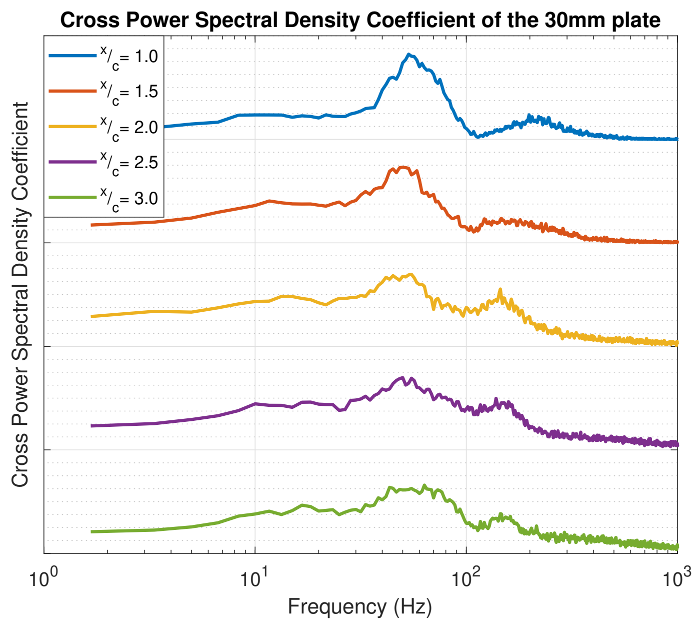

Fig. 3.53: Semi log plot of the Cross Power Spectral Density Coefficient for the 30mm chevron plate at $\frac{x}{c}$= 1, 1.5, 2, 2.5 and 3; the spectra have been shifted down by 0.4 for clarity

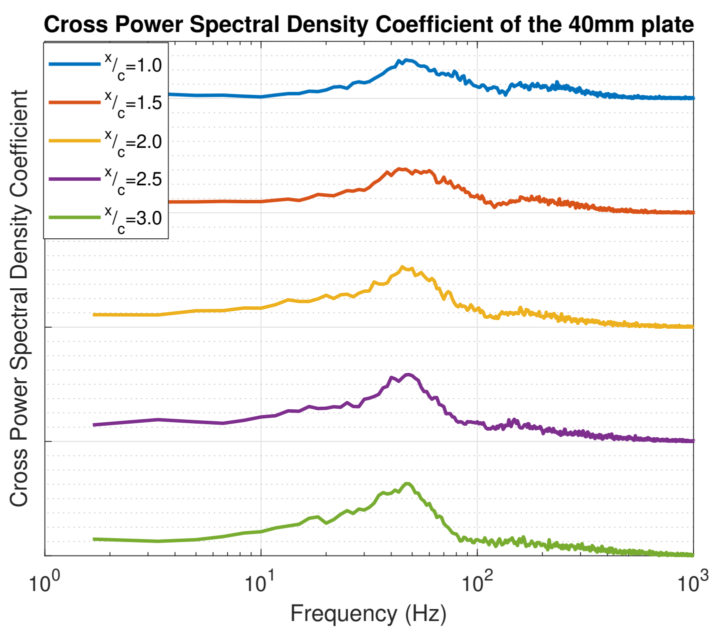

Fig. 3.54: Semi log plot of the Cross Power Spectral Density Coefficient for the 40mm chevron plate at $\frac{x}{c}$= 1, 1.5, 2, 2.5 and 3; the spectra have been shifted down by 0.4 for clarity

addition to the peak between 30Hz and 90Hz. According to Bailey *et al.* [56], wandering motion is associated with frequencies ‘significantly’ lower than the frequencies associated with turbulent acitivity in the core. No threshold, however, exists that marks what the ‘cut-off’ is between frequencies associated with wandering and those associated with turbulent activity in the core. The spectra for the chevron plates shows fewer dominant frequencies than the flat plate, leading one to speculate the following: a) the contribution of energy to the vortex center is from either vortex wandering or turbulence in the core or both, or b) the motion of the vortex center follows a set pattern in the case of chevron plates. While the exact effect of the chevrons on the turbulent activity in the tip vortex and the wandering of the vortex requires further investigation using PIV, it can be said with certainty that the cross spectra for the chevron plates is very different from that of the flat plate. Therefore, by extension, one can speculate that the wandering associated with chevron plates would also be significantly different than that of a flat plate. For instance, if we consider the wandering amplitudes normalized by the core radius, given by Devenport *et. al*’s correction to the flat plate, 10mm and 20mm chevron plates, we find that $\frac{\sigma_y}{r_c}$ and $\frac{\sigma_z}{r_c}$ increase with increase in chevron depths and downstream distances (see Fig 3.36). This is a significant finding because vortex wandering in atmospheric turbulence can aid in the faster dissipation of tip vortices.

Chapter 4

Future Work

This study was conducted on a very specific case- a flat plate with four chevrons at a Reynolds number of 67,000. Other studies can be conducted on plates with a larger number of chevrons that would more closely mimic bird wings. Within a chevron plate, the chevrons themselves could have variable depths, (or chevrons could be cut into the tips of an airfoil instead of a flat plate) again bringing us closer to a bird wing. This conceptual design is shown in Fig 4.1. It would

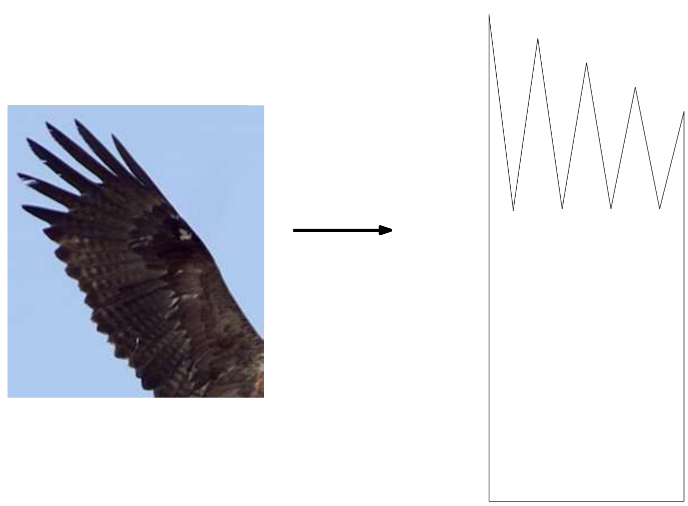

Fig. 4.1: Chevron plates with variable chevron depths

also be of interest to study whether or not the observed increase in aerodynamic efficiency for the 10mm and 20mm chevron plates and the weaker vortex observed for all the test plates is the same over a range of Reynolds numbers. Finally, instead of chevrons, other complex geometries such as fractals could be cut into the tips of wings and their impact on the tip vortex could be studied.

The development of the tip vortex could only be studied at a streamwise distance of 3c due to limitations in the length of the test section. Several studies on tip vortices suggest that the tip vortex is still developing within 3c. It would be of interest to investigate when the core of the chevron plate tip vortex would laminarize and how it would ultimately decay. The weaker vortices produced by the chevron plates also warrants further studies: the exact mechanism of vortex formation in the case of chevron plates remains unknown at this point. Furthermore, the significant difference in the cross power spectral density coefficient of the chevron plates as compared to the flat plates requires experiments using PIV, to attain a more comprehensive understanding of the flow field.

Chapter 5

Conclusions

This study focused on the impact that complex geometries, specifically, chevrons have on the tip vortex. Chevrons were used as they most closely resemble the ‘primaries’ on a bird wing. Through time resolved force and moment measurements using a six axis force/torque sensor, we found that the 10mm, 20mm and 30mm chevron plates had a higher peak aerodynamic efficiency (defined as the $\frac{L}{D}$ ratio) by 7.7%, 3.7% and 3.4%, respectively as compared to the flat plate. The 40mm and 50mm chevron plates had lower aerodynamic efficiencies (11.4% and 3.4%, respectively) than the flat plate. It was also observed the peak aerodynamic efficiency of each test plate was at a 5° angle of attack. The presence of the chevron geometries did not have an impact on the coefficients of roll and pitch moments, but made the coefficients of yaw moments more negative as compared to the flat plate. This was due to the shift in the position of the tip vortex- as the chevron depth increased, the vortex center was lifted up and moved towards the root of the wing. We can speculate that this lead to a change in the pressure distribution, which, in turn, resulted in a change in the Center of Pressure, thereby, changing the moment arm.

The mean velocity profiles was measured using constant temperature anemometry and a four sensor hot wire probe for each test plate mounted at a 5° angle of attack (as it corresponded to the angle of the peak aerodynamic efficiency). It was found that the chevron plates had a significantly smaller peak tangential velocities and larger core radii than the flat plate (with the exception of the 10mm plate, that showed a smaller core radius). All the test plates exhibited a ‘double core’ structure at a downstream distance of 0.5c, which disappeared by 1c. An axial velocity deficit was observed for the test plates at the vortex center, which became a surplus by $0.3r_{core}$. The cross power spectral density coefficient of v and w showed the presence of spikes at different frequency bands for different test plates, indicating vortex wandering. Vortex wandering is a low frequency meandering motion of the tip vortex, attributed to various factors like turbulence in the test section, instability in the vortex core, *etc.* To correct for vortex wandering, an analytical correction proposed by Devenport *et al.* was applied to the tangential velocity profiles of flat plate, 10mm and 20mm chevron plate. The correction showed larger peak tangential velocities and smaller core radii as compared to the uncorrected profiles. However, after the corrections were implemented, the peak tangential velocities of the chevron plates were smaller than the peak tangential velocity of the flat plate at each downstream position. The core radii of the 20mm chevron plate was larger than the flat plate and the 10mm plate still had smaller core radii than the flat plate. Therefore, as compared to the flat plate, the chevron plates lead to the formation of a weaker vortex.

This correction could not be applied to the 30mm, 40mm and 50mm chevron plates, as they exhibited a turbulent core, which was ascertained by the $\frac{-5}{3}$ slope of the power spectral density of the w velocity. For the flat plate, the core was laminar at 0.5c and became laminar by 1c, whilst for the 10mm chevron plate, it was found that the core was turbulent at 0.5c, 1c and 1.5c. At 2c, the core became laminar. The rest of the test plates showed a turbulent core at every downstream position, indicating that the tip vortex hadn't become stable up to the farthest downstream position where measurements were taken. The reason for the turbulent core was unclear- whether the presence of an axial velocity deficit at the core made the core turbulent or whether the turbulence in the core lead to the axial velocity profiles that were observed is a question that warrants further measurements using PIV.

Finally, the cross power spectral density coefficient at the vortex center was significantly different for the chevron plates as compared to the flat plate; the chevron plates exhibited a narrower frequency range with spikes as compared to the flat plate. The source of energy for each spike in the cross power spectral density coefficient was not clear- the energy contribution could be from the wandering motion of the vortices or the turbulence in the core or both. The narrow frequency band of the chevron plates could also be indicative of a set pattern followed by the tip vortex in their wandering motion.

Through this study, it has been established that the presence of chevrons has an impact on the tip vortex. The use of 10mm, 20mm and 30mm deep chevrons leads to a 7.7%, 3.7% and 3.4% higher aerodynamic efficiency as well as a weaker tip vortex as compared to the flat plate. One can also speculate that the deeper chevrons could be implemented on the tips of winglets to compensate for their lower aerodynamic performance on a flat plate.

References

[1] T. Sarpkaya, “Trailing vortices in homogeneous and density-startified media.” *Journal of Fluid Mechanics*, vol. 136, pp. 85–109, 1983.

[2] M. Giuni and R. B. Green, “Vortex formation on squared and rounded tip,” *Aerospace Science and Technology*, vol. 29, pp. 191–199, 08 2013.

[3] W. J. Devenport, M. C. Rife, S. I. Liapis, and G. J. Follin, “The structure and development of a wing-tip vortex,” *Journal of Fluid Mechanics*, vol. 312, pp. 67–106, 1996.

[4] J. D. Anderson, *Fundamentals of Aerodynamics*. The McGraw Hill Companies, 2007.

[5] ”IATA”, “”iata industry statistics fact sheet”,” 2018. [Online]. Available: ”https://www.iata.org/pressroom/facts_figures/fact_sheets/Documents/fact-sheet-industry-facts.pdf”

[6] J. Anderson, *Aircraft Performance and Design*. The McGraw Hill Companies, 1999.

[7] L. Prandtl and O. Tietjens, *Applied Hydro- and Aeromechanics*. United Engineering Trustees, Inc., 1934.

[8] J. Anderson, *Introduction to Flight*. The McGraw Hill Companies.

[9] R. Cummings and J. Bertin, *Aerodynamics for Engineers*. Pearson, 2014.

[10] S. Crow, “Stability theory for a pair of trailing vortices,” *AIAA Journal*, vol. 8, no. 12, pp. 2172–2179, 1970.

[11] F. Lanchester, *Aerodynamics*, ser. Lanchester: Aerial flight. Archibald Constable, 1907.

[12] J. R. Chambers, "Winglets- concept to reality: Contributions of the langley research centre to us civil aircraft of the 1990s," *NASA Langley Research Centre*, p. 35, 2003.

[13] R. T. Witcomb., "A design approach and selected wind-tunnel results at high subsonic speeds for wing-tip mounted winglets," *NASA Technical Reports*, 1976.

[14] D. M. Guerrero, J.E. and A. B., "Biomimetic spiroid winglets for lift and drag control," *Comptes Rendus Mecanique*, vol. 1, no. 340, pp. 67–80, 2012.

[15] C. J. Bargsten and M. T. Gibson, "Nasa innovation in aeronautics: Select technologies that have shaped modern aviation," *National Aeronautics and Space Administration*, pp. 11–22, 2011.

[16] D. McLean, "Wingtip devices: What they do and how they do it," *Performance and Flight Operations Engineering Conference*, 2005.

[17] C. Van Dam, "Induced-drag characteristics of crescent-moon shaped wings," *Journal of Aircraft*, vol. 24, no. 2, 1987.

[18] B. Lazos and K. Visser, "Aerodynamic comparison of hyper-elliptic cambered span (hecs) wings with conventional configurations," in *24th AIAA Applied Aerodynamics Conference*, 2006, p. 3469.

[19] K. A. Sheppard and D. E. Rival, "On the high-lift characteristics of a bio-inspired, slotted delta wing," *Bioinspiration & Biomimetics*, vol. 13, no. 3, p. 036008, apr 2018. [Online]. Available: https://doi.org/10.1088%2F1748-3190%2Faaafbd

[20] N. Tombazis and P. Bearman, "A study of three-dimensional aspects of vortex shedding from a bluff body with a mild geometric disturbance," *Journal of Fluid Mechanics*, vol. 330, p. 85–112, 1997.

[21] J. Nedić, O. Supponen, B. Ganapathisubramani, and J. C. Vassilicos, "Geometrical influence on vortex shedding in turbulent axisymmetric wakes," *Physice of Fluids*, 2015.

[22] P. C. Withers, "An aerodynamic analysis of bird wings as fixed airfoils," *Journal of Experimental Biology*, vol. 90, pp. 143–162, March 1981.

[23] V. Tucker, “Drag reduction by wing tip slots in a gliding harris hawk, parabuteo unicinctus,” *Journal of Experimental Biology*, no. 198, pp. 775–781, 1995.

[24] T. Chong and A. Vathylakis, “Self-noise produced by an airfoil with nonflat plate trailing-edge serrations,” *AIAA Journal*, vol. 51, no. 11, 2013.

[25] J. Nedić and J. Vassilicos, “Vortex shedding and aerodynamic performance of airfoil with multiscale trailing-edge modifications,” *AIAA Journal*, 2015.

[26] S. Prigent, O. Buxton, and P. J. K. Bruce, “Coherent structures shed by multiscale cut-in trailing edge serrations on lifting wings,” *Physics of Fluids*, vol. 29, p. 075107, 07 2017.

[27] N. Thomareis and G. Papadakis, “Effect of trailing edge shape on the separated flow characteristics around an airfoil at low reynolds number: A numerical study,” *Physics of Fluids*, vol. 29, no. 1, p. 014101, 2017. [Online]. Available: https://doi.org/10.1063/1.4973811

[28] S. Ito, “Aerodynamic influence of leading-edge serrations on an airfoil in allow reynold’s number,” *Journal of Biomechanical Science and Engineering*, vol. 4, no. 1, pp. 117–123, 2009.

[29] N. B. Wygnanski, I., “General description and calibration of the mcgill 3ft x 2ft low speed wind tunnel,” 1961.

[30] J. Ferguson-Lees and D. A. Christie, *Raptors of the World*. Houghton Mifflin Harcourt, 2001.

[31] A. Pope, *Low-Speed Wind Tunnel Testing*. The McGraw Hill Companies, 1966.

[32] F. Schmitz, “The aerodynamics of small reynold’s numbers,” *NASA Technical Memorandum, year=1980, pages=2*.

[33] A. Pelletier and J. Mueller, “Low reynolds number aerodynamics of low-aspect-ratio, thin/flat/cambered-plate wings,” *Journal of Aircraft*, vol. 37, no. 5, pp. 826–828, 2000.

[34] I. Green, *Fluid Vortices*. Springer Science+Business Media Dordrecht, 1995.

[35] Z. G. Chow, J.S. and P. Bradshaw, “Initial roll-up of a wingtip vortex in: Proceedings of the aircraft wake vortices conference,” *Federal Aviation Administration*, vol. 2, 1992.

[36] S. Green and A. Acosta, "Unsteady flow in trailing vortices," *Journal of Fluid Mechanics*, no. 227, pp. 107–134, 1991.

[37] D. R. Stinebring, K. J. Farrell, and M. L. Billet, "The structure of a three dimensional vortex at high reynolds number," *Journal of Fluids Engineering*, vol. 113, pp. 496–503, 1983.

[38] G. K. Batchelor, "Axial flow in trailing line vortices," *Journal of Fluid Mechanics*, vol. 20, no. 4, p. 645–658, 1964.

[39] E. A. Anderson and T. A. Lawton, "Correlation between vortex strength and axial velocity in a trailing vortex," *Journal of Aircraft*, vol. 40, no. 4, pp. 699–704, 2003.

[40] A. Shekarriz, T. C. Fu, J. Katz, H. L. Liu, and T. T. Huang, "Study of junction and tip-vortices using particle displacement velocimetry," *AIAA Journal*, vol. 31, pp. 112–118, 1983.

[41] S. Bailey, B. H.K. Lee, and S. Tavoularis, "Effects of free-stream turbulence on wingtip vortex formation and near field," *Journal of Aircraft*, vol. 43, pp. 1282–1291, 09 2006.

[42] J. Iversen, "Correlation of turbulent trailing vortex decay data," *Journal of Aircraft*, no. 13, pp. 338–342, 1976.

[43] T. Sarpkaya and J. J. Daly, "Effect of ambient turbulence on trailing vortices," *Journal of Aircraft*, vol. 24, pp. 399–404, 1987.

[44] H. Chevalier, "Flght test studies of the formation and dissipation of trailing vortices," *Journal of Aircraft*, vol. 10, pp. 14–18, 1973.

[45] J. D. Jacob, D. Liepmann, and O. Savas, "Natural and forced growth characteristics of the vortex wake from a rectangular airfoil," *AGARD CP 584*, 1996.

[46] C. S. Lee, D. Tavella, N. J. Wood, and L. Roberts, "Flow structure and scaling laws in lateral wing-tip blowing," *AIAA Journal*, vol. 27, pp. 1002–1007, 1988.

[47] A. L. Heyes and D. A. R. Smith, "Spatial perturbation of a wing-tip vortex using pulsed span-wise jets," *Experiments in Fluids*, vol. 37, pp. 120–127, 2004.

[48] M. Ahmadi-Baloutaki, R. Carriveau, and D. S.-K. Ting, "An experimental study on the interaction between free-stream turbulence and a wing-tip vortex in the near-field," *Aerospace Science and Technology*, vol. 43, pp. 395–405, 2015.

[49] P. R. Bandyopadhyay, D. J. Stead, and R. L. Ash, "The organized structure of a turbulent trailing vortex." *21st Fluid Dynamics, Plasma Dynamics, and Lasers Conference, Seattle, WA.*, pp. 395–405, 1990.

[50] G. R. Baker, S. J. Barker, K. K. Bofah, and P. Saffman, "Laser anemometer measurement of trailing vortices in water." *Journal of Fluid Mechanics*, vol. 65, pp. 325–336, 1990.

[51] A. Heyes, R. F. Jones, and D. A. R. Smith, "Wandering of wing-tip vortices," 07 2019.

[52] A. Scientific, "Auspex 4-sensor vorticity probe," http://www.auspexscientific.com/auquvopr.html.

[53] A. Labs, "Hot wire and film anemometry system- user's manual."

[54] E. and M. A, "A wind tunnel investigation of a wing-tip trailing vortex," 08 2019.

[55] W. R. C. Phillips, "The turbulent trailing vortex during roll-up," *Journal of Fluid Mechanics*, vol. 105, p. 451–467, 1981.

[56] S. Bailey and S. Tavoularis, "Measurements of the velocity field of a wing-tip vortex, wandering in grid turbulence," *Journal of Fluid Mechanics*, vol. 601, pp. 281 – 315, 04 2008.

[57] S. B. Pope, *Turbulent Flows*. Cambridge University Press, 2000.

[58] L. Tennekes and J. Lumley, *A First Course in Turbulence*. MIT Press, 2011.

[59] G. Iungo, P. Skinner, and G. Buresti, "Correction of wandering smoothing effects on static measurements of a wing-tip vortex," *Experiments in Fluids*, vol. 46, pp. 435–452, 01 2009.

[60] J. Katz and J. Bueno Galdo, "Effect of roughness on rollup of tip vortices on a rectangular hydrofoil," *Journal of Aircraft*, vol. 26, pp. 247–253, 03 1989.

[61] T. Lee and D. Birch, "Rollup and near-field behavior of a tip vortex," *Journal of Aircraft*, vol. 40, 05 2003.

[62] E. W. Mayer and K. Powell, "Similarity solutions for viscous vortex cores," *Journal of Fluid Mechanics*, vol. 238, pp. 487 – 507, 05 1992.

[63] S. Ragab, "Direct numerical simulation of instability waves in a trailing vortex," 01 1995.

[64] P. Indar Singh and M. S. Uberoi, "Experiments on vortex stability," *Physics of Fluids*, vol. 19, pp. 1858–1863, 12 1976.

[65] G. Baker, S. Barker, K. K. Bofah, and P. G. Saffman, "Laser anemometer measurements of trailing vortices in water," *Journal of Fluid Mechanics*, vol. 65, pp. 325 – 336, 08 1974.